GRANT/AMES

114P

IN-23710

NUMERICAL STUDIES OF POROUS AIRFOILS IN TRANSONIC FLOW

NCC 2-355

FINAL REPORT

June 1, 1985 - August 31, 1986

Dr. Chuen-Yen Chow
Principal Investigator

University of Colorado
Department of Aerospace Engineering Sciences
Campus 429
Boulder, CO 80309

COMPUTATION OF TRANSONIC FLOW OVER POROUS AIRFOILS

by

Chung-Lung Chen

B. S., National Cheng Kung University, 1979

M. S., University of Colorado, 1983

A thesis submitted to the

Faculty of the Graduate School of the

University of Colorado in partial fulfillment

of the requirements for the degree of

Doctor of Philosophy

Department of Aerospace Engineering Sciences

1986

This thesis for the Doctor of Philosophy degree by

Chung-Lung Chen

has been approved for the

Department of

Aerospace Engineering Sciences

by

_____

Chuen-Yen Chow

_____

Patrick D. Weidman

Date_____

Chen, Chung-Lung (Ph.D., Aerospace Engineering Sciences)

Computation of Transonic Flow over Porous Airfoils

Thesis directed by Professor Chuen-Yen Chow

A numerical tool is constructed to examine the effects of a porous surface on transonic airfoil performance and to help understand the flow structure of passive shockwave/ boundary layer interactions. The porous region is located near the shock with a cavity underneath it. This study is composed of two parts. Solved in the first part, with an inviscid-flow approach, is the transonic full-potential equation associated with transpiration boundary conditions which are obtained from porosity modeling. The numerical results of this part indicate that a porous airfoil has a wave drag lower than that of a solid airfoil. The observed lambda-shock structure in the wind-tunnel testing can be predicted. Furthermore, the lift could be increased with an appropriate porosity distribution.

In the second part of this work, the modified version of either an interactive boundary layer (IBL) algorithm or a thin-layer Navier-Stokes (TLNS) algorithm is used to study the outer flow, while a stream-function formulation is used to model the inner flow in the shallow cavity. The coupling procedure at the porous surface is based on Darcy's law and the assumption of a constant total pressure in the cavity. In addition, a modified Baldwin-Lomax turbulence model is used to describe the transpired turbulent boundary layer in the TLNS approach, while the Cebeci turbulence model is used in the IBL approach. According to the present analysis, a porous surface can reduce the wave drag appreciably, but can also increase the viscous losses. As has been observed experimentally, the numerical results indicate that the total drag is

reduced at higher Mach numbers and increased at lower Mach numbers when the angles of attack are small. Furthermore, the streamline pattern of passive shock/boundary layer interaction are revealed in this study.

ACKNOWLEDGMENTS

The author is indebted to many people for their help and consideration. A special thanks goes to Professor C. Y. Chow for sharing his knowledge, for his great support, and for his continuous guidances throughout the work. Many thanks go to Drs. Terry Holst and William Van Dalsem of NASA-Ames Research Center for their valuable discussions and for providing the TAIR and TRIVIA codes. The author also appreciates Dr. T. H. Pulliam for providing the ARC2D code.

I also thank Dean Seebass, Professor Weidman, Professor McCormick for reviewing my thesis and for their bright suggestions.

Finally, The author is particularly grateful to Drs. B. Baldwin and C. M. Hung of NASA-Ames Research Center for their valuable suggestions and discussions during the course of this work.

Funds for the support of this study have been allocated by the NASA-Ames Research Center, Moffett Field, California, under Grant NCC-2-355. All the work was done at NASA-Ames Research Center.

CONTENTS

FIGURES

Figure

CHAPTER I

INTRODUCTION

Background

A method often adopted to reduce the drag associated with shock-waves and to improve performance envelopes for transonic aircraft is the use of supercritical shock free airfoil sections for the wings. Three computational procedures have commonly been applied to design a supercritical airfoil:

1) Procedures involving indirect methods. The hodograph and fictitious gas methods are in this category.

2) Procedures involving inverse methods. Methods for solving the classical inverse problem of aerodynamics are in this category.

3) Direct methods. This category is characterized by use of a direct computational fluid dynamics (CFD) analysis program, coupled with a numerical optimization algorithm.

For an extensive list of references and survey articles the reader is referred to Holst et al.[1]

However, supercritical airfoils are only effective at quite restricted design conditions, since drag increases rapidly at off-design conditions.[2] In order to extend the optimum conditions, a simple and economical concept for drag reduction was suggested by Dennis Bushnell and Richard Whitcomb of NASA Langley Research Center in 1979, according to which a passive shock-wave/boundary layer control is achieved by using a porous surface with a

plenum chamber underneath the shock location. This device can be categorized into combined suction and blowing devices, which have been used for boundary layer control (BLC) since 1940.[3]

Theoretically, the drag reduction of a transonic airfoil can be achieved if boundary layer separation and shock wave strength can be controlled by applying appropriate blowing or suction at the airfoil surface. Appropriate blowing in the supersonic region ahead of a strong shock may cause it to degenerate into a series of weaker waves or to generate another oblique shock upstream of the injection region, thus resulting in a smaller pressure gradient and a smaller entropy change. The additional kinetic energy supplied by blowing also increases the mixing rate in the boundary layer and prevents flow separation. However, strong blowing not only thickens the boundary layer but also probably provokes an early separation as a side effect. On the other hand, the application of suction in the strong adverse-pressure gradient region would possibly delay separation but might produce a stronger shock and cause a higher wave drag as a side effect. In addition, if the suction area is of limited extent, it is necessary to examine whether the resulting boundary layer is capable of overcoming the adverse pressure gradient downstream of the suction region. Furthermore, according to an approximate nonasymptotic approach for weak shock/turbulent boundary layer interaction (including the mass transfer effects for attached flow), a small amount of suction could hasten the onset of separation slightly behind the shock foot.[4] Either blowing or suction requires power, thus an extra pump drag should be added to the total drag of the airfoil when an active control device is used. A passive control device (as sketched in Fig. 1.1), which provides blowing and suction without externally supplied power, hopefully, reaps the benefits of both blowing and

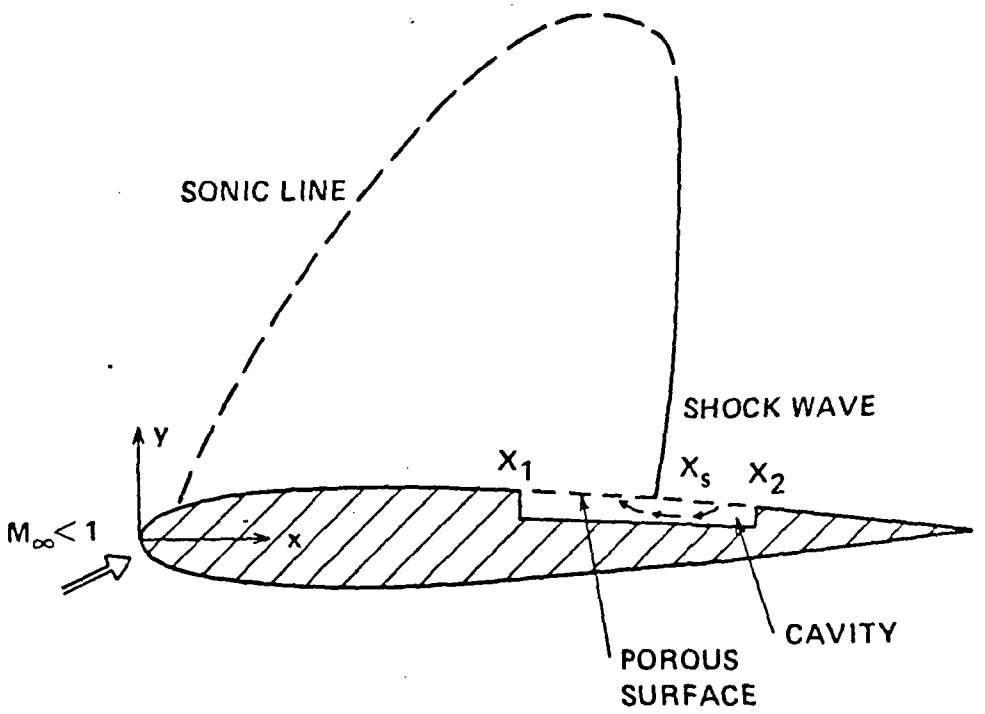

Fig. 1.1 Porous airfoil in transonic flow.

suction without their negative effects and without excessive use of space. This expectation has been initially proven by the experimental results obtained by Bahi et al.[5] and Nagamatsu et al.[6-7] which indicated that at high-subsonic Mach numbers a properly arranged porosity can reduce total drag appreciably. But at lower Mach numbers, the drag was increased. Also a lambda-shock structure was observed above the porous airfoil in the experiments. In these experiments, the airfoil model was mounted so that the lower half of the airfoil was embedded in the bottom wall of the test section and only the upper surface was exposed to the transonic flow. The porous surface extended over about 27% of the chord length.

Savu et al.[8] presented Schlieren photographs for two airfoil models. The porous surface extended from near the leading edge to the trailing edge. They observed a reduction in shock wave strength as well.

The passive shock wave/boundary layer interaction was investigated by Krogmann et al.[9] and Thiede et al.[10] They introduced a double-slot model and also studied the active suction effects. Their experimental results for a VFW VA-2 supercritical airfoil indicated that passive effects were effective primarily at relatively high Mach numbers and high angles of attack. In addition, they reported both a reduction in the drag and an increase in the lift on a porous airfoil model. Furthermore, their results indicate that local suction in the shock region delayed the shock-induced separation and considerably improved the overall aerodynamic performance. For a double slotted configuration at high angles of attack, no severe buffeting was noticed even though the flow was separated near the trailing edge. In general, they did not observe that the shock strength was significiently affected. These authors expressed uncertainty in the accuracy of their boundary layer probe measurements.

Recently, Raghunathan and Mabey[11] studied a 6 percent thick circular arc half airfoil set on a wind tunnel roof. They investigated the effect of hole orientation on the passive shockwave/boundary layer control and found that forward facing holes can reduce the drag appreciably. They also obtained a reduction in drag at higher Mach numbers and an increase in drag at lower Mach numbers for a porous airfoil, which agrees with the results of Bahi et al.[5] and Nagamatsu et al.[6,7]

Before numerical studies of porous airfoils are surveyed, it is helpful to briefly review previous studies of transonic flow over solid airfoils. Although some physical assumptions may not be strictly valid and numerical instability may result from the treatment of boundary conditions, in principal, the numerical approach used for solid airfoils can be extended to the study of porous airfoils.

The problem of transonic flow over a solid airfoil has been extensively studied with three different general approaches. The first approach is solving the nonlinear inviscid governing equations which can be either the transonic small-disturbance potential equation, the full-potential equation or the Euler equations. Only a small amount of computation time is required. This approach provides a good preliminary computational tool that is valid in the absence of strong viscous-inviscid flow interaction.

The second approach utilizes an interactive boundary layer (IBL) method. The essential components of the IBL method are an inviscid-flow algorithm coupled with a boundary-layer algorithm. The basis for this procedure was originated by Prantl,[12] who considered the high Reynolds number flow field to be mainly inviscid except for a viscous boundary layer near the airfoil and a viscous wake behind the airfoil. The principal interaction between

the boundary layer, wake and external inviscid flow arises from displacement thickness effects leading to a a thickened semi-infinite equivalent body which can cause significant changes in the surface pressure and forces. Separate systems of equations can be solved for the external inviscid flow and for the boundary layer and wake. The boundary-layer equations for the boundary layer and wake can be solved with finite-difference or integral methods. The external inviscid flow can be represented by one of the nonlinear inviscid approximations which have been mentioned earlier. The matching can be implemented at one of three different surfaces: 1) the surface of the airfoil and wake centerline, 2) the equivalent displacement surface, 3) the edge of the boundary layer. Reviews of matching procedures for the two separate systems can be found in references by Melnik,[13] LeBalleur,[14] and Lock and Firmin.[15]

The third approach is to solve the mass-averaged Navier-Stokes equations or thin-layer Navier-Stokes (TLNS) equations. The TLNS equations are obtained by neglecting all streamwise derivatives of the viscous terms, conductive heat-flux terms, and any term involving mixed derivatives from the full Navier-Stokes equations. These neglected terms generally cannot be resolved with the available grid resolution. Recent work by Visbal and Shang[16] clearly indicates that the TLNS approximation produces essentially the same results as the full Navier-Stokes equations. This third approach (Navier-Stokes) is more expensive but imposes less theoretical restrictions than the other approaches.

Until now, transonic porous airfoils or transonic airfoils with mass transfer have been studied numerically only by the first two approaches. Savu and Trifu[17] and Savu, Trifu and Dumitrescu[8] have computed the flow about a porous NACA 0012 airfoil and a NACA 64A205.5 airfoil using the first ap-

proach (solving the transonic small-perturbation potential equation). Their results show that the standing shock can be eliminated completely by choosing the appropriate distribution of porosity for a given Mach number. The porosity was distributed from near the leading edge to the trailing edge.

Mildly separated transonic flows over porous airfoils have been studied by Olling[18] via the second approach. An integral method was applied to the boundary layer equations and a full-potential solver was used for the inviscid flow. A slight improvement in airfoil performance due to porosity was found in this study.

Shock wave/laminar boundary layer interaction with mass transfer (via the second approach) has also been studied by Ram et al.[19] The boundary layer equations were solved by an integral method with attention to necessary modification in boundary conditions for flows with mass transfer through the surface. The zonal approach was adopted for solving different equations in different zones. The results indicate that full-chord laminar flow can be maintained and separation can be prevented by the use of suitable suction.

Recently, Inger and Nandanan[20] presented a nonasymptotic triple deck approach for shock/turbulent boundary layer interaction (SBLI) that included the effect of wall suction confined to the SBLI zone. It was found that both displacement thickness and momentum thickness were increased along the aft portion of airfoil at low suction rates. This work (employing the second approach) was limited to unseparated flow, and suction effects on the shock position were neglected.

Motivation

The aforementioned experimental and theoretical results indicate that porous surfaces can affect an airfoil performance at transonic speeds. Unlike a supercritical airfoil whose fixed shape is designed for certain optimum Mach number and angle-of-attack ranges, a porous airfoil can be adjusted without changing its contour shape. The adjustments achieved from variable surface porosity may result in improved performance over a wide range of conditions. Experimental demonstration of the possible gains has been hampered by uncertainties arising from wall and support interference in transonic wind tunnels. Theoretical evaluation is impaired by the absence of a complete theory for flow over a transonic airfoil with mass transfer. In view of the importance of the problem and the improving computer capabilities, it seems worthwhile to continue the numerical investigations.

The purpose of the present study is to achieve improved computations of transonic flow over porous airfoils. An inviscid code, an IBL procedure, and a TLNS procedure are employed. To the author's knowledge, no previous work has brought these procedures to bear on the problem at hand.

The inviscid code TAIR, originally developed by Holst,[21] solves the conservative, transonic full-potential equation using an approximate factorization algorithm (AF2). The IBL procedure TRIVIA, developed by Van Dalsem and Steger,[22-23] consists of a direct-inverse, finite-difference boundary-layer algorithm coupled with TAIR. The TLNS procedure ARC2D, developed at NASA Ames Research Center,[24] is based on the Beam and Warming implicit approximate factorization algorithm with several further improvements.

Chapter II includes a description of the inviscid governing equations,

solution algorithm, and treatment of boundary conditions for transpiration at the airfoil surface. In Chapter III, the viscous boundary layer equations, the modified algorithm for the boundary layer equations, the modified viscous-inviscid interaction algorithm, and the Cebeci turbulence model are described. Chapter IV includes a description of the TLNS equations, the algorithm, and a modified version of the Baldwin-Lomax turbulence model. The cavity-flow solver and porosity modeling are described in Chapter V. The numerical results are discussed in Chapter VI. The conclusions from this work and recommendations for future work are presented in Chapter VII.

CHAPTER II

INVISCID FLOW SOLUTION

Transonic Full-Potential Equation

Because the changes of density, velocity and temperature across a shock are first order but the entropy jump across the shock is third order,[25] inviscid transonic flow can be reasonably approximated as an isentropic and irrotational flow when the Mach number ahead of the shock (M_1) is less than 1.3.[26] This assumption allows the flow to be described by a potential Φ which satisfies the continuity equation

$$(\rho\Phi_x)_x + (\rho\Phi_y)_y = 0 \tag{2.1a}$$

$$\rho = \left[1 - \frac{\gamma - 1}{\gamma + 1}(\Phi_x^2 + \Phi_y^2)\right]^{\frac{1}{\gamma - 1}} \tag{2.1b}$$

where x and y are Cartesian coordinates nondimensionalized by the airfoil chord length c; ρ and Φ_x ,Φ_y are the density and velocity components nondimensionalized by the stagnation density ρ_s and the critical sound speed a^*, respectively; and γ is the ratio of specific heats.

For computational convenience, the governing equations are transformed from the physical domain (Cartesian coordinates) to a computational domain by the transformation

$$\xi = \xi(x,y) \qquad \eta = \eta(x,y)$$

The full-potential equation written in the ξ-η computational domain is given by

$$\left(\frac{\rho U}{J}\right)_{\xi} + \left(\frac{\rho V}{J}\right)_{\eta} = 0 \tag{2.2a}$$

$$\rho = \left[1 - \frac{\gamma - 1}{\gamma + 1}(U\Phi_{\xi} + V\Phi_{\eta})\right]^{\frac{1}{\gamma - 1}} \tag{2.2b}$$

where

$$U = A_1\Phi_{\xi} + A_2\Phi_{\eta} \qquad V = A_2\Phi_{\xi} + A_3\Phi_{\eta}$$

$$A_1 = \xi_x^2 + \xi_y^2$$

$$A_2 = \xi_x\eta_x + \xi_y\eta_y$$

$$A_3 = \eta_x^2 + \eta_y^2$$

and

$$J = \xi_x\eta_y - \xi_y\eta_x$$

The variables U and V are the contravariant velocity components along the ξ and η directions, respectively; A_1, A_2, and A_3 are metric quantities; and J is the Jacobian of the transformation. This transformation maintains the strong conservation-law form of the original equation and hence possesses characteristics suitable for a shock-capture scheme. The A_1 and A_3 metrics provide a measure of cell aspect ratio. The A_1 metric is approximately the

ratio of arc length along the η-direction to arc length along the ξ-direction. The A_3 metric is approximately the inverse of A_1, and A_2 is a measure of orthogonality. The Jocobian, J, can be shown to approximate the inverse of cell area.

Numerical Algorithm

The numerical algorithm and code, TAIR, developed by Holst[21] are capable of simulating inviscid flow about an airfoil (with weak shocks) by solving the transonic full-potential equation in body-fitted coordinates using an AF2 scheme. This code provides rapid convergence and requires only a few seconds of computer time per case on a CRAY-XMP processor.

The AF2 fully implicit scheme can be expressed as

$$(\alpha - \overrightarrow{\delta_\eta} A_j)(\alpha \overrightarrow{\delta_\eta} - \overrightarrow{\delta_\xi} A_i \overrightarrow{\delta_\xi}) C^n_{i,j} = \alpha\omega L\Phi^n_{i,j} \tag{2.3}$$

in which $C^n_{i,j} = \Phi^{n+1}_{i,j} - \Phi^n_{i,j}$, α is an acceleration parameter, ω is a relaxation parameter$(2 \geq \omega \geq 0)$ and A_i and A_j are defined by

$$A_i = \left(\frac{\tilde{\rho} A_1}{J}\right)_{i-\frac{1}{2},j} \qquad A_j = \left(\frac{\bar{\rho} A_3}{J}\right)_{i,j-\frac{1}{2}}$$

The scheme is implemented in a two-step format. In step 1, a scalar bidiagonal matrix is inverted for each ξ = constant line and in step 2, a scalar tridiagonal matrix is solved for each η = constant line.

The residual $L\Phi^n_{i,j}$ on the right-hand side of Eq. (2.3) is given by

$$\overleftarrow{\delta}_\xi \left(\frac{\tilde{\rho} U}{J}\right)_{i+\frac{1}{2},j} + \overleftarrow{\delta}_\eta \left(\frac{\bar{\rho} V}{J}\right)_{i,j+\frac{1}{2}}$$

where $\overleftarrow{\delta}_\xi$ and $\overleftarrow{\delta}_\eta$ are first-order accurate, backward-difference operators in the ξ and η directions, respectively. The artificial density scheme consists of

introducing an upwind evaluation of the density in ξ and η directions (denoted by $\tilde{\rho}$ and $\bar{\rho}$). Basically, the supersonic regions are stabilized using an upwind bias of the density. This provides an efficient and reliable spatial differencing scheme for the capture of weak (transonic) shock waves. Details of this scheme can be found in Refs. [21,27].

There is an entropy-correction option in the TAIR code which involves replacing the isentropic density ρ_i by

$$\rho = \rho_i e^{-\Delta S/R}$$

The normalized entropy change $(\Delta S/R)$ can be approximated by a locally one-dimensional shock relation which is a function of M_1 (the Mach number upstream of the shock).

$$\frac{\Delta S}{R} \approx \frac{2\gamma}{3(\gamma+1)^2}(M_1{}^2 - 1)^3 \tag{2.4}$$

Another feature of the TAIR code is its ability to capture free-stream flow in general curvilinear coordinates. Three free-stream consistency conditions are required for free-stream capturing. The reader is referred to Ref. [28] for complete details.

The body-fitted grids used for the full-potential solver are generated by the finite-difference solution of Poisson equations using a computer code (GRAPE) developed by Sorenson[29] and based on the work of Steger and Sorenson.[30] Two sets of Poisson equations are solved using the successive line over-relaxation procedure. This grid generation code allows control of the grid point spacing along and normal to the boundaries as well as the angles at which grid lines intersect the boundaries. The C-mesh grid topology used in this study is shown in Fig. 2.1. A typical inviscid grid is shown in Fig. 2.2.

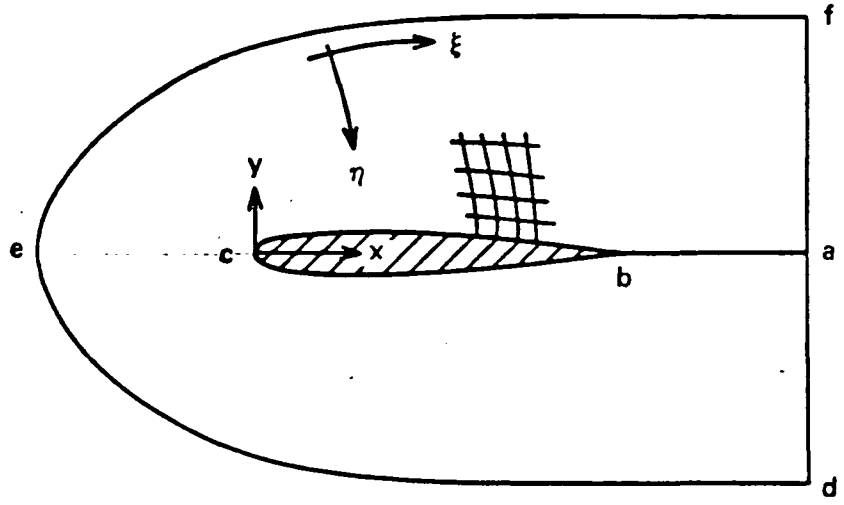

(a) PHYSICAL DOMAIN

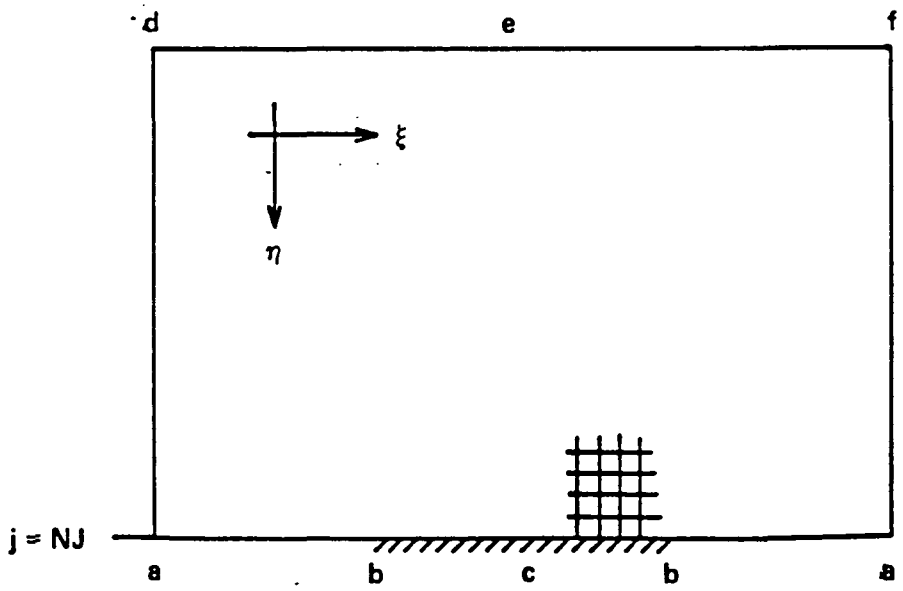

(b) COMPUTATIONAL DOMAIN

Fig. 2.1 C-grid topology for numerical computation.

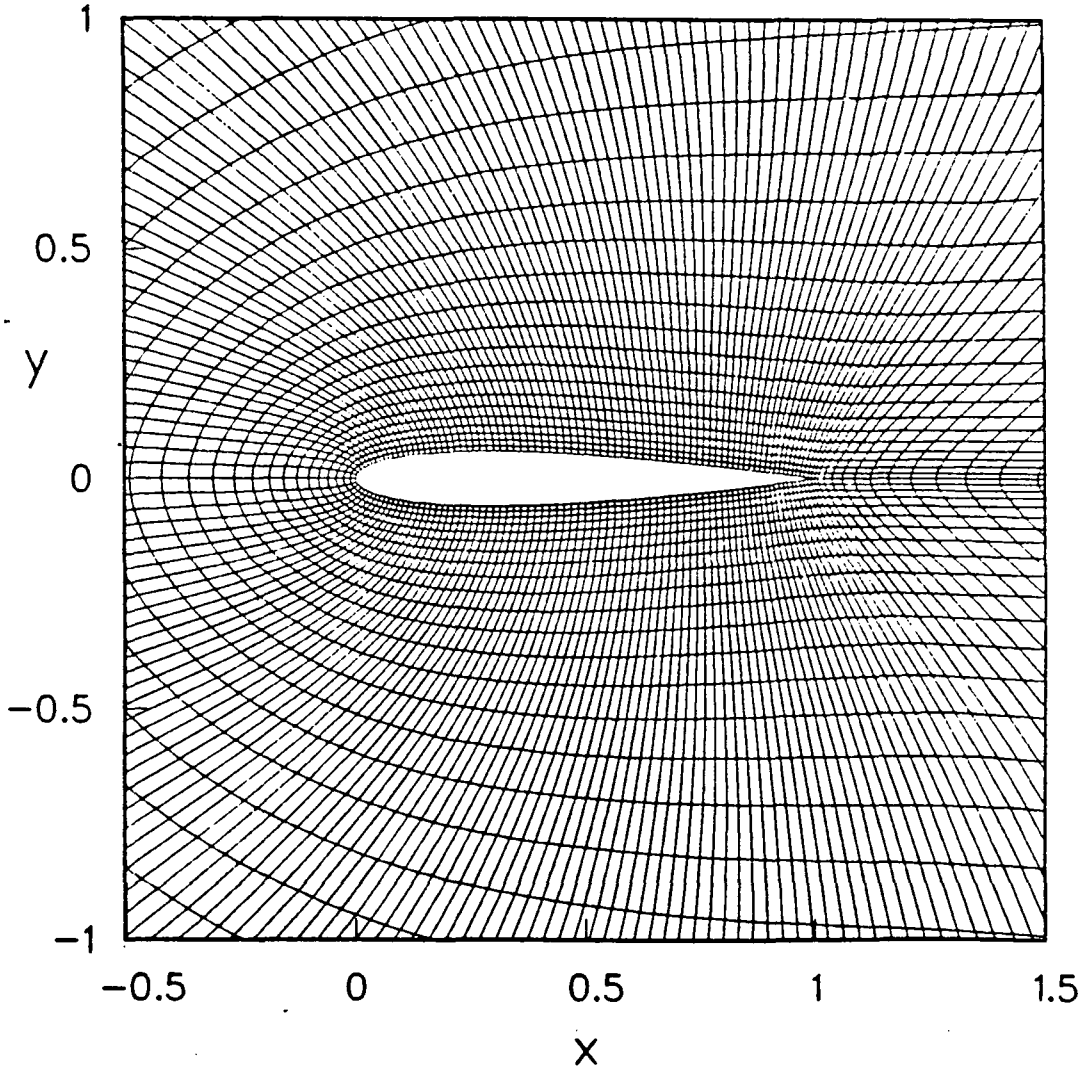

Fig. 2.2 Grid used for inviscid-flow calculation.

Boundary Conditions

The boundaries associated with the physical domain are transformed to boundaries of the computational domain. At the outer boundary, the velocity potential is set to be the sum of the uniform free-stream component and the component caused by a vortex with circulation Γ, where Γ is the jump in the velocity potential at the airfoil's trailing edge. At the airfoil surface, there are two types of boundary conditions depending on the surface property (solid or porous).

1. On solid regions of the airfoil, the flow tangency condition is satisfied by requiring that the contravariant velocity component in the η-direction vanish.

$$V = 0 \qquad \text{on solid surfaces} \tag{2.5}$$

2. On porous regions of the airfoil, the normal wall velocity v_n does not vanish and its value is determined by porosity modeling, which will be introduced in Chapter V.

The physical transpiration velocity v_n is then transformed into the computational domain:

$$\begin{bmatrix} V \\ U \end{bmatrix} = - \begin{bmatrix} \sqrt{A_3} & 0 \\ \frac{A_2}{\sqrt{A_3}} & \frac{J}{\sqrt{A_3}} \end{bmatrix} \begin{bmatrix} v_n \\ 0 \end{bmatrix} \tag{2.6}$$

where the negative sign is due to the use of a left handed coordinate system. With the C-mesh topology, the η-coordinate lines intersect the body at close to right angles and, to a good approximation, $A_2 = 0$ at the body. Using this approximation v_n does not contribute to U and can be expressed in the computational domain as:

$$V = -\sqrt{A_3} v_n \qquad \text{on the porous surface} \tag{2.7}$$

Numerical implementation of the boundary conditions on the airfoil surface is summarized as follows:

1. On the solid portion of the airfoil, the flow tangency boundary condition (i.e., $V = 0$) is used to obtain

$$\left(\frac{\rho V}{J}\right)_{i,NJ+\frac{1}{2}} = -\left(\frac{\rho V}{J}\right)_{i,NJ-\frac{1}{2}} \tag{2.8}$$

where $j = NJ$ is the airfoil surface (Fig. 2.1).

2. On the porous portion of the airfoil, the boundary condition (i.e., $V = -\sqrt{A_3}v_n$) is applied with the aid of a Taylor series expansion

$$\left(\frac{\rho V}{J}\right)_{i,NJ\pm\frac{1}{2}} = \left(\frac{\rho V}{J}\right)_{i,NJ} \pm \frac{\Delta\eta}{2}\left(\frac{\rho V}{J}\right)'_{i,NJ} + \frac{(\Delta\eta)^2}{8}\left(\frac{\rho V}{J}\right)''_{i,NJ} \pm O[(\Delta\eta)^3] \tag{2.9}$$

so that the first-order boundary condition becomes

$$\left(\frac{\rho V}{J}\right)_{i,NJ+\frac{1}{2}} = -\left(\frac{\rho V}{J}\right)_{i,NJ-\frac{1}{2}} + 2\left(\frac{\rho V}{J}\right)_{i,NJ} \tag{2.10}$$

In fact, Eq. (2.8) is a special case of Eq. (2.10) for $V = 0$ at $j = NJ$.

Equation (2.2), together with the surface boundary conditions [Eqs. (2.8) and (2.10)] and appropriate outer boundary conditions, are solved numerically using the modified TAIR computer code. At the beginning of each iteration, the porous boundary condition is updated by porosity modeling. Once the flow field is obtained, forces on the airfoil in the x and y directions can be computed by performing integrations around the airfoil contour

$$F_x = \int_S (pn_x + \rho v_n u)ds \tag{2.18}$$

$$F_y = \int_S (pn_y + \rho v_n v) ds \tag{2.19}$$

in which S is the circumference of the airfoil; u and v are velocity components in the x and y directions, respectively; p is pressure; and n_x and n_y are direction cosines between the airfoil surface and the x and y directions, respectively. Equations (2.18) and (2.19) are derived from the momentum conservation theorem. Note that the second term in both equations ($\rho v_n u$ and $\rho v_n v$) are zero for solid wall airfoils but must be retained in the present calculations because of the porous wall assumption. Once F_x and F_y are obtained from Eqs. (2.18) and (2.19), the lift and drag coefficients, C_L and C_D, are easily computed.

The drag components of a two-dimensional airfoil are wave drag, viscous pressure drag, friction drag and pump drag. At this stage, the only drag component evaluated is wave drag because viscous effects are neglected and no power is supplied.

CHAPTER III

INTERACTIVE BOUNDARY LAYER PROCEDURE

A finite-difference viscous-inviscid interaction algorithm is modified to simulate the viscous transonic flow over porous airfoils in the presence of mild separation. The code consists of a direct-inverse, finite-difference boundary layer algorithm coupled with the full-potential solver described in Chapter II. A viscous-inviscid interaction algorithm is used. For the present work, major modifications in this procedure are associated with the forcing function, the boundary condition treatment, the viscous/inviscid interaction algorithm, integration of the continuity equation, and the turbulence model.

Governing Equations

The nondimensionalized, first-order compressible turbulent boundary layer equations for the steady, two-dimensional flow of a perfect gas are:

x-momentum equation

$$\rho(uu_x + vu_y) = -\beta p_x + ((\mu_l + \mu_t)u_y)_y \tag{3.1a}$$

energy equation

$$\rho c_p(uT_x + vT_y) = \beta u p_x + ((\kappa_l + \kappa_t)T_y)_y + (\mu_l + \mu_t)(u_y)^2 \tag{3.1b}$$

perfect gas equation

$$p = \rho T \tag{3.1c}$$

continuity equation

$$(\rho u)_x + (\rho v)_y = 0 \tag{3.1d}$$

where x, y are along and normal to the body or wake centerline, respectively. Viscosity, pressure, temperature, and density are nondimensionalized by their free-stream values. The u and x variables are nondimensionalized by the free-stream velocity and a characteristic length, respectively, whereas the v and y variables are nondimensionalized by the same quantities divided by $\sqrt{Re_\infty}$. In Eq. (3.1), $\beta = (p/\rho U^2)_\infty$, μ_l and κ_l are molecular viscosity and conductivity determined by the Sutherland viscosity law and a constant Prandtl number assumption, μ_t and κ_t are eddy viscosity and conductivity determined by turbulence modeling. These equations are simplified from the Reynolds equations with use of the Boussinesq approximation, that is,

$$-\overline{\rho u'v'} = \mu_t u_y \tag{3.1e}$$

$$-c_p\overline{\rho v'T'} = \kappa_t T_y \tag{3.1f}$$

Experiments confirm that the ratio of the diffusivities for the turbulent transport of heat and momentum, called the turbulent Prandtl number, $Pr_t = \mu_t c_p/\kappa_t$, is a well-behaved function across the flow. Most algebraic turbulence models set $Pr_t = 0.9$ such that only μ_t needs modeling.

To solve the boundary-layer equations using finite-difference approximations, it is necessary to construct a grid. In the interest of accuracy and computational efficiency, it is desirable to use a non-uniform grid. However, if Eqs. (3.1a-3.1d) are differenced on a non-uniform grid, complicated variable-spacing finite-difference operators must be used. On the other hand, if a general x, y to $\xi(x), \eta(x, y)$ coordinate transformation is applied to the boundary-layer equations, a non-uniform x, y grid may be used while the equations can be solved on a uniform ξ, η grid. In other words, the physical domain x, y grid is adapted to resolve the flow field, while the computational domain ξ, η grid

is chosen so that simple equal-spaced finite-difference operators may be used. Hence, although the equations are slightly more complicated after the coordinate transformation, overall the finite-difference solution of the equations becomes much simpler.

For computational convenience, the boundary-layer equations are transformed from the physical x, y domain to a uniform $\xi(x), \eta(x, y)$ computational domain:

x-momentum equation

$$\rho[u(u_\xi \xi_x + u_\eta \eta_x) + v u_\eta \eta_y] = -\beta p_\xi \xi_x + ((\mu_l + \mu_t) u_\eta \eta_y)_\eta \eta_y \qquad (3.2a)$$

energy equation

$$\rho c_p[u(T_\xi \xi_x + T_\eta \eta_x) + v T_\eta \eta_y] = \beta u p_\xi \xi_x + ((\kappa_l + \kappa_t) T_\eta \eta_y)_\eta \eta_y + (\mu_l + \mu_t)(u_\eta \eta_y)^2 \qquad (3.2b)$$

perfect gas equation

$$p = \rho T \qquad (3.2c)$$

continuity equation

$$(\rho u)_\xi \xi_x + (\rho u)_\eta \eta_x + (\rho v)_\eta \eta_y = 0 \qquad (3.2d)$$

Moreover, it is also frequently assumed that the stagnation enthalpy is constant across the boundary layer in the case of low- to moderate- speed air flow over an adiabatic surface. This approximation does not introduce large errors provided the Mach number M_e at the boundary-layer edge is moderate (the actual variation of stagnation enthalpy across an adiabatic boundary-layer is approximately equal to 4% when $M_e = 2$). Therefore the energy equation can be replaced by a simple algebraic relation ($H = c_p T + u^2/2 =$ constant), and an increase in computational efficiency achieved.

Numerical Algorithm

The finite-difference boundary-layer equations are solved using a predictor-corrector space marching algorithm with appropriate initial conditions as shown in Refs. [22-23]. However, integration of the continuity equation from the wall to obtain v (v_n can be nonzero) has been replaced by

$$\overleftarrow{\delta_\eta}(\rho v) = -\frac{1+E_\eta^{-1}}{2}\frac{\xi_x\delta_\xi(\rho u)+\eta_x\delta_\eta(\rho u)}{\eta_y} \tag{3.3}$$

where E is the shift operator (e.g. $E_\eta{}^1 u_k = u_{k-1}$), $\overleftarrow{\delta_\eta} = 1 - E_\eta^{-1}$, $\delta_\xi = (E_\xi - E_\xi^{-1})/2$, and $\delta_\eta = (E_\eta - E_\eta^{-1})/2$. This procedure is simpler than the original version. Since the boundary-layer equations are weakly coupled, they are solved in a sequential manner at each streamwise station. Overall, second-order accurate solutions are obtained at the cost of a few scalar bidiagonal and scalar tridiagonal matrix inversions per streamwise station rather than at least one block tridiagonal inversion per marching step of the box scheme. Both direct and semi-inverse interactions are built into the code. For attached flow, pressure is specified in the direct mode. However, near and in the reverse-flow regions, in order to avoid the Goldstein singularity, the wall shear τ_w and wake-centerline velocity u_{wc} are specified in the inverse mode.

By applying the x-momentum equation at the porous wall ($u_w = 0, v_n \neq 0$), one can obtain a relation :

$$\beta\xi_x p_\xi = (\mu u_\eta \eta_y)_\eta \eta_y \mid_w - \rho v u_\eta \eta_y \mid_w \tag{3.4}$$

This expression allows us to eliminate the term $\beta\xi_x p_\xi$ from the differenced x-momentum equation and to put τ_w into that equation by the following approximation:

$$\beta \xi_x p_\xi = \frac{2\left(\frac{\eta_{y_2}+\eta_{y_1}}{2}\right)\left(\frac{\mu_2+\mu_1}{2}\right)\frac{u_2-u_1}{y_2-y_1} - 2\tau_w}{y_2 - y_1} - \rho v_n \frac{\tau_w}{\mu_1} \tag{3.5}$$

where subscripts 1 and 2 correspond to the wall and one grid away from the wall, respectively. Since these inverse forcing functions are cast in a general form, they can be applied to either a solid surface or a porous surface. In the inverse mode, τ_w is updated by the following viscous-inviscid interaction algorithm :

$$\tau_w^{n+1} = \tau_w^n + \omega(p_v^n - p_i^{n+1})\xi_x \tag{3.6a}$$

The acceleration parameter ω is gradually increased to avoid the high frequency error which occurs during the first few iterations. A similar procedure is used to update the wake centerline velocity.

$$u_w^{n+1} = u_{wc}^n + \omega_c(p_v^n - p_i^{n+1})\xi_x \tag{3.6b}$$

The quantity $\omega\xi_x$ varies in a range near ten and $\omega_c\xi_x$ varies near two.

Viscous effects are introduced into the inviscid solver via a transpiration velocity $\bar{v}_n$ determined from the boundary-layer solution

$$\bar{v}_n = \frac{1}{\rho_e}\left(\frac{\partial(\rho_e u_e \delta^*)}{\partial s} + \rho_w v_n\right) \tag{3.7}$$

where v_n is the surface blowing (or suction) velocity determined from porosity effects, ρ_e and u_e are the inviscid values at the airfoil (or wake centerline). This equation is derived by considering the difference between the continuity equations for inviscid and viscous flow,[15] that is

$$\frac{\partial}{\partial s}(\rho_i u_i - \rho u) + \frac{\partial}{\partial n}(\rho_i v_i - \rho v) = 0 \tag{3.8}$$

where subscript i denotes inviscid quantity. Integrating across the boundary layer, from n = 0 to δ, one can obtain Eq. (3.7), since both $(\rho_i v_i - \rho v)$ and $(\rho_i u_i - \rho u)$ vanish at $n = \delta$ due to the matching condition. The transpiration velocity $\bar{v}_n$ is imposed at the airfoil surface in the inviscid flow solver (see Fig. 3.1). This interaction procedure avoids supercritical behavior and the the need for inviscid-grid generation at each iteration. As LeBalleur[31] indicated, the supercritical behavior has no physical significance and can be controlled solely by the choice of the matching condition coupling the inviscid and boundary layer equations. In Fig. 3.1, the ξ^i, η^i coordinate system is for the inviscid-flow solver and the ξ, η solution-adaptive coordinate system is for the boundary-layer solver. The total grid height for the viscous turbulent flow is a function of computed displacement thickness:

$$y_{max} = \sigma \delta^*_{i-1} \left(\frac{x_i}{x_{i-1}} \right)^{\frac{6}{7}} \tag{3.9}$$

where $\sigma \approx 5$. The viscous grid is generated by an exponential stretching function:

$$y_j = y_{j-1} + \Delta y_{min}(1 + \epsilon)^{j-2} \tag{3.10}$$

The first grid point above the airfoil is placed at approximately $y^+ = 1$ (which determines ϵ).

Once $\bar{v}_n$ is known, the numerical boundary condition is applied as in Chapter II except v_n in Eqs. (2.7-2.8) is replaced by $\bar{v}_n$. The complete interaction scheme is indicated in Fig. 3.2. From this IBL procedure, the skin friction and viscous pressure drags are evaluated in addition to the the wave drag.

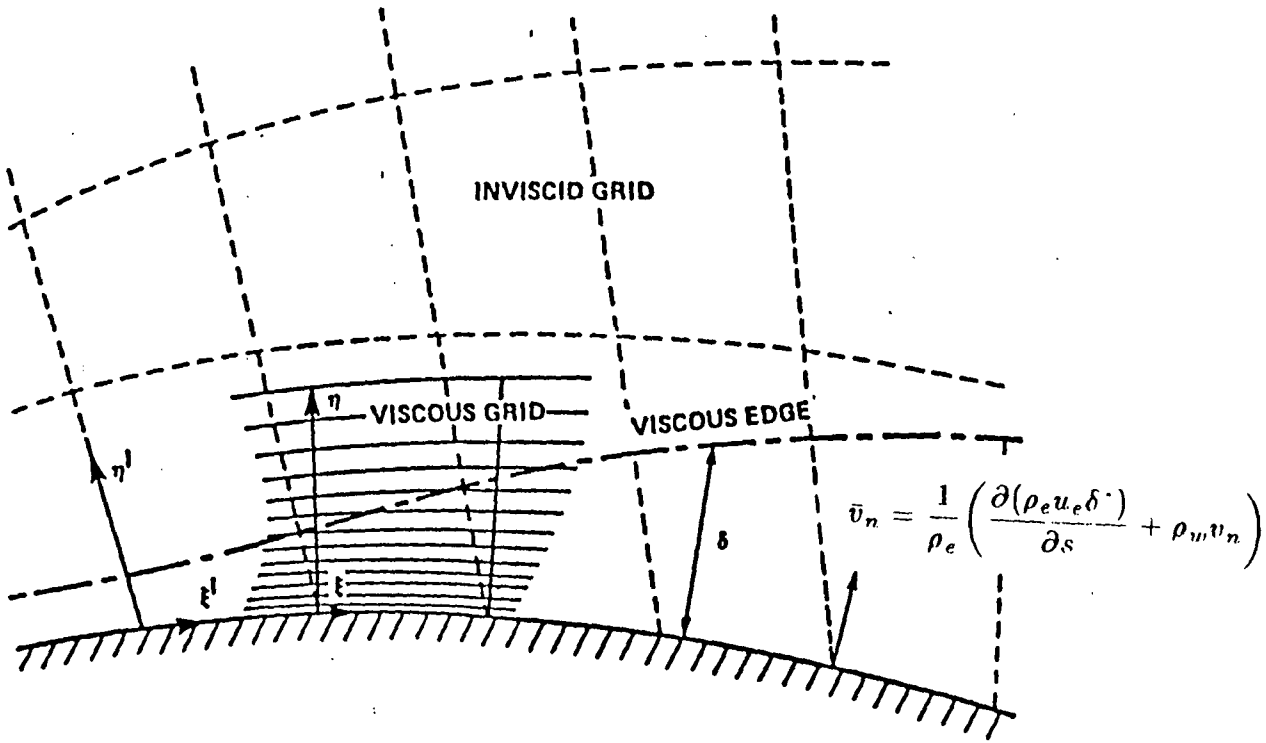

Fig. 3.1 Viscous-grid topology and transpiration velocity concept.

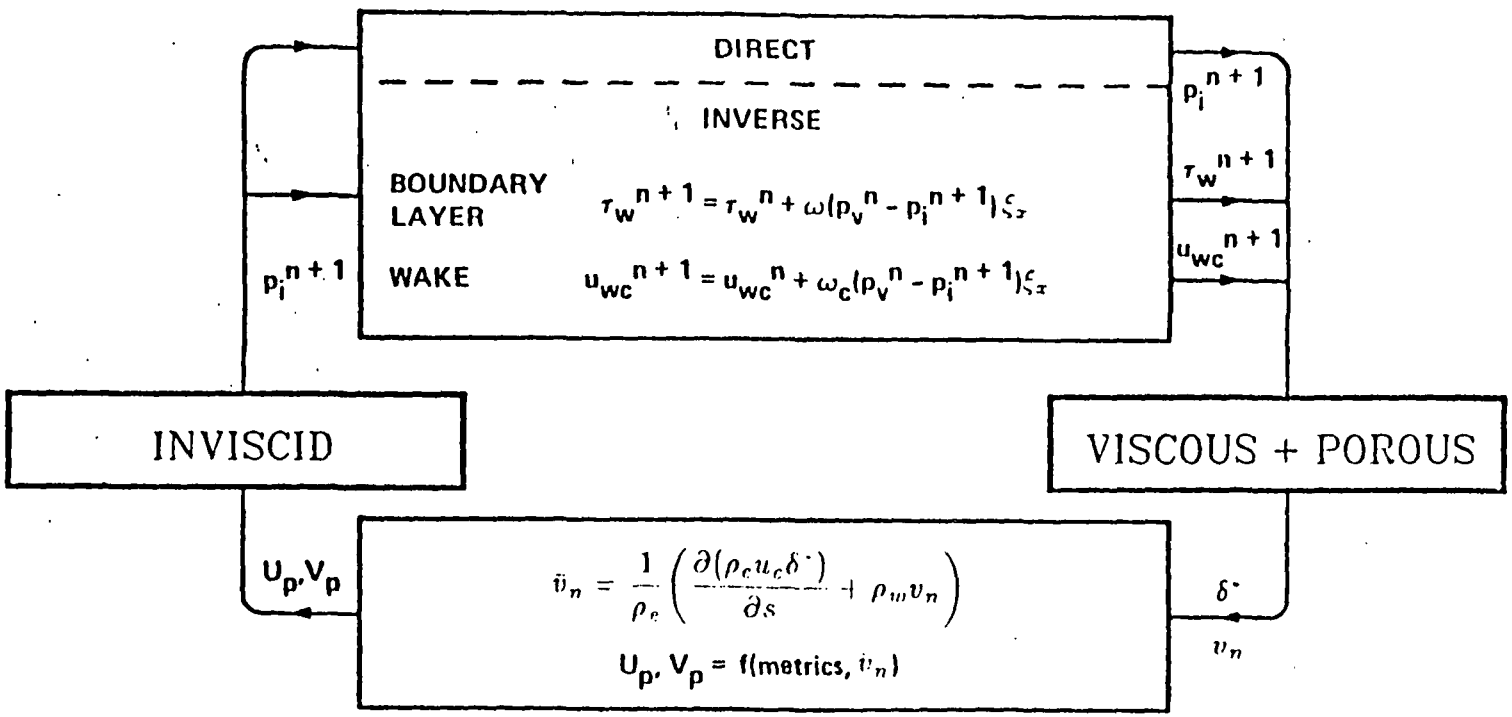

Fig. 3.2 Complete interaction scheme.

Turbulence Model

The turbulence model used in the IBL procedure is the Cebeci two-layer algebraic turbulence model. The Prandtl formulation used in the inner layer is,

$$(\mu_t)_{inner} = \rho l^2 \left|\frac{\partial u}{\partial y}\right| \tag{3.11}$$

The mixing length , l , is evaluated from

$$l = \kappa y(1 - e^{y^+/A^+}) \tag{3.12a}$$

The quantity y^+ is given by $y^+ = yu_\tau/\nu$, and the friction velocity u_τ by $u_\tau = (\tau_w/\rho)^{1/2}$. In Eq. (3.12a) κ is the von Kármán constant usually taken as 0.41 and A^+ is the damping constant most commonly evaluated as 26. Cebeci extended Van Driest's modeling of the viscous sublayer and let A^+ be a function of v^+ , p^+, μ_e and ρ_e(subscript e denotes the edge of boundary layer). Here $v^+ = v_n/u_\tau$ and $p^+ = (dp/dx)(\nu/\rho u_\tau{}^3)$. The Clauser formulation used in the outer layer is

$$(\mu_t)_{outer} = 0.0168\rho u_e \delta^* \tag{3.12b}$$

where u_e is the velocity at the edge of boundary layer and δ^* is given by

$$\delta^* = \int_0^\delta (1 - \frac{u}{u_e})dy \tag{3.12c}$$

The outer value $(\mu_t)_{outer}$ is used at all values of y beyond the point where $(\mu_t)_{inner}$ and $(\mu_t)_{outer}$ first cross. The reader who is interested in this model is referred to Ref. [32] for further details.

CHAPTER IV

THIN-LAYER NAVIER-STOKES PROCEDURE

The thin-layer Navier-Stokes equations are generally referred to in the literature as TLNS equations. A main feature of these equations is the presence of a nonzero, normal-pressure gradient, which is necessary to couple and solve simultaneously the viscous and inviscid regions. By comparison with the Navier-Stokes equations, these composite equations require less computational effort because they contain fewer terms. However, the thin layer approximation is invalid at low Reynolds numbers and in regions of massive flow separation.

Governing Equations

Again for computational convenience, the governing equations are transformed from Cartesian coordinates to general curvilinear coordinates by the transformation

$$\begin{aligned} \tau &= t \\ \xi &= \xi(x, y, t) \\ \eta &= \eta(x, y, t) \end{aligned} \tag{4.1}$$

The conservative thin layer Navier-Stokes equations expressed in terms of Reynolds mass-averaged variables in general curvilinear coordinates (ξ, η) and time τ can be written as

$$\partial_\tau \widehat{Q} + \partial_\xi \widehat{E} + \partial_\eta \widehat{F} = Re^{-1} \partial_\eta \widehat{S} \tag{4.2}$$

where

$$\widehat{Q} = J^{-1}\begin{bmatrix}\rho\\ \rho u\\ \rho v\\ e\end{bmatrix}, \quad \widehat{E} = J^{-1}\begin{bmatrix}\rho U\\ \rho uU + \xi_x p\\ \rho vU + \xi_y p\\ U(e+p) - \xi_t p\end{bmatrix},$$

$$\widehat{F} = J^{-1}\begin{bmatrix}\rho V\\ \rho uV + \eta_x p\\ \rho vV + \eta_y p\\ V(e+p) - \eta_t p\end{bmatrix}$$

with

$$U = \xi_t + \xi_x u + \xi_y v$$

$$V = \eta_t + \eta_x u + \eta_y v$$

and

$$\widehat{S} = J^{-1}\begin{bmatrix}0\\ \eta_x m_1 + \eta_y m_2\\ \eta_x m_2 + \eta_y m_3\\ \eta_x(um_1 + vm_2 + m_4) + \eta_y(um_2 + vm_3 + m_5)\end{bmatrix}$$

wherein

$$m_1 = \mu(4\eta_x u_\eta - 2\eta_y v_\eta)/3$$

$$m_2 = \mu(\eta_y u_\eta + \eta_x v_\eta)$$

$$m_3 = \mu(-2\eta_x u_\eta + 4\eta_y v_\eta)/3$$

$$m_4 = \mu Pr^{-1}(\gamma - 1)^{-1}\eta_x \partial_\eta(a^2)$$

$$m_5 = \mu Pr^{-1}(\gamma - 1)^{-1}\eta_y \partial_\eta(a^2)$$

Pressure is related to the conservative flow variables, Q, by the equation of state

$$p = (\gamma - 1)\left[e - \frac{1}{2}\rho(u^2 + v^2)\right] \tag{4.3}$$

where γ (=1.4) is the ratio of specific heats. The speed of sound is a (for ideal fluids, $a^2 = \gamma p/\rho$). The dynamic viscosity μ is made up of an eddy viscosity (μ_t) and molecular viscosity (μ_l) which is evaluated by Sutherland's semi-empirical formula. Re is Reynolds number and μPr^{-1} represents $\mu_l Pr^{-1} + \mu_t Pr_t^{-1}$.

Numerical Algorithm

The TLNS procedure ARC2D developed at NASA Ames Research Center[15] is modified for this study. This implicit code was based on the Beam and Warming approximate-factored algorithm. Euler implicit or three-point implicit time difference and second-order central spatial difference are utilized. An artificial dissipation model was added to capture a non-oscillating shock and maintain stability. Pulliam and Chaussee[33] developed a diagonal version to reduce the block pentadiagonal inversion to 4×4 matrix multiplications and scalar pentadiagonal inversions. Also a local time step and variable grid spacing are employed to accelerate the convergence rate for the steady flow solutions. The reader who is interested in the numerical algorithm is referred to Ref. [15] for details.

Boundary Conditions and Grid

On the airfoil surface, the normal wall velocity v_n is specified and the tangential velocity is set to zero. The boundary condition on pressure at the airfoil is taken to be $\partial p/\partial \eta = 0$, since the η coordinate lines are nearly orthogonal to the airfoil surface. The adiabatic wall condition is used to obtain density at the surface and total energy is decoded from the equation of state. The far field boundary condition is set by imposing a compressible potential vortex solution on the free stream quantities.[34] All the boundary conditions are updated explicitly in the TLNS procedure.

The grid for the TLNS procedure is obtained by a hyperbolic grid-generation procedure.[35] Since the equation system used to generate the grid is hyperbolic in the η direction, the outer boundary is not specified in advance

as in the elliptic grid-generation procedure. A typical grid set for the TLNS is shown in Fig. 4.1. By comparison with the inviscid grid (Fig. 3.2), the grid spacing for the TLNS procedure is more clustered near the airfoil surface. For most of the test cases in this work, the first point above the airfoil is at $y^+ \sim O(1)$, the total number of grid points is 251×65, and the outer boundary is set at 16 chord lengths away from the airfoil.

Turbulence Model for Transpired Boundary

The Baldwin-Lomax model[36] used in the TLNS procedure is a two-layer algebraic model in which μ_t is given by

$$\mu_t = \begin{cases} (\mu_t)_{inner}, & y \leq y_{crossover} \\ (\mu_t)_{outer}, & y > y_{crossover} \end{cases} \tag{4.4}$$

where y is the normal distance from the wall and $y_{crossover}$ is the smallest value of y at which values from the inner and outer formulas are equal.

The Prandtl-Van Driest formulation is used in the inner region

$$(\mu_t)_{inner} = \rho l^2 |\omega| \tag{4.5}$$

where

$$l = ky\left[1 - exp\left(-y^+/A^+\right)\right] \tag{4.6}$$

$|\omega|$ is the magnitude of the vorticity and

$$y^+ = \frac{\rho_w u_\tau y}{\mu_w} = \frac{\sqrt{\rho_w \tau_w}\, y}{\mu_w} \tag{4.7}$$

The eddy viscosity coefficient in the outer layer is given by

$$(\mu_t)_{outer} = KC_{CP}\rho F_{WAKE} F_{KLEB}(y) \tag{4.8}$$

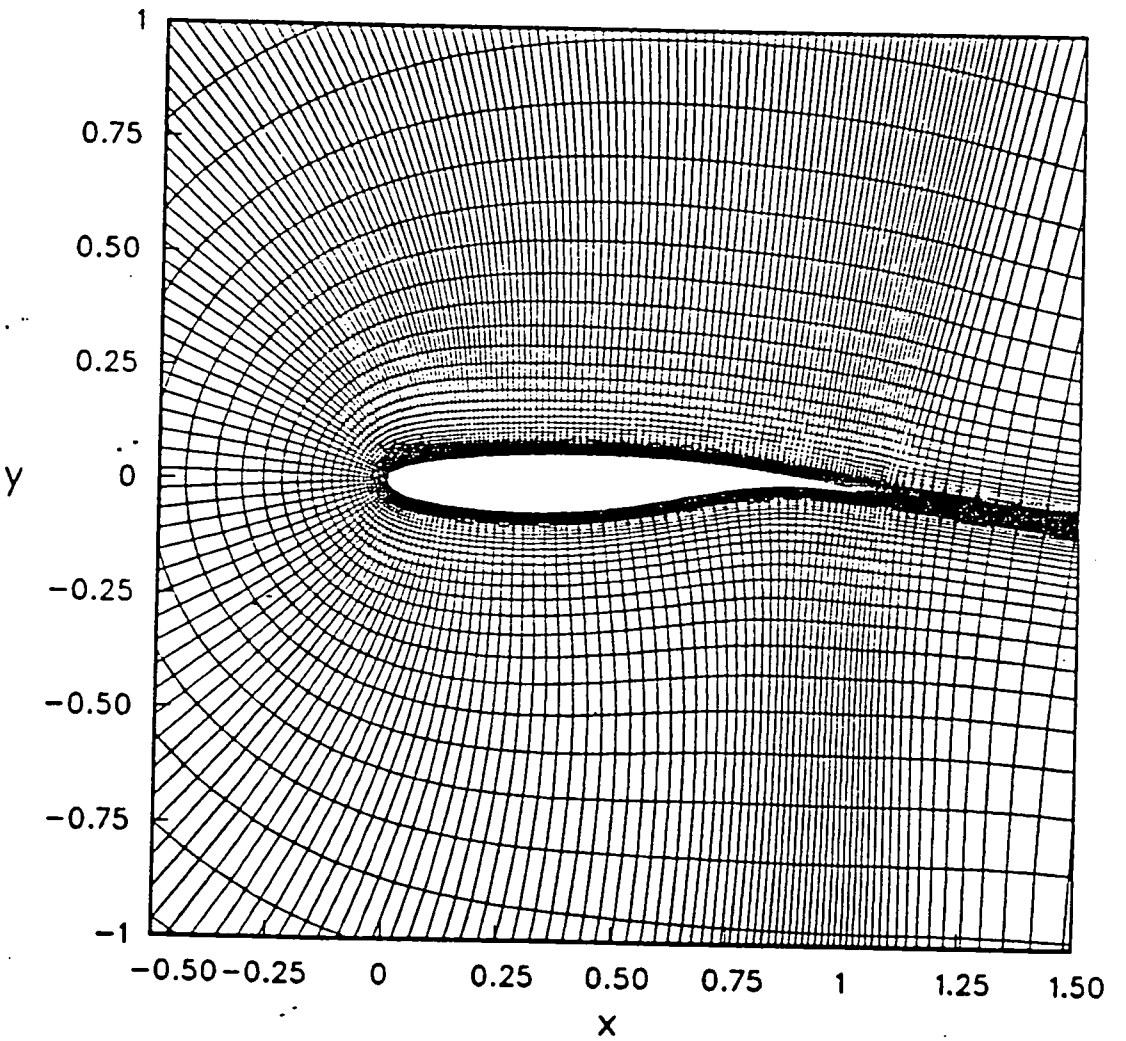

Fig. 4.1 Grid used for TLNS calculation.

where K is the Clauser constant(0.0168) and C_{CP} is an additional constant (1.6), and

$$F_{WAKE} = min \left\{ \begin{array}{c} y_{max} F_{max} \\ C_{WK} y_{max} {u_{DIF}}^2 / F_{max} \end{array} \right\} \tag{4.9}$$

$$u_{DIF} = u_{at\ y_{max}} - u_{min} \tag{4.10}$$

where $C_{WK} = 1.0$, and y_{max} and F_{max} are determined from the function

$$F(y) = y|\omega| \left[1 - exp\left(-y^+ / A^+\right)\right] \tag{4.11}$$

The quantity F_{max} is the maximum value of $F(y)$ that occurs in the profile, and y_{max} is the value of y at which it occurs. The Baldwin-Lomax model is patterned after that of Cebeci with modifications that avoid the necessity for finding the outer edge of the boundary layer. The length scales are determined by the distribution of vorticity. Since the original Baldwin-Lomax turbulence model did not consider blowing (or suction) effects on A^+, the damping factor A^+ is redefined as :[37]

$$A^+ = \frac{26}{\left(\tau^+\right)^n} \tag{4.12a}$$

where $\tau^+ = \tau / \tau_w$. In order to compare with the STAN-5 results in Refs. [38-39] near the blowing (or suction) surface, the x-momentum equation is integrated with $v = v_n = constant$, $p_x = constant$, $\rho = constant$ and uu_x neglected. The result is

$$\tau^+ \approx {\tau_w}^+ + p^+ y^+ + v^+ u^+(y^+) \tag{4.12b}$$

where p^+, y^+, v^+ and u^+ are already defined in Chapter III. Fig. 4.2 shows plots of A^+ vs. p^+ with v^+ as parameter. The symbols represent data from

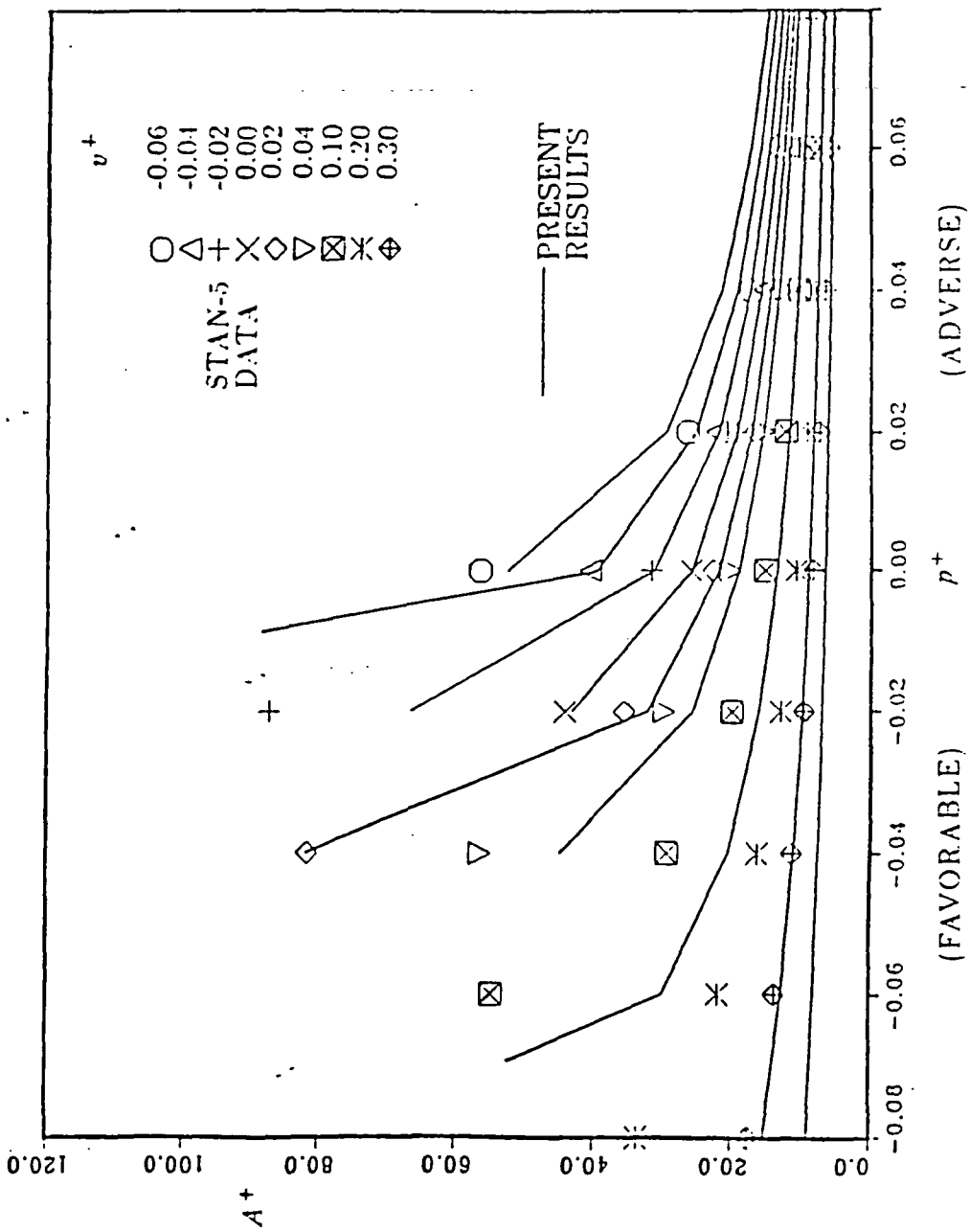

Fig. 4.2 Damping parameter A^+.

STAN-5. It is observed from Fig. 4.2 that when $p^+ \approx -0.04$, and $v^+ = 0$, A^+ goes to ∞. For agreement with this, the denominator of Eq. (4.12a) should go to zero under those conditions

$$\tau^+ = 1 - 0.04y^+ = 0$$

Thereby $y^+ = 25$ is determined and extended to other cases with $v^+ \neq 0$. The results from setting $y^+ = 25$ in Eq. (4.12b) and $n = 0.7$ in Eq. (4.12a), (μ_t is evaluated with Eqs. (4.5-4.6)) are shown as the solid lines in Fig. 4.2. It is seen that values of A^+ vs. p^+ for various v^+ from this procedure agree well with the results from STAN-5. With this modification, the dependence on boundary-layer edge quantities in the Cebeci turbulence model can be neglected. Indeed, this value of n is in the range proposed by other researchers, such as Patankar and Spalding ($n = 0.5$)[40] and Baker, Jonsson and Launder($n = 1.0$)[41]. This modification (Eq. 4.12a) has been added to the Baldwin-Lomax turbulence model, yielding skin friction values in the blowing region higher than those calculated by the original Baldwin-Lomax model. Conversely, this model predicts skin friction in the suction region lower than from the original model.

For example, for the RAE2822 airfoil at $M_\infty = 0.7$, $\alpha = 2.0$ and $Re = 6.5 \times 10^6$, with the transition position specified at 0.03 chord, and with the specified distribution of blowing shown in Fig. 4.3, the skin friction is reduced in the blowing region. But the modified version predicts slightly higher skin friction values than the Baldwin-Lomax model . The blowing effects on the C_p distribution are plotted in Fig. 4.4. The effect of blowing on the pressure predicted by the two models is the same. Next the effect of a specified suction distribution is investigated and again the two models predict the same effect on the pressure, but the increased skin friction over the suction

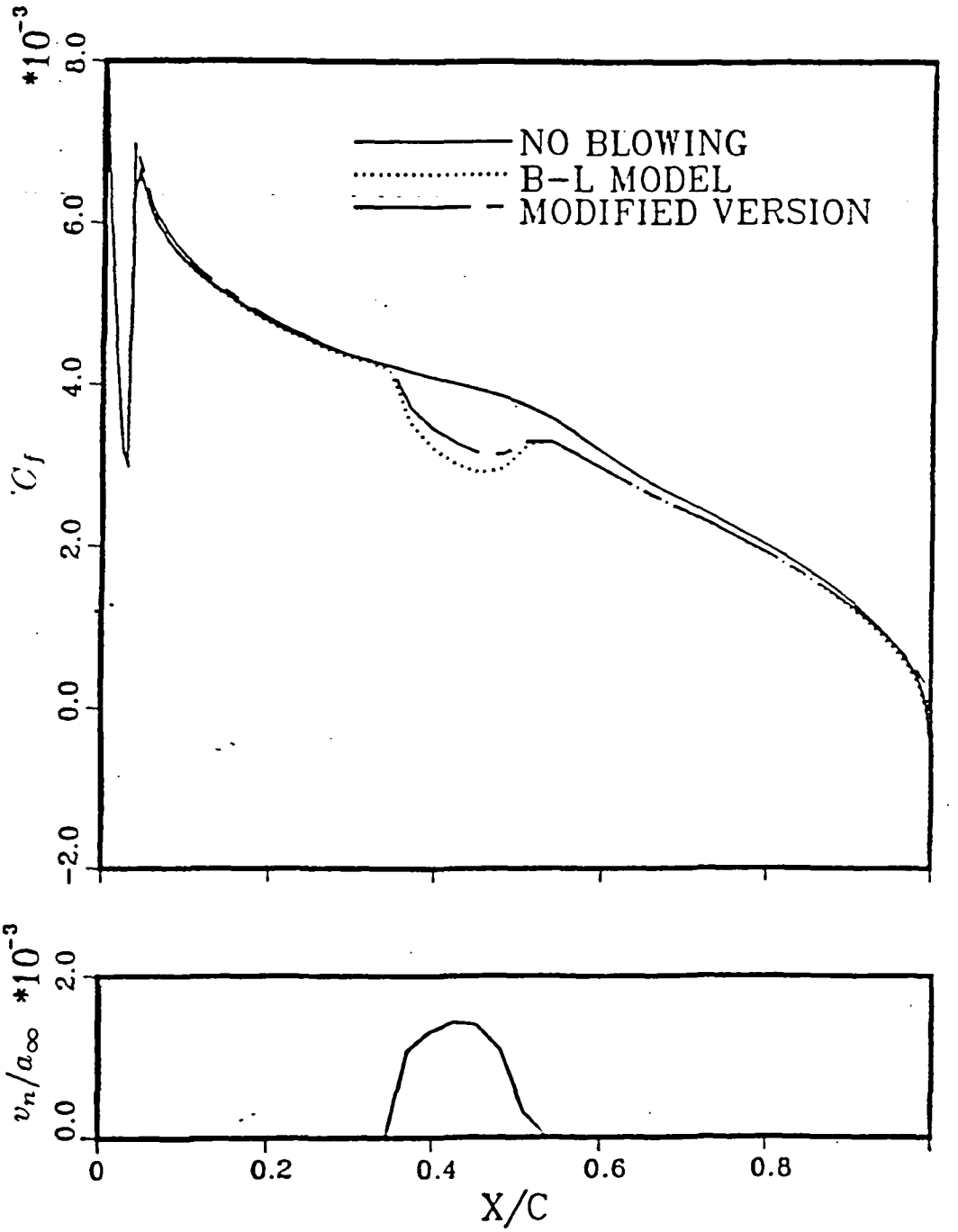

Fig. 4.3 Comparison of blowing effects on C_f by two turbulence models.

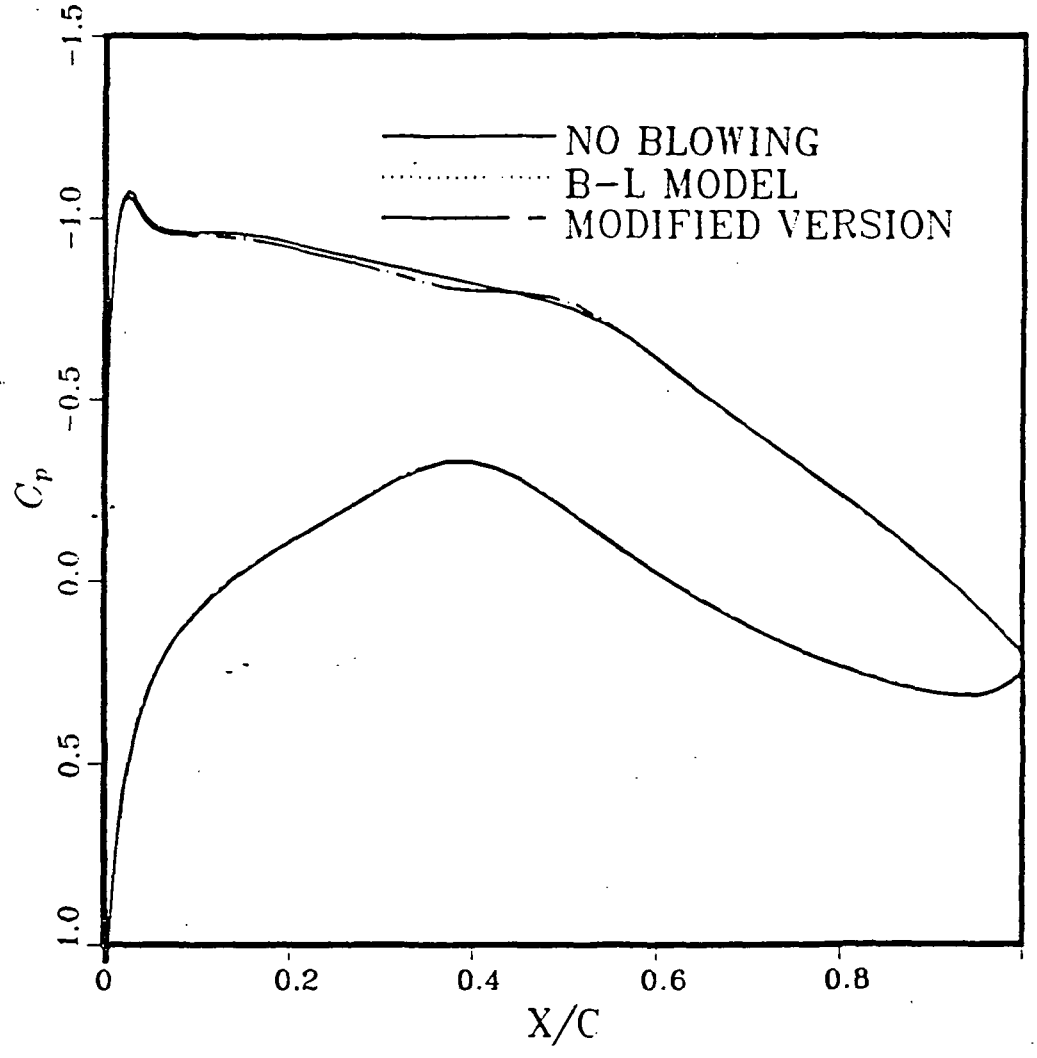

Fig. 4.4 Comparison of blowing effects on C_p by two turbulence models.

region is slightly lower in the modified version shown (see Fig. 4.5). That is because in the modified version the blowing increases the mixing rate (A^+ being reduced) and the suction tends to laminarize the flow (A^+ being increased). These effects are neglected when $A^+ = 26$ is assumed. Similarly, a strong adverse pressure gradient would reduce A^+ according to the modified version. The skin friction $C_f|_e$ for the RAE2822, at $M_\infty = 0.73$, $C_L = 0.803$, and $Re = 6.5 \times 10^6$ with transition specified at 0.03 chord, is shown in Fig. 4.6. Results from the two models are compared with Mehta's[42] computation and with experimental results[43] by Cook et al. All of the predictions agree well with experiment, but there is a slight improvement in results from the modified version.

Surface roughness also has a large effect upon A^+. But this effect is not considered in the present work.

Generally, the present IBL procedure is one to two orders of magnitude faster than the TLNS procedure. For a mildly separated transonic flow, it can provide very good results.[22-23] However, the range of allowable blowing rates in the IBL procedure is more restricted than in the TLNS approach. This restriction arises mainly from the boundary layer theory assumption that the magnitude of the normal velocity component v is less than $O(Re^{-1/2})$. In addition, the first-order boundary-layer approximation becomes suspect when a strong shock boundary-layer interaction occurs, because dp/dy in the boundary layer may not be negligible. At the expense of longer computing time, the TLNS procedure has less theoretical restrictions than the IBL procedure. Therefore, when a strong interaction occurs or blowing (or suction) becomes strong, the TLNS procedure is preferred in the present study.

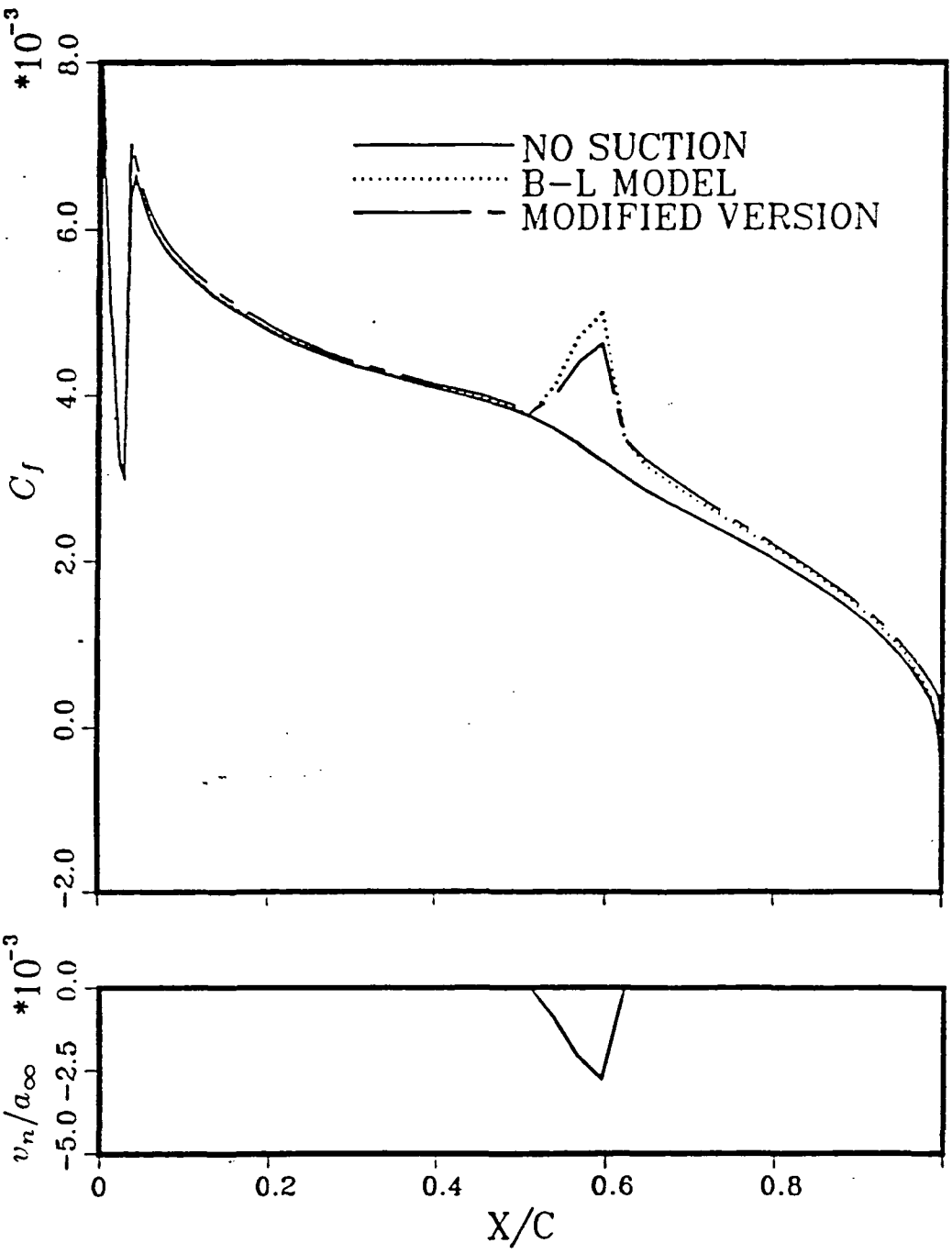

Fig. 4.5 Comparison of suction effects on C_f by two turbulence models.

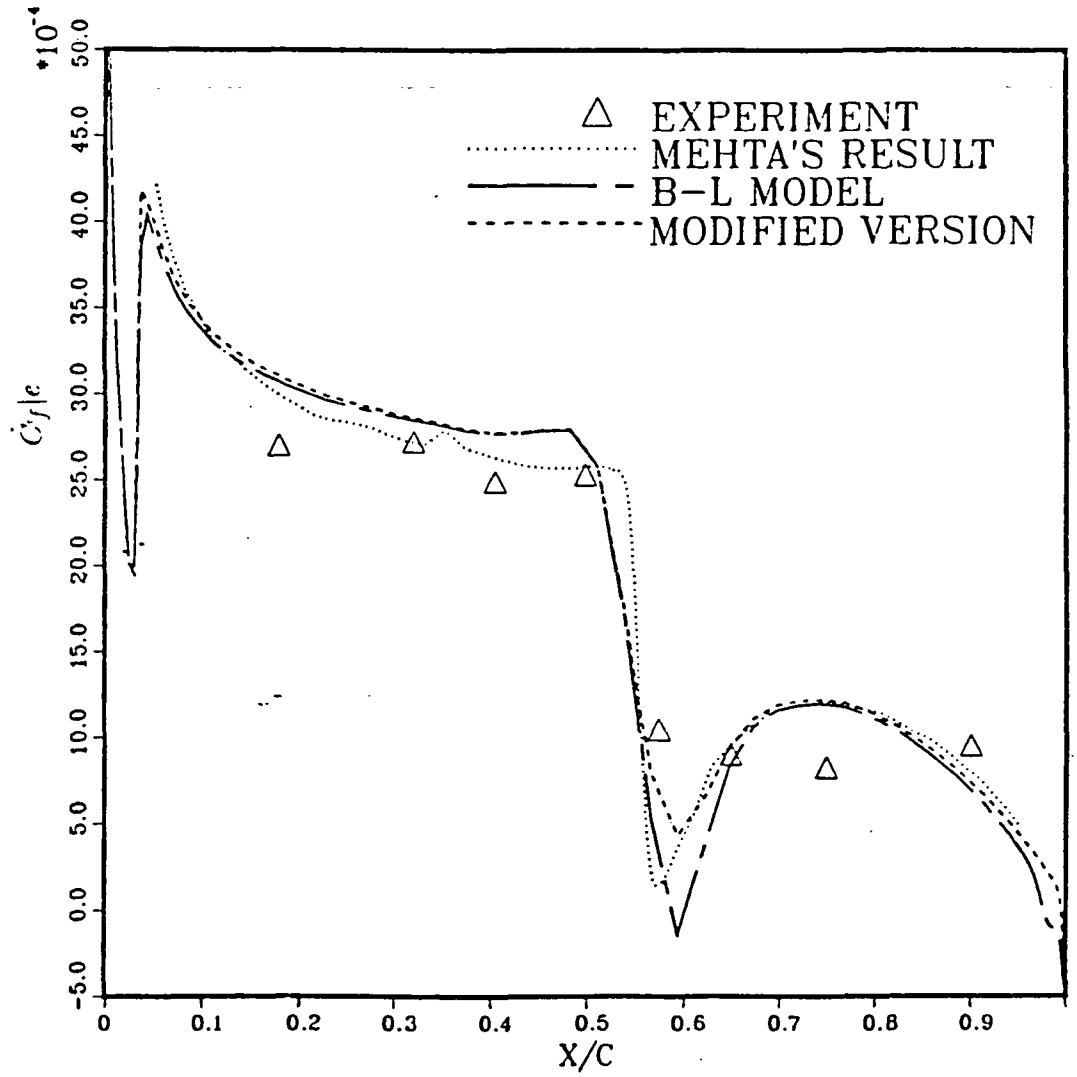

Fig. 4.6 Comparison of $C_f|e$ distributions for an RAE 2822 airfoil at $M_\infty = 0.73, Re = 6.5 \times 10^6$ and $C_L = 0.803$.

CHAPTER V

POROSITY AND CAVITY-FLOW MODELING

Since the holes over the porous region are very small and dense, it is difficult to compute the flow across the porous media without extremely fine grids. Therefore the porosity effect is modeled instead of being computed in the present study. The model proposed is patterned after the treatment of porous wind-tunnel walls[44] based on the Darcy's law.

Interface of Outer and Inner Flows

There are two porosity models used in this study. For both of them, the transpiration velocity v_n for the outer flow is governed by Darcy's law such that

$$v_n = -\frac{\bar{\sigma}}{\rho_\infty U_\infty}\left(p_{outer} - p_{inner}\right) \tag{5.1}$$

where the subscript n indicates the direction of the outward normal on the surface; p_{outer} and p_{inner} are the pressure above and below the porous surface, respectively; $\bar{\sigma}$ is the porosity distribution function which is determined by viscosity as well as by the size and density of the holes in the porous surface. The subscript *outer* indicates the outer-flow property and *inner* indicates the inner-flow property. The first cavity model considered assumes a constant pressure, $\bar{p}$, in the cavity, so that,

$$v_n = -\frac{\bar{\sigma}}{\rho_\infty U_\infty}(p_{outer} - \bar{p}_{inner}) \tag{5.2}$$

The constant cavity-pressure assumption was made for convenience but is expected to be qualitatively accurate. For passive flow through the cavity, the net mass flow through the porous surface of length S must be zero, or

$$Q = \int_S (\rho v_n)_{outer} ds = 0 \tag{5.3}$$

which leads to the relation,

$$\bar{p}_{inner} = \frac{\int_S \bar{\sigma}(\rho p)_{outer} ds}{\int_S \bar{\sigma}\rho_{outer} ds} \tag{5.4}$$

Once $\bar{p}_{inner}$ is known, the v_n for the outer flow can be determined from Eq. (5.2).

For the second model considered, the total pressure in the cavity is assumed to be constant, that is,

$$(p_t)_{inner} = constant \tag{5.5}$$

As before, total mass flow through the porous surface is conserved, and Darcy's law is applied across the interface,

$$v_n = -\frac{\bar{\sigma}}{\rho_\infty U_\infty}\left[p_{outer} - (\frac{p}{p_t})_{inner}(p_t)_{inner}\right] \tag{5.6}$$

which leads to the relation

$$(p_t)_{inner} = \frac{\int_S \bar{\sigma}(\rho p)_{outer} ds}{\int_S \bar{\sigma}\rho_{outer}(\frac{p}{p_t})_{inner} ds} \tag{5.7}$$

The pressure variation in the cavity $(p/p_t)_{inner}$ can be determined by computing the cavity flow. For convenience in coupling with the outer flow, the

flow in the cavity is assumed isentropic and irrotational with a different total pressure from the outer flow. The total temperature is assumed to be the same as that of the free stream. Therefore the cavity flow can be described by the stream-function formulation

$$\left(\frac{\Psi_x}{\rho}\right)_x + \left(\frac{\Psi_y}{\rho}\right)_y = 0 \tag{5.8a}$$

$$\rho = \left[1 - \frac{\gamma - 1}{\gamma + 1}\frac{(\Psi_x^2 + \Psi_y^2)}{\rho^2}\right]^{\frac{1}{\gamma - 1}} \tag{5.8b}$$

where

$$\rho u = \Psi_y \qquad \rho v = -\Psi_x \tag{5.8c}$$

The stream-function is set to zero at both the vertical side walls and the bottom wall of the cavity. Along the porous surface, it is determined by the integration of mass flow rate from the outer flow by

$$\Psi(x) = \int_{x_1}^{x} (\rho v_n)_{outer} ds \tag{5.9}$$

as indicated in Fig. 5.1.

The $(p/p_t)_{inner}$, $(p_t)_{inner}$ and v_n can be determined iteratively. The iterative process uses the first model to obtain an initial v_n, then integrates the mass flow rate by Eq. (5.9) to obtain the boundary conditions for the cavity and solves the cavity flow to update $(p/p_t)_{inner}$ underneath the porous surface. Then update the $(p_t)_{inner}$ by Eq. (5.7) and updates v_n by using Eq. (5.6) to finish the first iteration. Then iterative procedure is repeated to update the boundary stream function until the converged solutions ($(p_t)_{inner}$, $(p/p_t)_{inner}$, and v_n) are obtained. Then v_n is available for the next update of the outer flow solver.

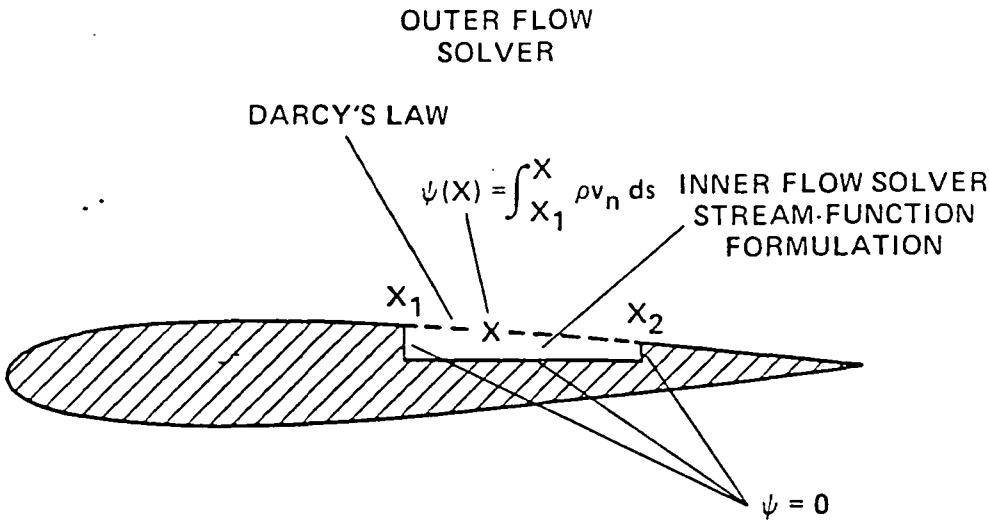

Fig. 5.1 Porous airfoil with a cavity-flow model.

The nonuniqueness of Neumann problem is avoided and boundary conditions are easily implemented by using the stream-function formulation (rather than full-potential equation with specified normal derivatives at all the boundary). The resulting model for the cavity flow, although not perfect, helps by providing estimates of how important pressure variations within the cavity might be.

Cavity-Flow Solver

The stream-function formulation in the cavity can be written in the ξ-η domain as

$$-\left(\frac{A_1}{J^2}V - \frac{A_2}{J^2}U\right)_\xi + \left(\frac{A_3}{J^2}U - \frac{A_2}{J^2}V\right)_\eta = 0 \tag{5.10a}$$

$$\rho = \left[1 - \frac{\gamma - 1}{\gamma + 1}q^2\right]^{\frac{1}{\gamma - 1}} \tag{5.10b}$$

where

$$U = \frac{J}{\rho}\Psi_\eta \qquad V = -\frac{J}{\rho}\Psi_\xi \tag{5.10c}$$

$$q^2 = \frac{A_3}{\rho^2}{\psi_\eta}^2 + 2\frac{A_2}{\rho^2}\Psi_\eta\Psi_\xi + \frac{A_1}{\rho^2}{\Psi_\xi}^2 \tag{5.10d}$$

in which the nondimensionalization and the definitions of A_1, A_2, A_3 and J have been described earlier in the inviscid full-potential solver. However, it should be noted that the stagnation density used for nondimensionalization is different from the outer-flow stagnation density.

An approximate factorized scheme (AF1), which is a reformulation of an ADI scheme, is applied to solve the cavity flow. An ADI for potential

equation can be easily to be converted to solve the stream-function equation. The only difference is that the density is moved from numerator to denominator(see Eqs. (2.1a) and (5.8a)). Consequently, there is no difficulty in obtaining a converged solution for the subsonic flow in the cavity. The numerical procedure is

$$(\alpha - \overrightarrow{\delta_\eta} A_j \overleftarrow{\delta_\eta})(\alpha - \overrightarrow{\delta_\xi} A_i \overleftarrow{\delta_\xi}) C^n_{i,j} = \alpha\omega L\Psi^n_{i,j} \tag{5.11}$$

where $C^n_{i,j} = \Psi^{n+1}_{i,j} - \Psi^n_{i,j}$, $\alpha \sim 1/\delta t$, and ω is a relaxation parameter. $\overrightarrow{\delta_\eta}()_{i,j}$ and $\overrightarrow{\delta_\xi}()_{i,j}$ are the first-order forward-difference operators defined by

$$\overrightarrow{\delta_\eta}()_{i,j} = ()_{i,j+1} - ()_{i,j} \tag{5.12a}$$

$$\overrightarrow{\delta_\xi}()_{i,j} = ()_{i+1,j} - ()_{i,j} \tag{5.12b}$$

and $\overleftarrow{\delta_\eta}()_{i,j}$ and $\overleftarrow{\delta_\xi}()_{i,j}$ are the first-order backward-difference operators defined by

$$\overleftarrow{\delta_\eta}()_{i,j} = ()_{i,j} - ()_{i,j-1} \tag{5.13a}$$

$$\overleftarrow{\delta_\xi}()_{i,j} = ()_{i,j} - ()_{i-1,j} \tag{5.13b}$$

Eq. (5.11) can be derived by applying the Crank-Nicolson scheme to the two-dimensional heat equation. A_i and A_j are defined by

$$A_i = \left(\frac{A_1}{\rho J}\right)_{i-\frac{1}{2},j} \qquad A_j = \left(\frac{A_3}{\rho J}\right)_{i,j-\frac{1}{2}} \tag{5.14}$$

where ρ is updated using Eq. (5.10b). The residual $L\Psi^n_{i,j}$ is obtained from

$$L\Psi^n_{i,j} = \overleftarrow{\delta_\xi}\left(\frac{A_1\Psi_\xi + A_2\Psi_\eta}{J\rho}\right)_{i+\frac{1}{2},j} + \overleftarrow{\delta_\eta}\left(\frac{A_2\Psi_\xi + A_3\Psi_\eta}{J\rho}\right)_{i,j+\frac{1}{2}} \tag{5.15}$$

Values of the density computed from Eq. (5.10b) are stored at cell centers, that is, at $(i+\frac{1}{2}, j+\frac{1}{2})$, using values of Ψ_ξ and Ψ_η computed from

$$(\Psi_\xi)_{i+\frac{1}{2},J+\frac{1}{2}} = \frac{1}{2}(\Psi_{i+1,J+1} - \Psi_{i,J+1} + \Psi_{i+1,j} - \Psi_{i,j}) \tag{5.16}$$

$$(\Psi_\eta)_{i+\frac{1}{2},J+\frac{1}{2}} = \frac{1}{2}(\Psi_{i+1,J+1} - \Psi_{i+1,J} + \Psi_{i,j+1} - \Psi_{i,j}) \qquad (5.17)$$

Values of the density required at $(i+\frac{1}{2}, j)$ or $(i, j+\frac{1}{2})$ are obtained using simple averages. The ADI scheme is implemented in a two-step format:

$$(\alpha - \overrightarrow{\delta_\eta} A_j \overleftarrow{\delta_\eta}) f^n_{i,j} = \alpha\omega L\Psi^n_{i,j} \qquad (5.18a)$$

where $\omega \approx 2.$ and

$$(\alpha - \overrightarrow{\delta_\xi} A_i \overleftarrow{\delta_\xi}) C^n_{i,j} = f^n_{i,j} \qquad (5.18b)$$

A scalar tridiagonal matrix is inverted at each step using the Thomas algorithm. A repeating sequence of $\alpha's$ (that is, variable time step) is used to speed up the convergence. A suitable sequence of $\alpha's$ proposed by Ballhaus et al.[45] is used

$$\alpha_k = \alpha_H(\alpha_L/\alpha_H)^{(k-1)/(M-1)} \qquad k = 1, 2, 3, ..., M$$

where M is the number of elements in the sequence. for which either 6 or 8 is used in the present study. Both α_H and α_L are optimized by numerical experimentation.

Grid Generation

The grids for the cavity flow is generated by an algebraic method. A linear function is chosen as follows,

$$x(\xi,\eta) = x_t(\xi)\frac{\eta - 1}{\eta_{max} - 1} + x_b(\xi)\frac{\eta_{max} - \eta}{\eta_{max} - 1} \qquad (5.19a)$$

$$y(\xi,\eta) = y_t(\xi)\frac{\eta - 1}{\eta_{max} - 1} + y_b(\xi)\frac{\eta_{max} - \eta}{\eta_{max} - 1} \qquad (5.19b)$$

where subscript t or b indicates the top or bottom wall of the cavity. The values of x_t and y_t are obtained by locally refining the outer-flow coordinates on the porous surface, and the values of x_b and y_b are determined by the shape of the cavity.

CHAPTER VI

NUMERICAL RESULTS AND DISCUSSION

Inviscid Flow Solutions

The inviscid flow solutions shown in this chapter are obtained from the procedure descibed in Chapter II without the entropy correction. A 14% thick NASA supercritical airfoil[6] and a NACA 0012 airfoil were used in a series of numerical studies of the effect of a porous surface on transonic performance with the first model. All of the computations by the inviscid-flow approach were performed on a 223 x 31 C-type mesh, with 162 of the 6913 grid points on the airfoil surface.

Three types of porosity distribution have been examined which were obtained by varying the porosity distribution function $\bar{\sigma}$ in Eq. (5.1). They are described as follows:

Type 1

$$\bar{\sigma} = constant$$

Type 2

$$\bar{\sigma} = \bar{\sigma}_{max} \sqrt{\sin \frac{x - x_1}{x_2 - x_1} \pi}$$

where x_1 and x_2 are the limits of the porous region shown in Fig. 1.1, and $\bar{\sigma}_{max}$ is the maximum porosity at the midpoint of the region. The Type 2 porosity distribution is the distribution used by Savu and Trifu.[8]

Type 3

$$\bar{\sigma} = \bar{\sigma}_{max} \sqrt{\cos \frac{x - x_s}{x_k - x_s} \frac{\pi}{2}}$$

where x_s is the horizontal position of the shock if the porous surface were solid, and x_k represents either x_1 or x_2 depending on whether x is less or greater than x_s. This function automatically adjusts the porosity distribution so that it decreases from the maximum value under the shock wave to zero at either end of the porous region.

The performance of a 14% thick NASA supercritical airfoil with a porous surface has been experimentally investigated.[5-7] However, as mentioned earlier, this airfoil was mounted so that only the upper half of the airfoil was exposed to the transonic flow. This experimental arrangement was modeled by reflecting the upper surface to the lower surface and computing the flow about the resulting symmetrical airfoil at zero angle of attack. There is some uncertainty concerning the airfoil coordinates in the region near the trailing edge where the y-coordinates of the airfoil's upper surface are negative. In the numerical simulation, these coordinates are modified by using a linear interpolation from (x, y) = (0.95, 0.0057) to the trailing edge at (1.0, 0.0).

To agree with the experimental shock-location,[7] the computations had to be performed at free-stream Mach numbers slightly lower than those measured. This is probably caused by the differences between the experimental and numerical geometries including the lack of wind tunnel wall modeling in the computed results and the inviscid assumption. For example, the flow over the solid supercritical airfoil at M_∞ = 0.81 in the wind tunnel can be approximated by using M_∞ = 0.795 in the computation (Fig. 6.1). Also the flow over the same airfoil at M_∞ = 0.85 can be approximated by using M_∞ = 0.805 (Fig. 6.2). Type 1 porosity with $\bar{\sigma}_{max}$= 0.6 was used to model the experimental uniform 2.8% porosity (based on the hole area divided by the

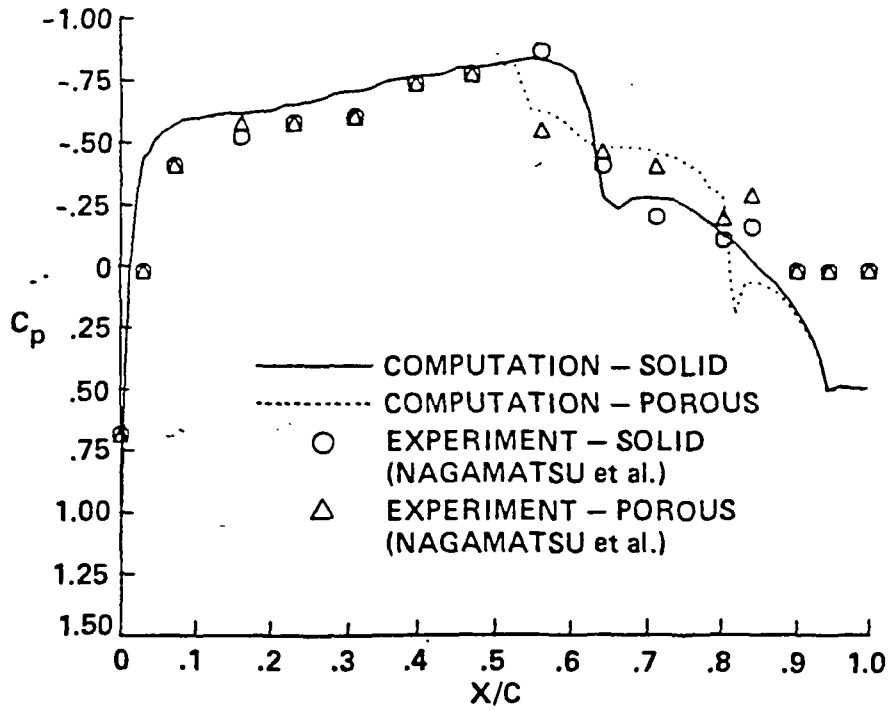

Fig. 6.1 Comparison of computed and experimental pressure distribution on the surface of the modified NASA supercritical airfoil. Experimental data at $M_\infty = 0.81$ and 2.8% porosity; computations at $M_\infty = 0.795$ with $\bar{\sigma} = 0.6$ Type 1 porosity.

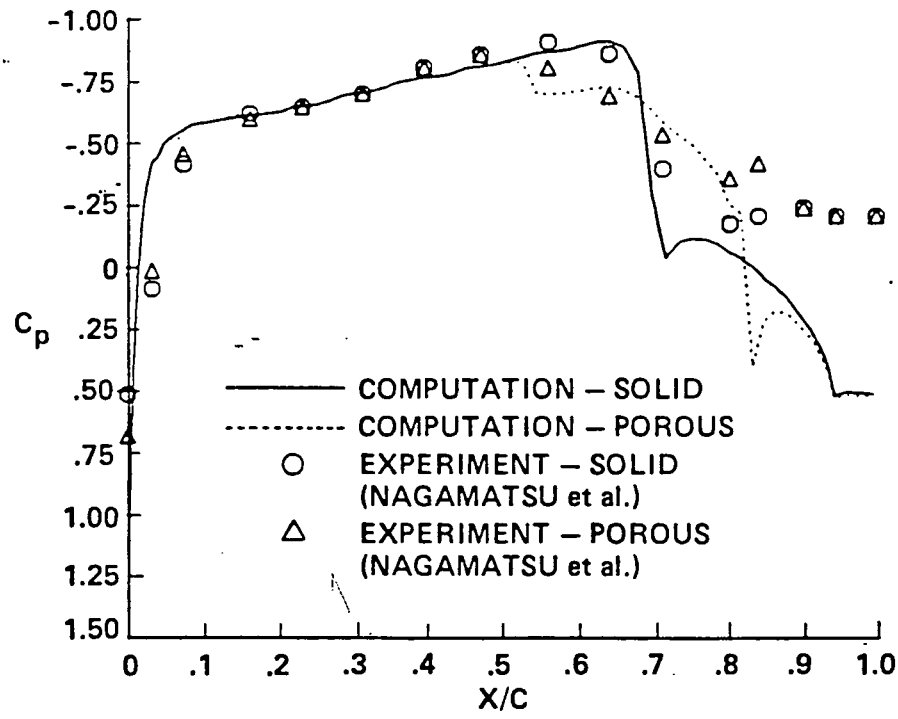

Fig. 6.2 Comparison of computed and experimental pressure distribution on the surface of the modified NASA supercritical airfoil. Experimental data at $M_\infty = 0.85$ and 2.8% porosity; computations at $M_\infty = 0.805$ with $\bar{\sigma} = 0.6$ Type 1 porosity.

total airfoil area).[3] The porous region extends from 56% to 83% in both the experiment and computations. The computed and experimental pressure distributions on the porous airfoil are compared in Figs. 6.1-6.2. Overall, the agreement is quite good. The discrepancy in the trailing edge region is due, at least in part, to the difference in geometries and viscous effects. These results suggest that $\bar{\sigma}_{max}$= 0.6 may be used to simulate this flow over a range of Mach numbers and also indicate that the assumption of constant-cavity pressure results in reasonable pressure distribution predictions.

- The variation in the pressure distribution with $\bar{\sigma}$ is shown in Fig. 6.3. As $\bar{\sigma}$ is increased, the variation in the pressure distribution becomes smaller. For example, as $\bar{\sigma}$ is increased from 0.6 to 0.8, there is very little change in the pressure distribution. In other words, increasing the porosity beyond $\bar{\sigma} \approx 0.6$ does not significantly change the flow or improve the performance.

It is difficult to make a direct comparison of the computed wave drag with the experimental drag presented in Ref. [7]. The measured drag data contain the effects of viscosity, airfoil surface roughness, and other factors that have not been considered in our analysis. For approximate comparison, the viscous drag was estimated by computing the viscous flow over the solid airfoil at a nominal M_∞= 0.6 using the viscous/inviscid interaction code of Refs. [22-23]. This $C_D|_{viscous}$= 0.012 was then added to the wave drag computed with the present code, and the results are compared with the experimental data in Fig. 6.4. The drag reduction effect caused by the porous surface observed in the laboratory is qualitatively obtained in the present study. However, the drag reduction occurs at lower M_∞ than in the experiment. In addition, the increased drag at lower M_∞ in the experiment is not predicted.

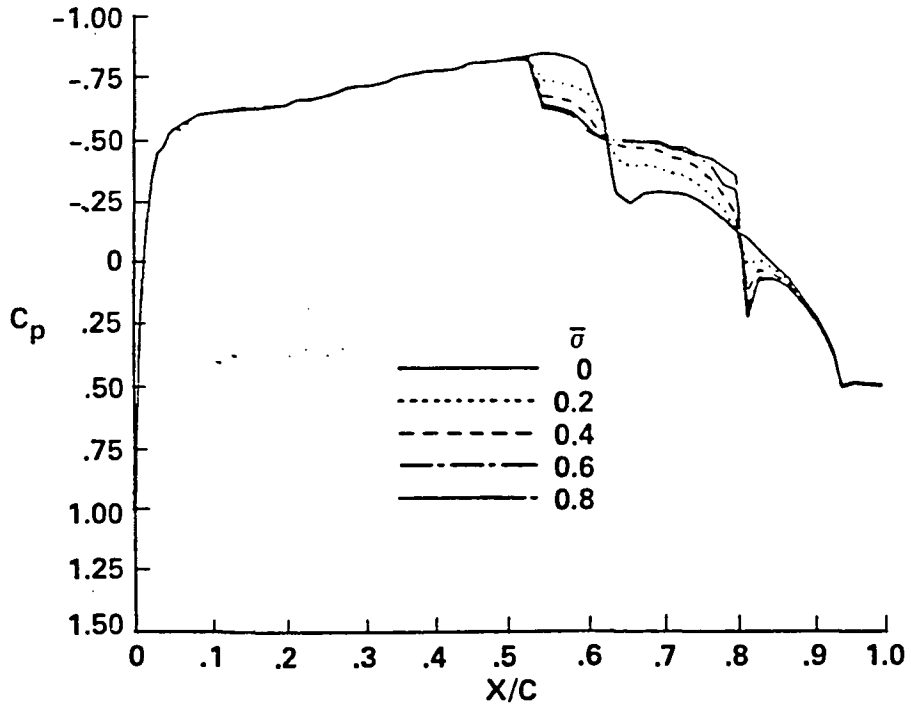

Fig. 6.3 Effects of varying the porosity strength $\bar{\sigma}$ on the pressure distribution of a modified NASA supercritical airfoil at $\alpha = 0°$ and $M_\infty = 0.795$.

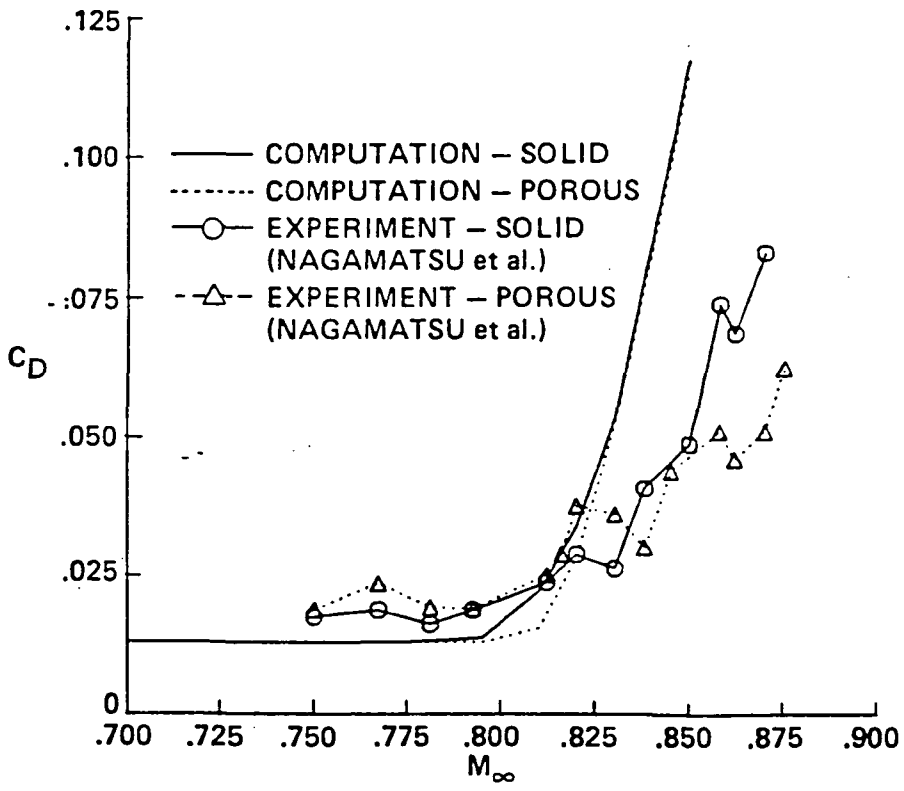

Fig. 6.4 Computed and experimental drag on a modified NASA supercritical airfoil at $\alpha = 0°$.

The effect of a porous surface on the $M_\infty = 0.8$ flow past the NACA 0012 airfoil at zero angle of attack is presented in Figs. 6.5 and 6.6. A Type 2 porosity is used on the upper surface between $x = 0.4$ and $x = 0.8$ with $\bar{\sigma}_{max}$= 0.6. The constant-Mach number contours show a normal shock standing below the solid lower surface of the porous airfoil whose location and strength are not much different from those of the shock on the original solid airfoil. However, the shock above the upper surface is weakened in the presence of the porous surface, as shown by a group of less concentrated constant-Mach lines around the sonic line. Figure 6.5 also reveals that the porous surface causes a weak, oblique compression wave at its upstream end ($x = 0.4$), due to the blowing from the cavity, and a readjusted compression downstream of the shock due to the suction of air into the cavity. The contour lines in the shock region are no longer normal to the airfoil surface, resulting in a lambda-shaped shock wave structure similar to that photographed in the laboratory (Refs. [5-7]).

The pressure distribution on the upper airfoil surface for the case just presented is plotted in Fig. 6.6. The results for a porous airfoil (dashed line) and solid airfoil(solid line) are compared. The comparison clearly shows that the original steep compression through the normal shock on the solid airfoil has been reduced in the presence of the porous region. The original shock is replaced by several weaker compressions over the region covered by the porous surface. The resulting weaker, adverse-pressure gradient would lessen the possibility of flow separation. The porous upper surface has a negligible influence on the pressure distribution along the lower surface; that distribution is, therefore, omitted here. The asymmetrical pressure distribution on the upper and lower surfaces causes a small lift on the airfoil at zero angle of attack, with $C_L = 0.0183$. On the other hand, a 27.5% decrease in wave drag

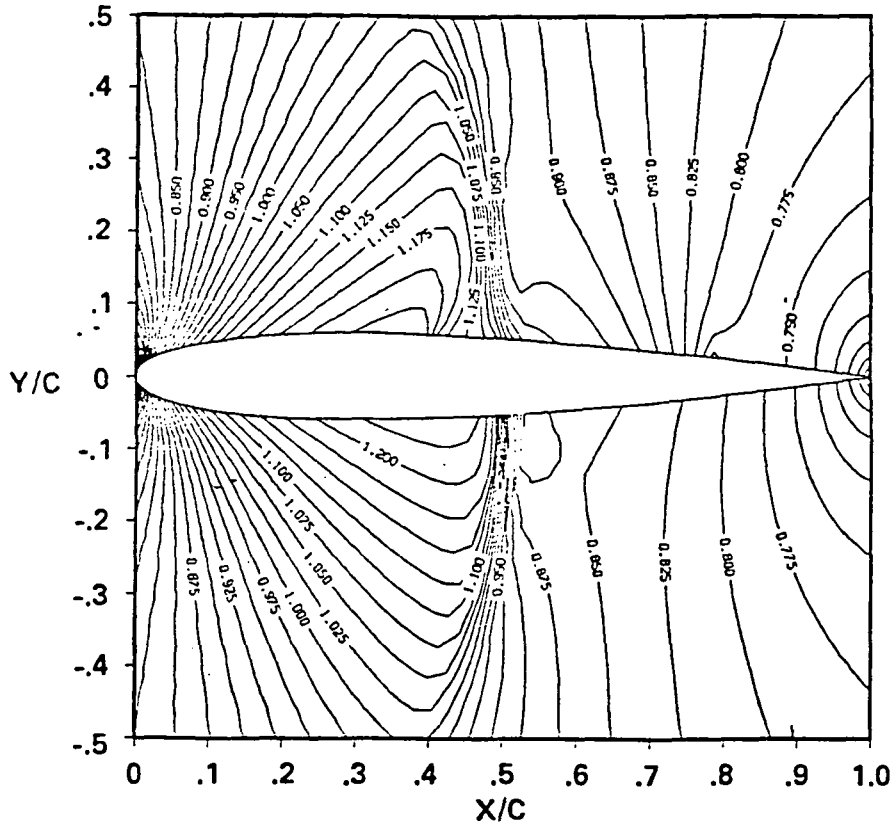

Fig. 6.5 Constant Mach number contours around a porous NACA 0012 airfoil, $M_\infty = 0.8$, $\alpha = 0°$, Type 2 porosity, $\bar{\sigma}_{max} = 0.6$, $x_1 = 0.4$, $x_2 = 0.8$ (upper surface is porous).

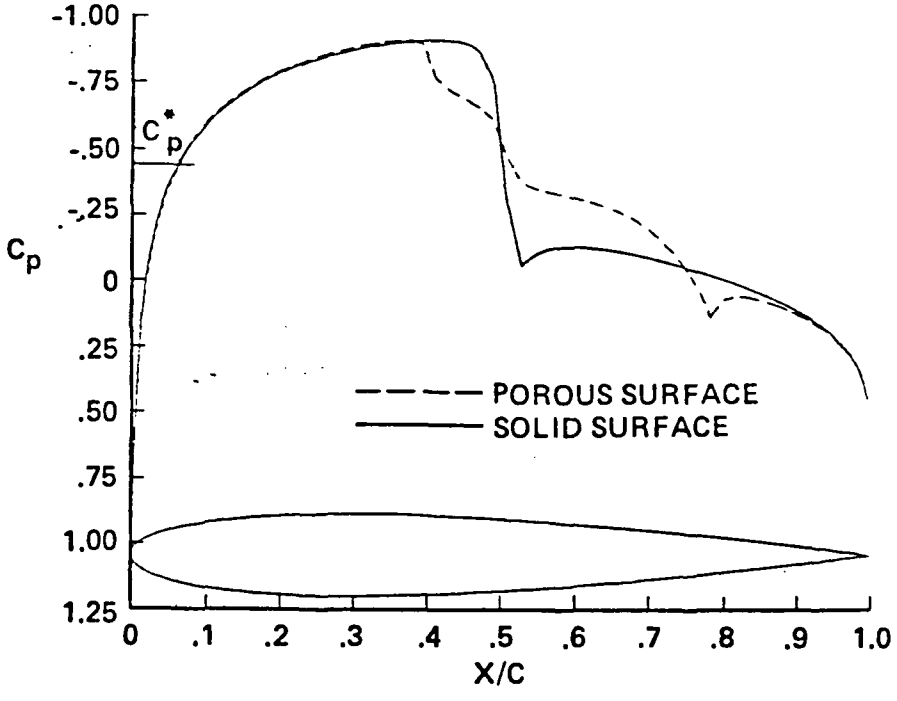

Fig. 6.6 Pressure distribution on the upper surface of the airfoil described in Fig. 6.5.

from $C_D = 0.0069$ to 0.0050 is found for the porous airfoil.

Much larger decreases in drag are obtained when both upper and lower surfaces are made porous. The effect of varying the porosity strength on the drag of a double-porous NACA 0012 airfoil at $\alpha = 0°$ is shown in Fig. 6.7. A Type 2 porosity distribution between $x = 0.1$ and $x = 1.0$ is used for all curves presented. The porous surface has a drag-reduction effect only when a shock appears above it at Mach numbers higher than 0.77, and that effect is enhanced by increasing $\bar{\sigma}_{max}$ (i.e., by using porous surfaces having smaller resistance to the penetrating flow). However, this trend diminishes as $\bar{\sigma}_{max}$ reaches higher values. This is consistent with the result shown in Fig. 6.3.

Changing from Type 2 to Type 3 porosity does not cause a significant change in drag if the normal shock appears near the center of the porous surface. This change assumes the same value of $\bar{\sigma}_{max}$ for both porosity distributions. If the shock wave is not centered in the porous region, Type 3 porosity is considerably better than Type 2 in smearing the shock and reducing the wave drag.

The behavior of porous airfoils at a finite angle of attack is now described. The Mach number contours for a solid NACA 0012 airfoil at Mach 0.75 and an angle of attack of 1° are plotted in Fig. 6.8. A shock wave appears only on the upper surface. A Type 3 porosity of strength $\bar{\sigma}_{max} = 0.3$ is then distributed on 90% of the upper surface between $x = 0.1$ and $x = 1.0$. The resulting flow pattern and pressure distribution, plotted in Figs. 6.9 and 6.10, respectively, reveal that this widely distributed porosity is very effective in reducing the shock strength. By making the upper surface porous, C_L is increased from 0.240 to 0.357 while C_D is decreased from 0.0240 to 0.0008,

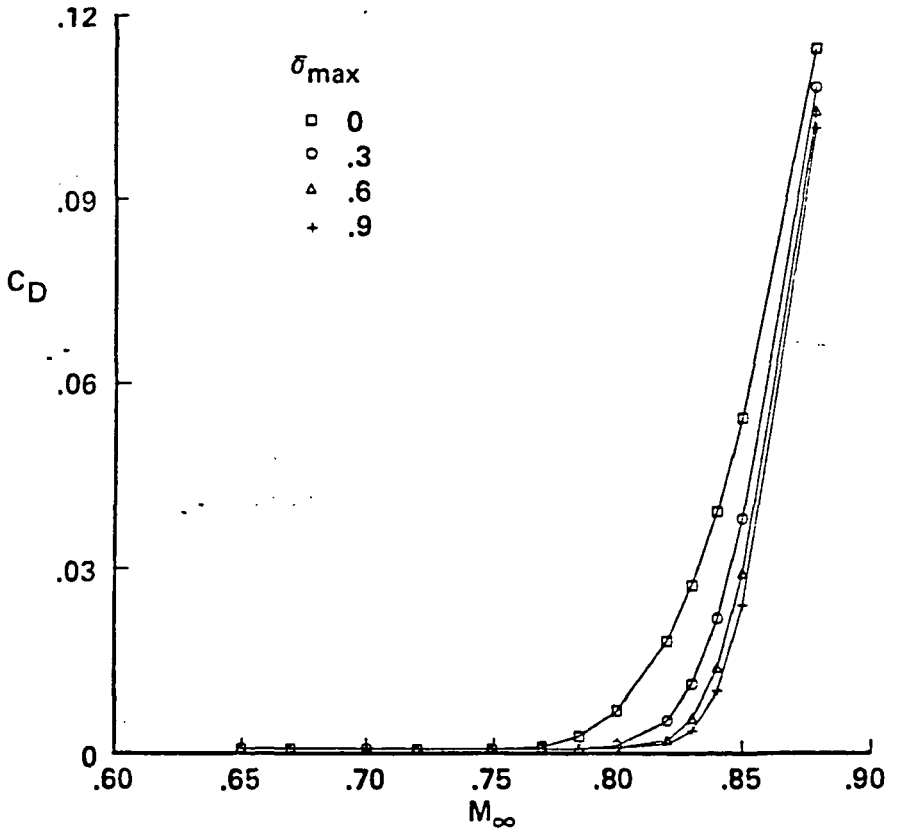

Fig. 6.7 Effect of varying porosity strength on the drag of a NACA 0012 airfoil at $\alpha = 0°$, Type 2 porosity, $x_1 = 0.1$, $x_2 = 1.0$ (both the upper and lower surfaces are porous).

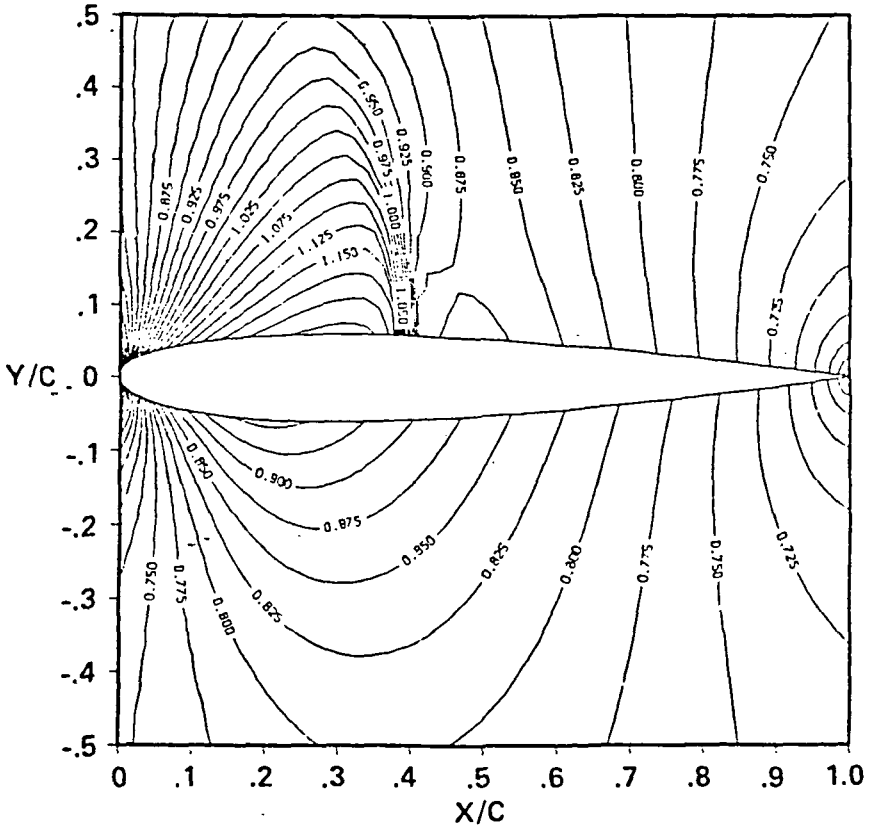

Fig. 6.8 Constant Mach number contours around a solid NACA 0012 airfoil for $M_\infty = 0.75$ and $\alpha = 1°$.

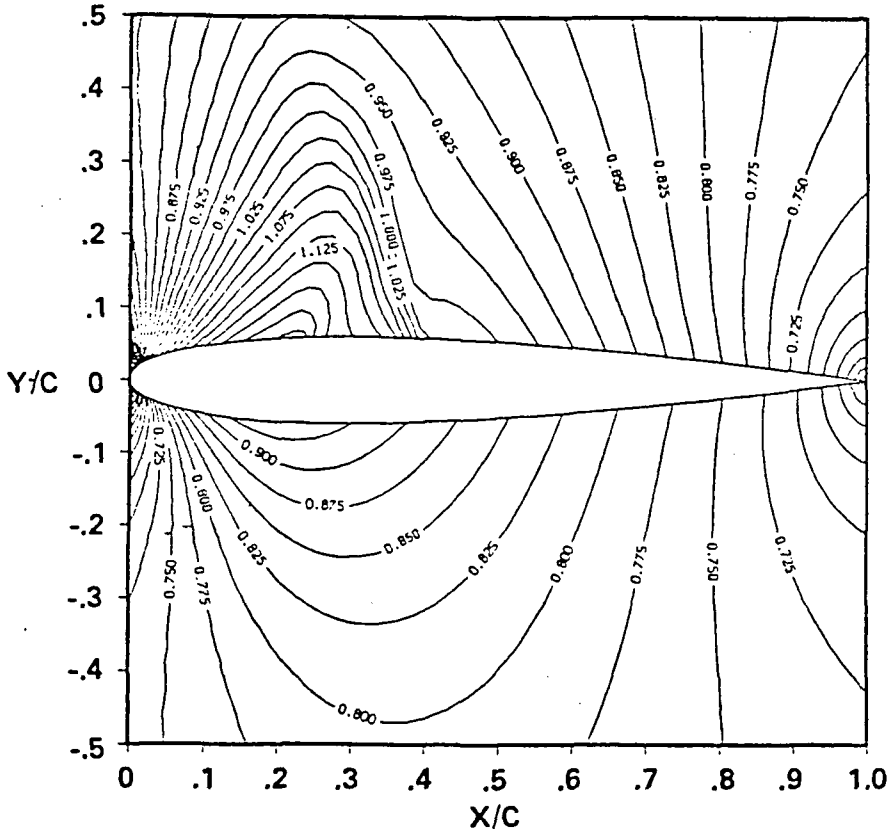

Fig. 6.9 Constant Mach number contours around a porous NACA 0012 airfoil, $M_\infty = 0.75$, $\alpha = 1°$, Type 3 porosity, $\bar{\sigma}_{max} = 0.3$, $x_1 = 0.1, x_2 = 1.0$ (upper surface is porous).

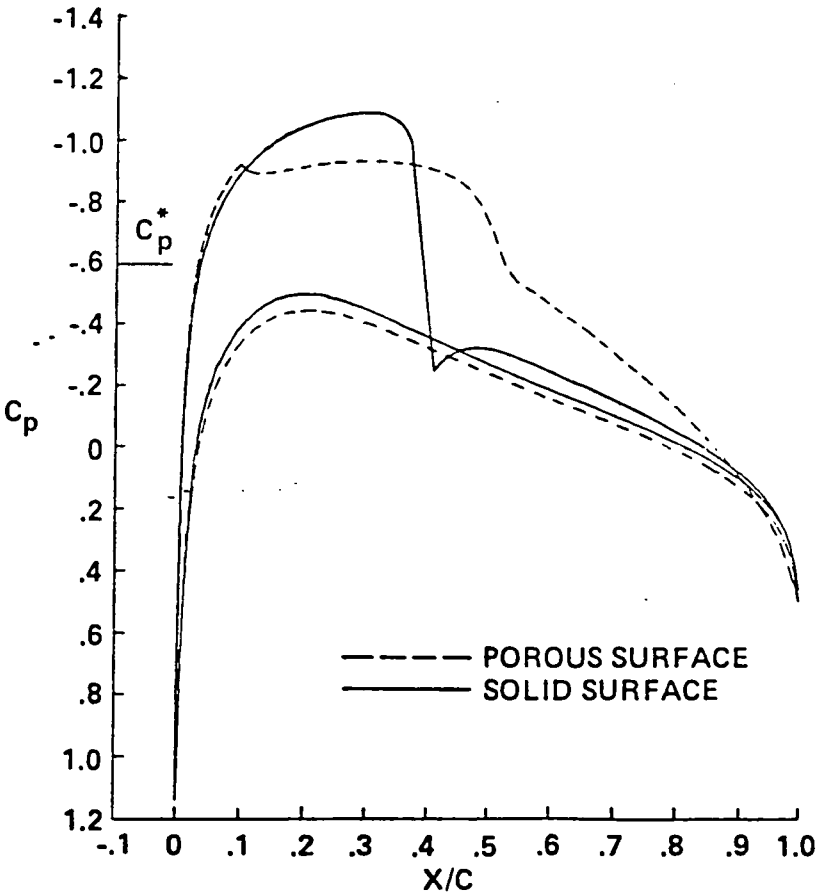

Fig. 6.10 Pressure distribution around the airfoil described in Fig. 6.8 and 6.9.

which corresponds to a nearly shock-free condition.

To study the effect of varying porosity strength on lift and drag of a transonic airfoil, a Type 3 porosity is distributed between $x = 0.3$ and $x = 0.9$ over the upper surface of a NACA 0012 airfoil. For this series of cases the angle of attack is fixed at 1°. The result for drag plotted in Fig. 6.11 is analogous to that shown in Fig. 6.7 for the double-porous airfoil at zero angle of attack, showing that large wave-drag reductions can be achieved by increasing the porosity. Plotted in Fig. 6.12 are the lift coefficient data which indicate that lift is increased by making the upper surface porous. Unlike the drag coefficient, C_L is affected by the porous surface at Mach numbers less than 0.72 when the shock is still upstream of the porous region. The higher lift is caused by asymmetric changes in the pressure on the porous-upper and solid-lower surfaces of the airfoil. A dramatically increased lift of a porous airfoil was also observed by Savu et al. using the inviscid small-disturbance approximation (Ref. [8]). Relatively, results from an IBL approach by Olling[18] were more conservative (lift was increased about 2%). Indeed, the lift was improved little for a porous airfoil at lower M_∞ and α, as has been indicated experimentally by Krogmann et al. (Ref. [9]).

According to the present inviscid-flow approach (although the results may be slightly over-optimistic and somewhat at variance with the experimental results), it can be concluded that the shock strength can be weakened, wave drag can be reduced and lift may be increased by appropriate porosity distribution. In addition, the inviscid-flow approach can provide an upper bound of useful levels of $\bar{\sigma}$ of interest for viscous flow calculations.

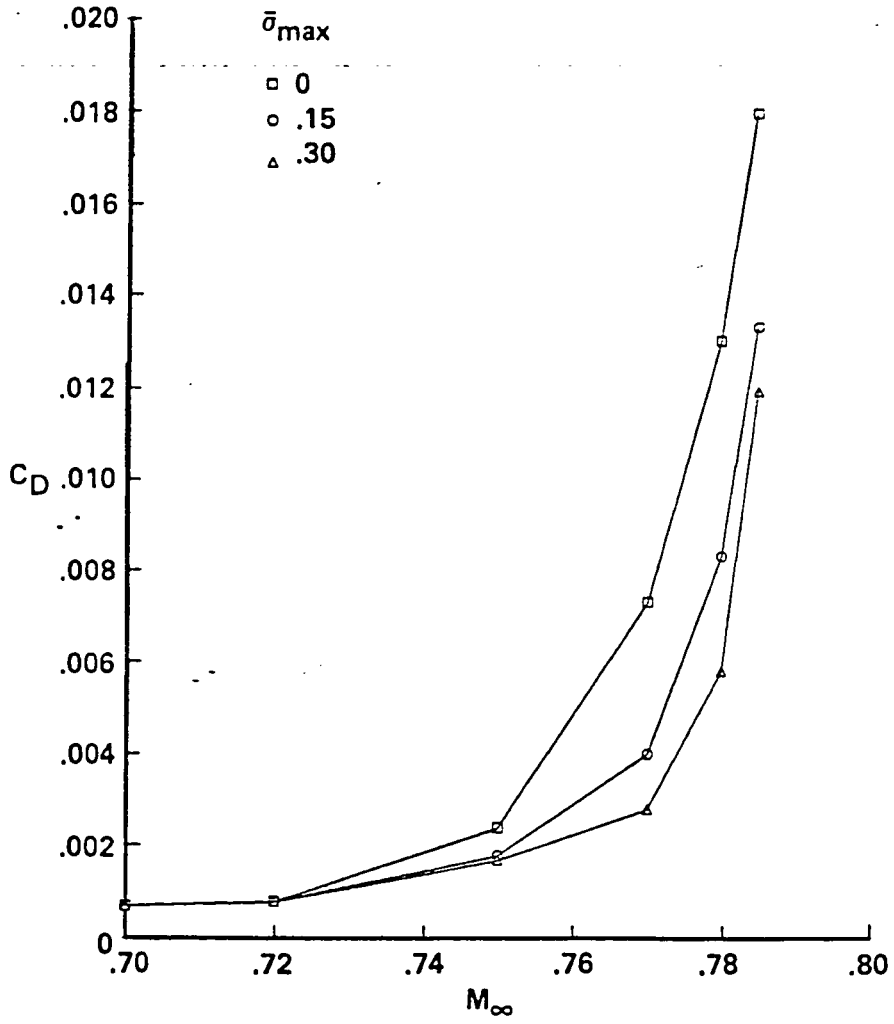

Fig. 6.11 Effect of varying porosity strength on the drag of a NACA 0012 airfoil at $\alpha = 1°$, Type 3 porosity, $x_1 = 0.3$, $x_2 = 0.9$ (upper surface is porous).

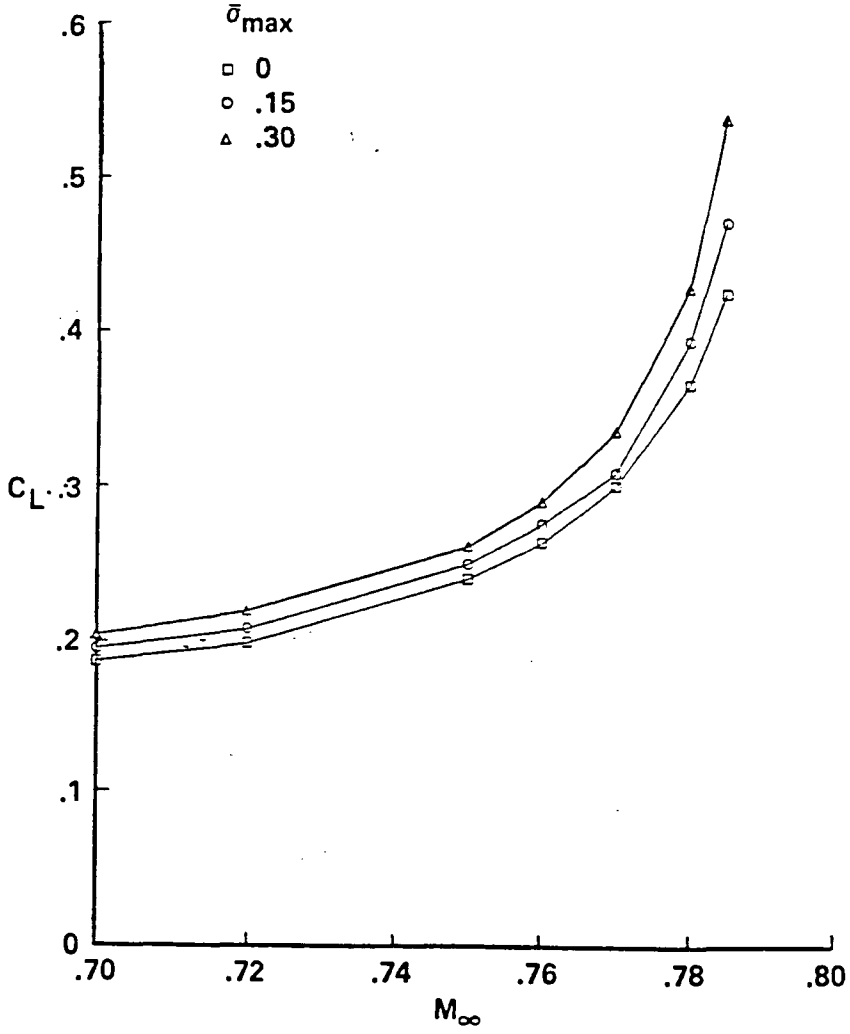

Fig. 6.12 Effect of varying porosity strength on the lift of a NACA 0012 airfoil at $\alpha = 1°$, Type 3 porosity, $x_1 = 0.3$, $x_2 = 0.9$ (upper surface is porous).

Viscous Flow Solution

It is well known that viscous effects are important on airfoil performance, especially at transonic speeds. When a shock/boundary layer interaction becomes strong, the inviscid-flow analysis alone is not sufficient to describe the flow about an airfoil. There are numerous examples illustrating the discrepancies in shock position and pressure at the trailing edge predicted by inviscid-flow calculations in Ref. [46]. In the present inviscid-flow approach, such discrepancies were noted in the previous section particularly for a solid airfoil. In addition, the blowing and suction at the airfoil surface have such a large influence on the boundary layer that v_w affects the inviscid flow not only directly but also indirectly via the effect of δ^* on the $\bar{v}_n$ (see Eq. (3.7)). The purpose of the work here is to study these viscous effects in transonic flow past porous airfoils. In the IBL procedure, the inviscid grid is the same as that mentioned earlier in this chapter, with an additional 50 grid lines in the η direction for the boundary layer algorithm. In the TLNS procedure, on the other hand, the computations were performed on a 251 x 65 C-type mesh, with 163 points on the airfoil surface.

Effects of Active Blowing and Suction

Since the porous airfoil induces blowing in the supersonic region and suction in the subsonic region, it is meaningful to investigate separately effects of blowing and suction on the shock and boundary-layer control. The first test case is a NACA 0012 airfoil, at $M_\infty = 0.75$, with $\alpha = 2.0°$, the transition specified at 0.03 chord, and $Re = 3.76 \times 10^6$. Generally, the numerical results show that blowing in the supersonic region weakens the shock strength and smoothes the pressure gradient. However, if the blowing is too

strong, the results indicate that separation may occur in the blowing region and increase the thickness of the boundary layer approaching the trailing edge, which causes not only an increase in viscous pressure drag but also a decambering effect of the boundary layer leading to a decrease in lift. For the case of blowing ahead of the shock such as the one shown in Fig. 6.13, the results indicate that the pressure gradient is smoothed, C_D (pump drag being excluded) is reduced from 0.01913 to 0.01707, and C_L is also reduced from 0.37528 to 0.30588. Even though the blowing velocity in this case is less than 1.5% of the free-stream velocity, C_f already becomes negative in the blowing region. In other words, the drag reduction with normal blowing seems to be mainly due to the weakened shock rather than due to the boundary-layer control achieved by increasing the mixing rate. On the other hand, suction behind the shock generally increases the shock strength, moves the shock downstream and delays separation. Shown in Fig. 6.14 is an example of these phenomena. In this case C_L is increased from 0.37528 to 0.44354, but C_L/C_D is improved only slightly because wave drag and skin-friction drag are also increased. Furthermore, the viscous pressure drag is not a dominant part of the total drag in this case, so the form drag cannot be reduced significantly. The boundary-layer control aspect is shown by the fact that C_f is increased not only in the suction area but also in the region downstream of the suction, indicating that suction probably can sustain the strong shock without separation or with controllable separation. Therefore, in regard to drag reduction, the above numerical results imply that the shock can be weakened by normal blowing and boundary-layer control can be achieved by suction.

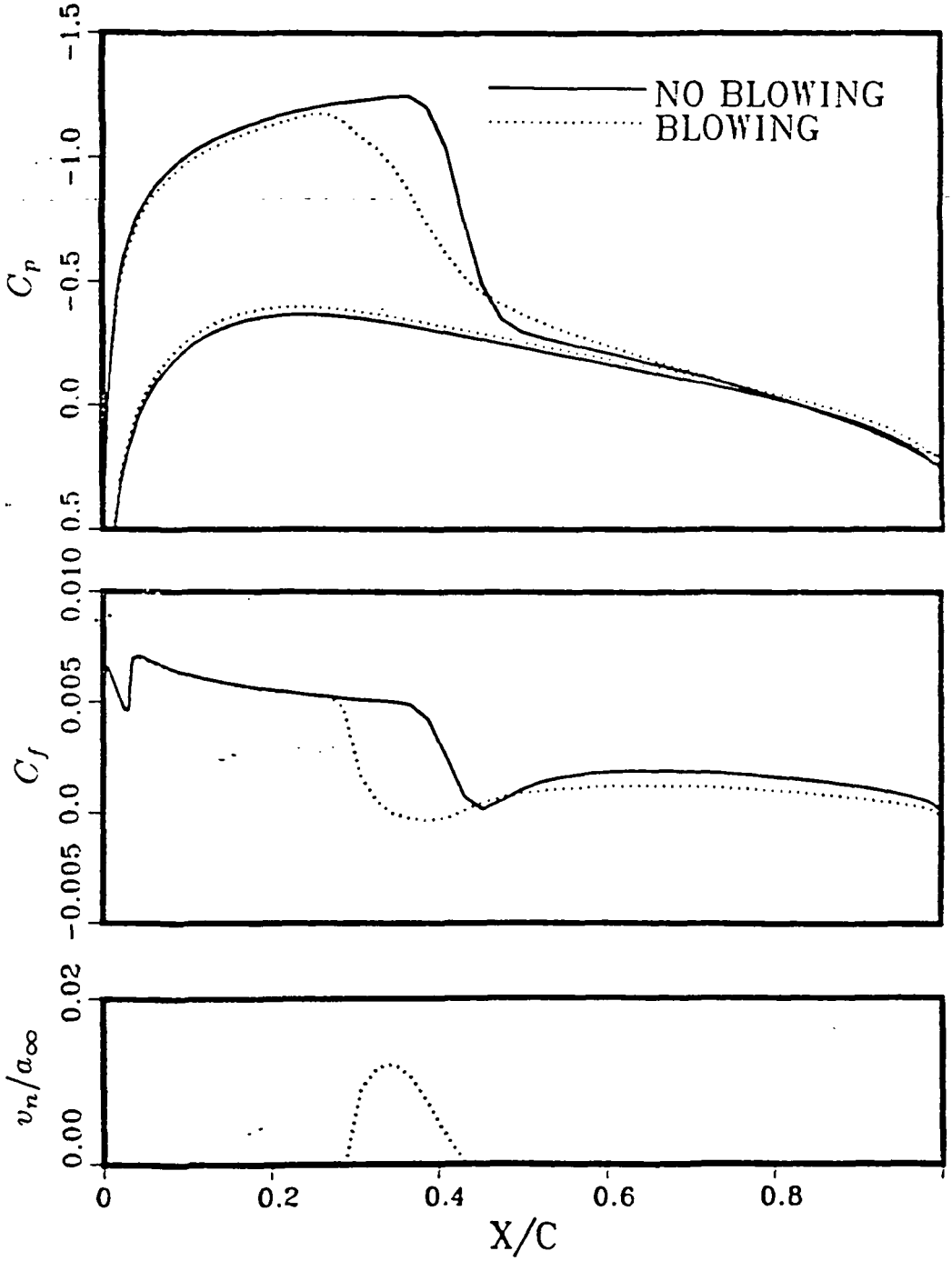

Fig. 6.13 An example of blowing ahead of the shock.

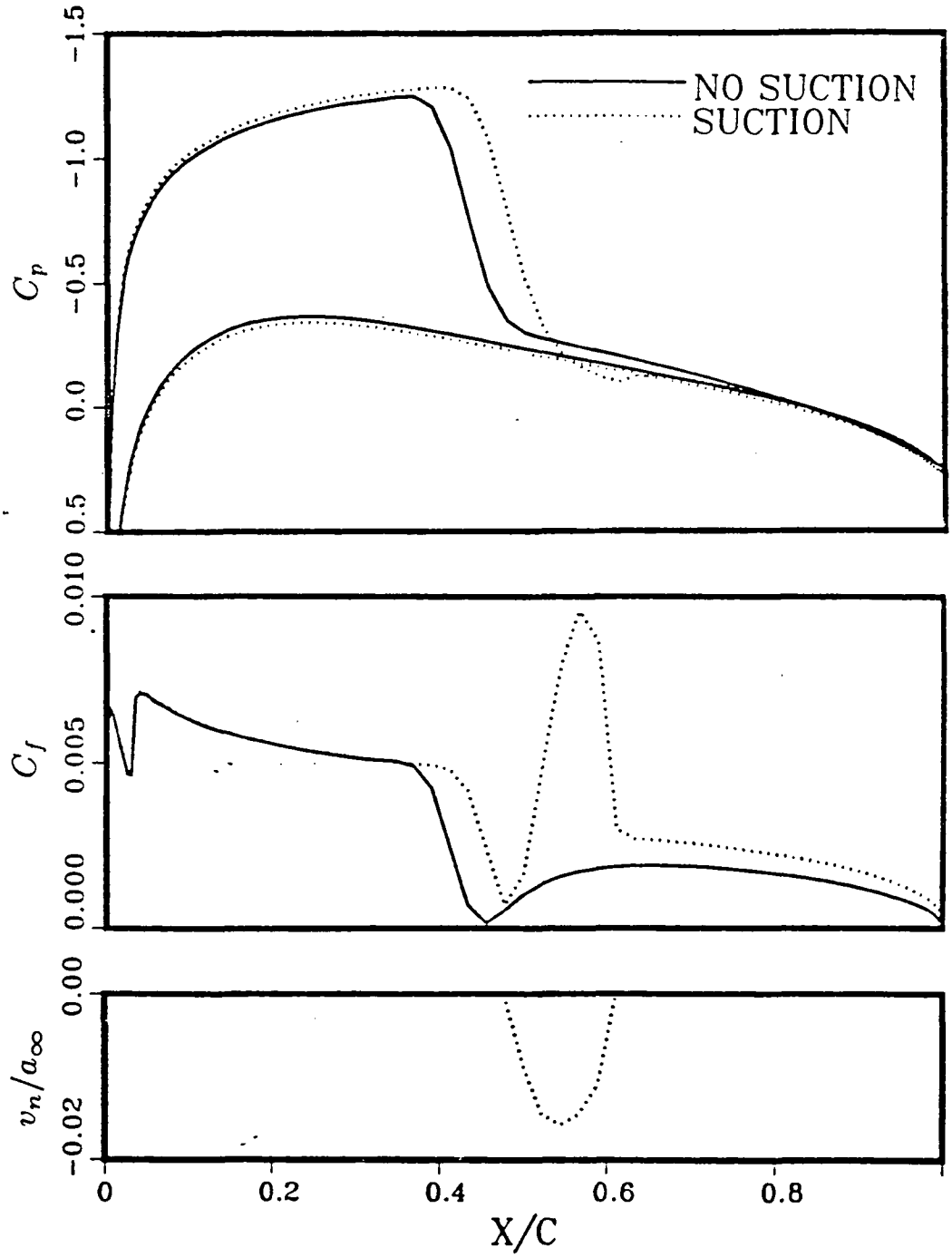

Fig. 6.14 An example of suction behind the shock.

Porous Airfoils

It has been demonstrated in Refs. [22-23] that except for slight differences near the shock and trailing edge, good agreement can be obtained between results from the IBL and TLNS procedures in mildly separated transonic solid-airfoil computations. Similarly, for a NACA 0012 airfoil at $M_\infty = 0.8$, $\alpha = 0.0°$ and $Re = 4.09 \times 10^6$, comparable C_D values of 0.0125 and 0.0123 are obtained respectively via TLNS and IBL procedures (the measured drag coefficient of the solid airfoil is 0.0106[47]). Computed pressure distributions are plotted in Fig. 6.15(a) in comparison with measurements. The same airfoil is then made porous with a Type 2 porosity distribution $\bar{\sigma}_{max} = 0.1$ (the first model) between $x_1 = 0.3$ and $x_2 = 0.5$ (on both upper and lower surfaces). Again comparable drag coefficients of 0.0127 (TLNS) and 0.0125 (IBL) are obtained numerically. Although Fig. 6.15(b) shows that the pressure jump is smeared by the porous surface, the pressure jump on the airfoil surface still has a tendency to move downstream. Since the airfoil surface over this region is backward facing, the lower pressure moving downstream would increase the pressure drag. The reduction in shock strength is not large enough to compensate the increased viscous pressure drag, so that the total drag of the porous airfoil becomes slightly higher than that of the solid airfoil. Such an effect has also been observed in the laboratory[5-7] at the lower M_∞ range, but it has not been predicted by any inviscid-flow approach which can only evaluate wave drag. The velocity profiles in the boundary layer over the porous surface (from the IBL procedure) are shown in Fig. 6.16. The distance normal to the airfoil has been magnified ten times for clarity. It can be observed that the velocity profiles in the blowing region have a tendency to separate. For this case, the blowing (or suction) velocity at the porous surface is less than 1.0%

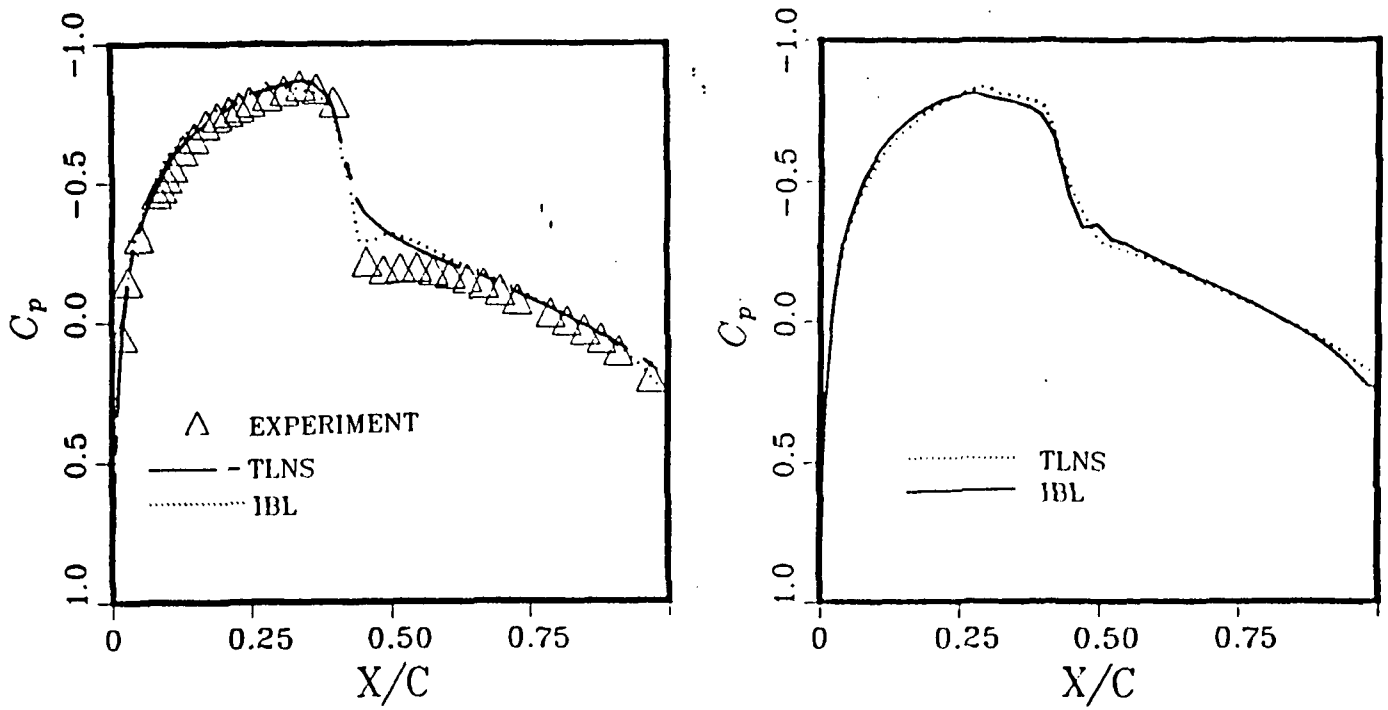

(a) Computed and experimental results for a solid airfoil.

(b) Computed results for a porous airfoil.

Fig. 6.15 Comparison of pressure distributions for a NACA airfoil $M_\infty = 0.8, \alpha = 0°, Re = 4.09 \times 10^6, x_1 = 0.3, x_2 = 0.5$.

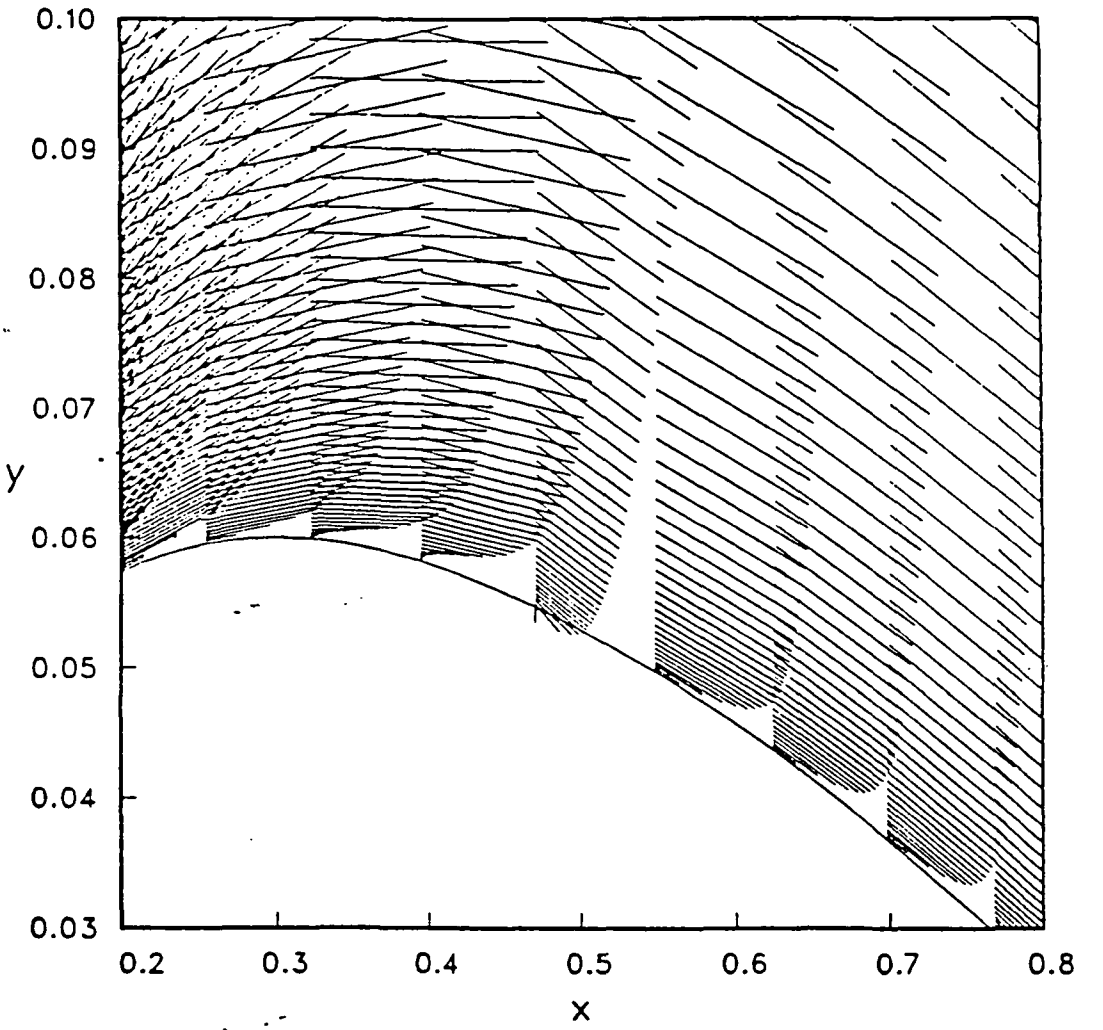

Fig. 6.16 Velocity profiles near the porous airfoil described in Fig. 6.15.

of freestream velocity.

For a lifting case, a calculation (based on the TLNS procedure) was made with a NACA 0012 airfoil at $M_\infty = 0.77$, with $\alpha = 1.0°$, $Re = 4.09 \times 10^6$, the transition fixed at 0.01, and a Type 3 porosity distribution $\bar{\sigma}_{max} = 0.07$ (the first model) from 0.378 to 1.000 which occupies a large portion on the upper surface of the airfoil. It can be seen in Fig. 6.17 that the pressure jump across the shock is weakened, C_L is increased from 0.169 to 0.183, but again C_D is increased from 0.0125 to 0.0137 while the skin-friction drag is little changed. By comparison with the result for the solid airfoil, the skin friction is reduced in the blowing region and is increased in the suction region due to the porosity.

The results in Figs. 6.18(a)-6.19(m) (obtained from the TLNS procedure) are for a symmetrical airfoil which is generated by reflecting the upper surface of an RAE2822 airfoil to the lower surface. The porous surfaces are from 0.615 to 0.805 (the second model on both upper and lower surfaces) with a Type 1 porosity $\bar{\sigma} = 0.4$. The bottom of the cavity is at $y/c = 0.0$. The flow and airfoil parameters are $Re = 6.5 \times 10^6$, $\alpha = 0.0°$ and the transition is fixed at 0.03. For the first case with $M_\infty = 0.82$, C_D is increased from 0.0258 to 0.0273 in the presence of the porous surface. The effects of the porosity are described as follows:

1. The comparison of C_p plots(Fig. 6.18(a)) for the solid and porous airfoils shows that, relative to the solid airfoil, the shock is weakened near the airfoil surface and the pressure on the porous airfoil is lower at the trailing edge. The C_p plots also indicate that the original one strong pressure jump becomes two consecutive weaker jumps, which represent the leading and rear legs of a lambda shock. In this case, the rear leg is slightly behind the

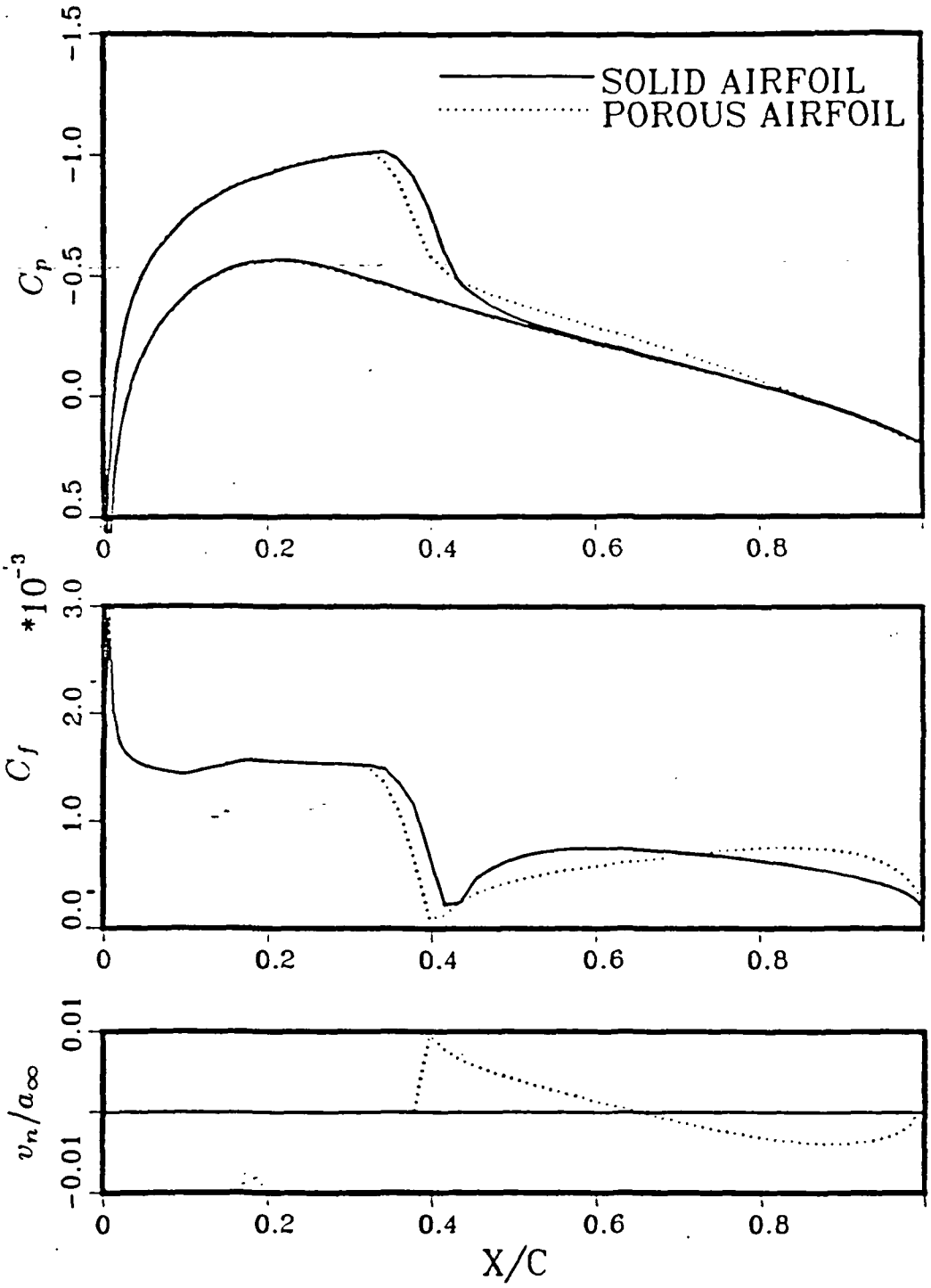

Fig. 6.17 Pressure, skin friction and normal velocity distribution on a lifting NACA 0012 airfoil.

original shock position on the solid airfoil. The lowered pressure at the trailing edge has also been observed experimentally by Raghunathan and Mabey who recently investigated the flow about a 6% thick circular arc model mounted on the upper wall of a wind-tunnel[11]. (See Fig. 6.18(b).)

2. The comparison of the Mach-contour plots (Figs. 6.18(c),(d)) indicates that a lambda shock structure does occur on the porous airfoil. The leading leg of the lambda shock slants at the beginning of the porous surface. This shock structure has been illustrated by the present inviscid-flow approach and also observed experimentally by Nagamatsu et al.(Fig. 6.18(e))

3. A comparison of streamline patterns near the porous region is shown in Figs. 6.18(f),(g). The passive flow through the porous surface generates a bump-like bubble (not a separation bubble) where the lambda shock is situated.

4. Blowing at the leading part of the porous region reduces C_f and suction at the rear part of porous region makes the local C_f larger in the suction region, as shown in Fig. 6.18(h). But downstream of the suction region, the flow has difficulty overcoming the adverse-pressure gradient resulting in values of C_f smaller than for the solid airfoil. Aft of the porous surface, C_f even becomes negative.

5. Pressure contours from the cavity-flow solution are presented in Fig. 6.18(i). The pressure variation is very small within the cavity. Further description of flow in the cavity will be described in the next case.

For the same airfoil just described but at $M_\infty = 0.85$, the computed results indicate about a 10% reduction in drag ($C_D = 0.055$ for the solid airfoil, $C_D = 0.050$ for the porous airfoil). The effects of porosity are described as follows:

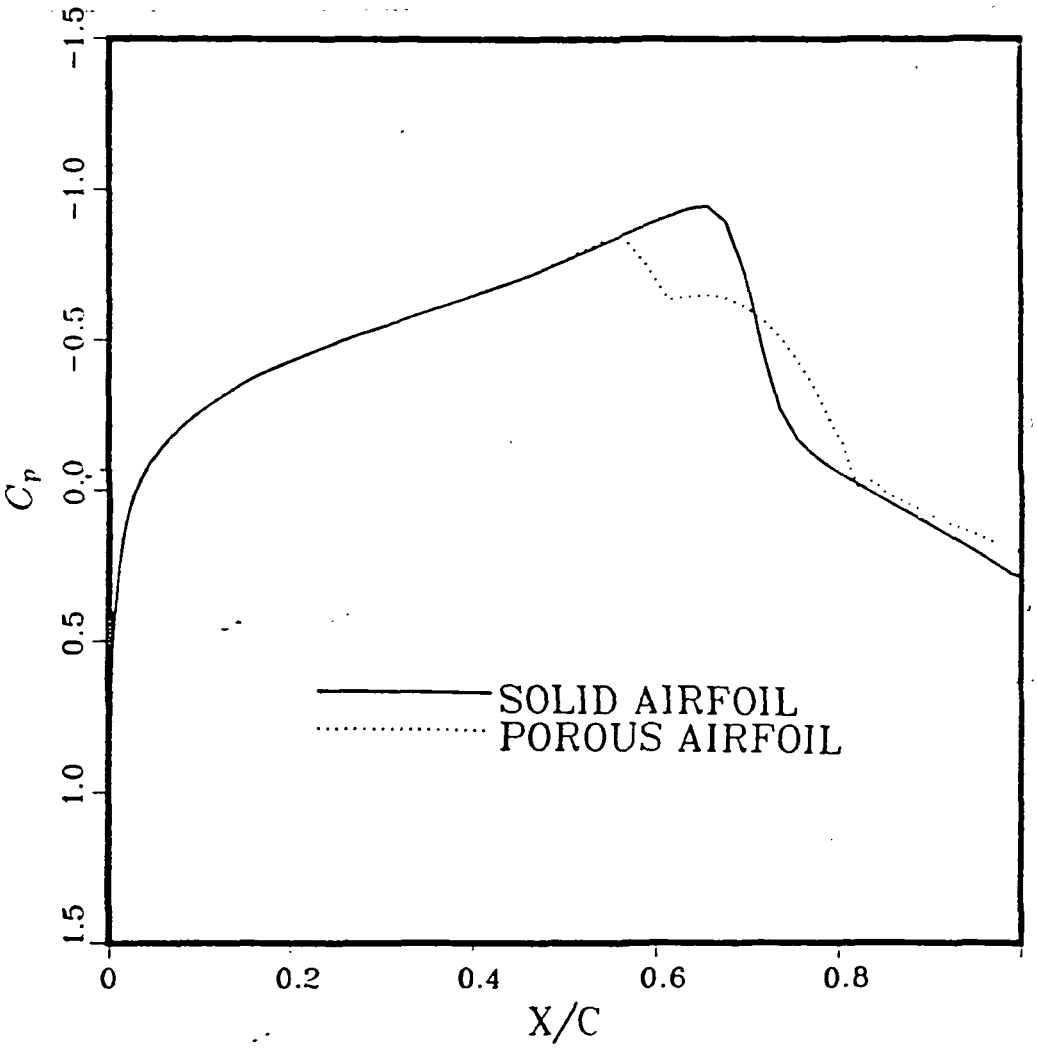

Fig. 6.18 Effects of porosity on a modified RAE 2822 airfoil, $x_1 = 0.615$, $x_2 = 0.805$, Type 1 porosity on both upper and lower surfaces, $\bar{\sigma} = 0.4$, the bottom of cavity is at $y/c = 0.0$, $Re = 6.5 \times 10^6$, $\alpha = 0°$, $M_\infty = 0.82$ and transition is fixed at 0.03.
(a) Comparison of pressure distribution on the airfoil surface.

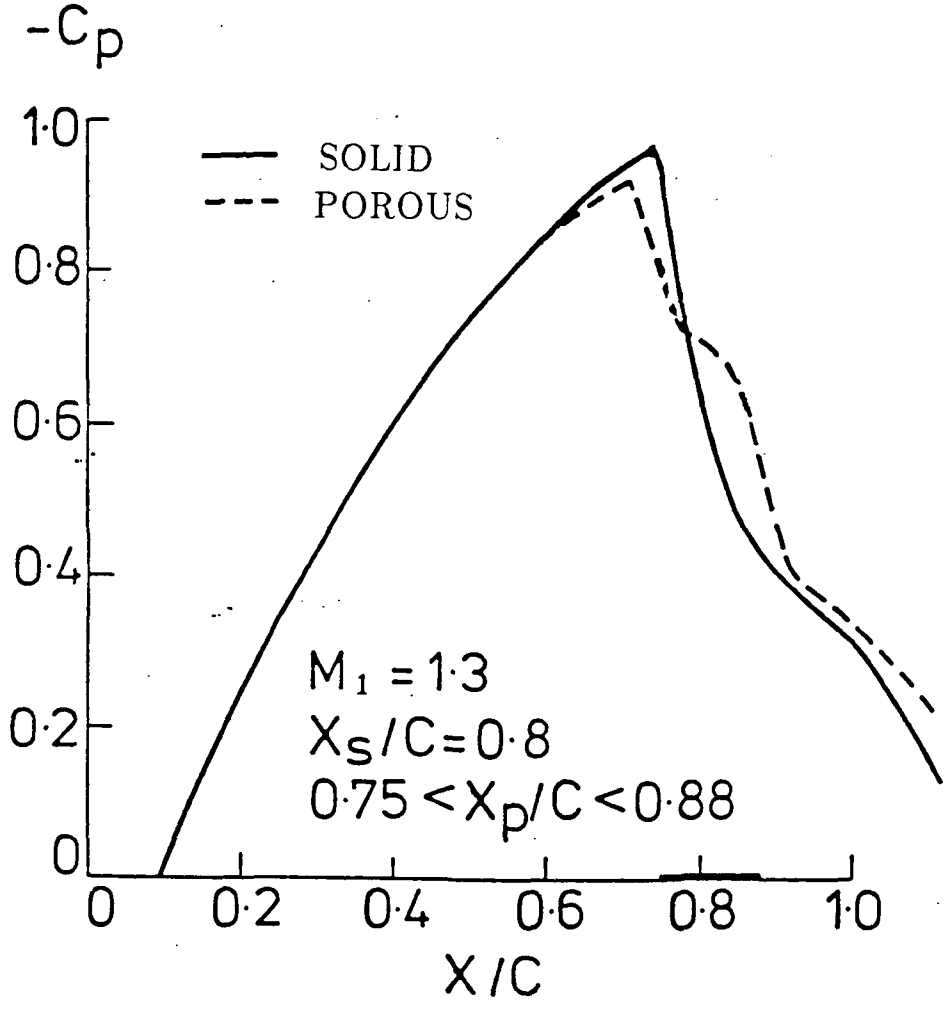

Fig. 6.18(b) Experimental pressure distribution on a 6% thick half circular arc.

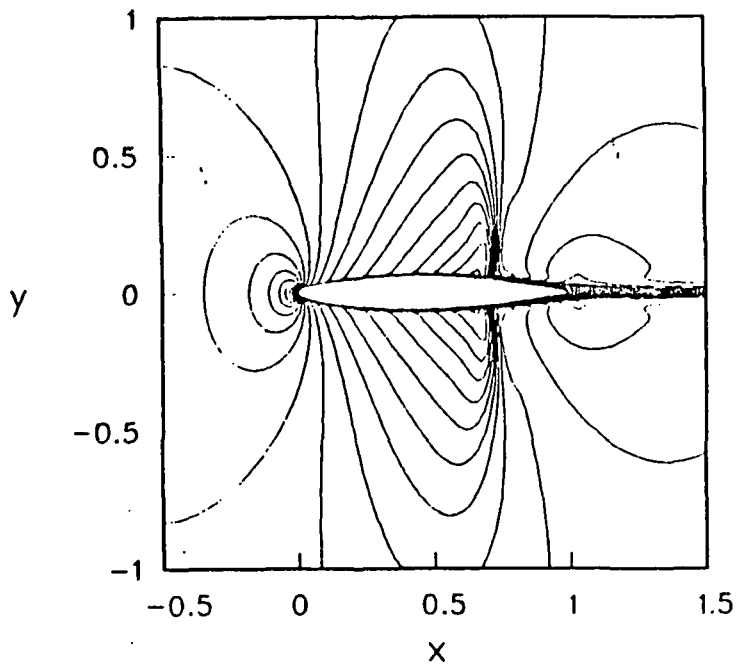

Fig. 6.18(c) Constant Mach number contours around a solid airfoil.

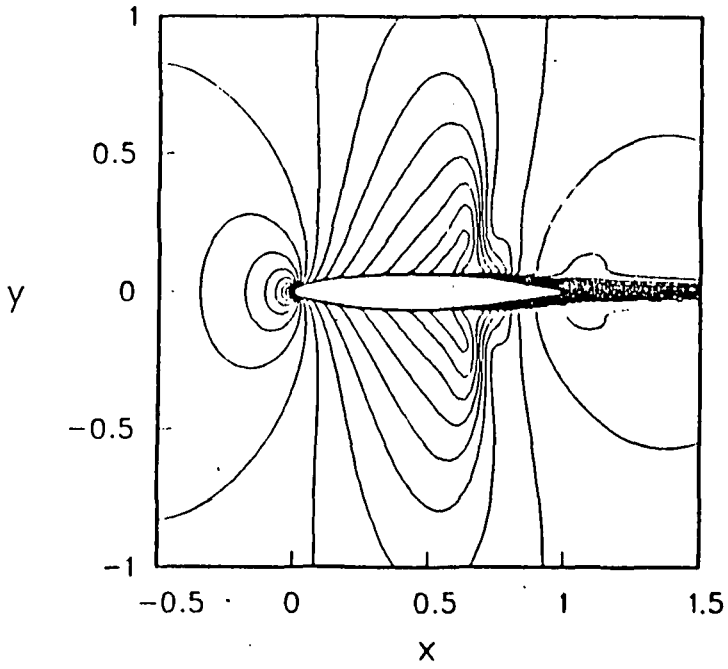

(d) Constant Mach number contours around a porous airfoil.

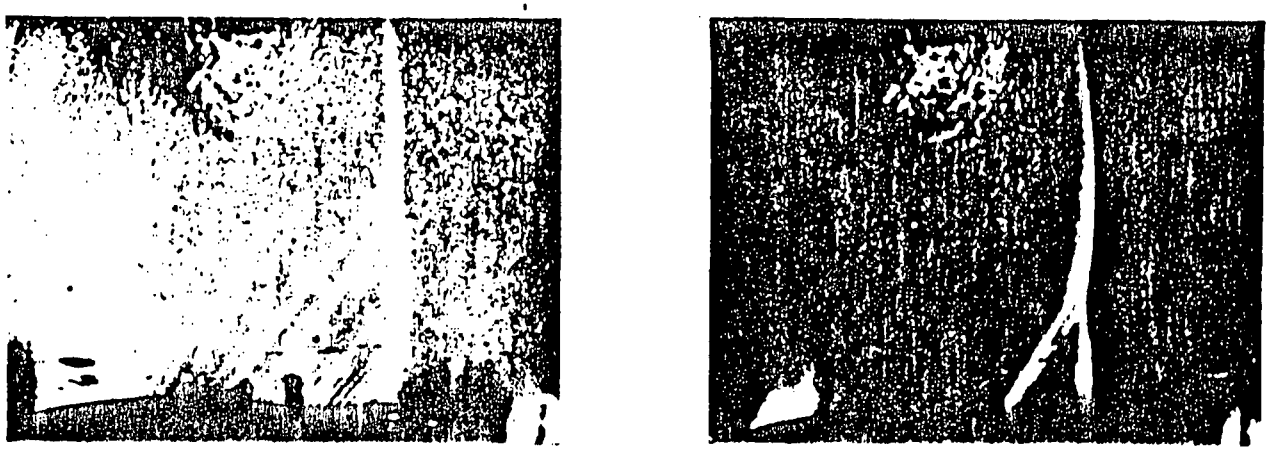

SOLID AIRFOIL

POROUS AIRFOIL

Fig. 6.18(e) Experimental results of a supercritical airfoil obtained by Nagamatsu et al.

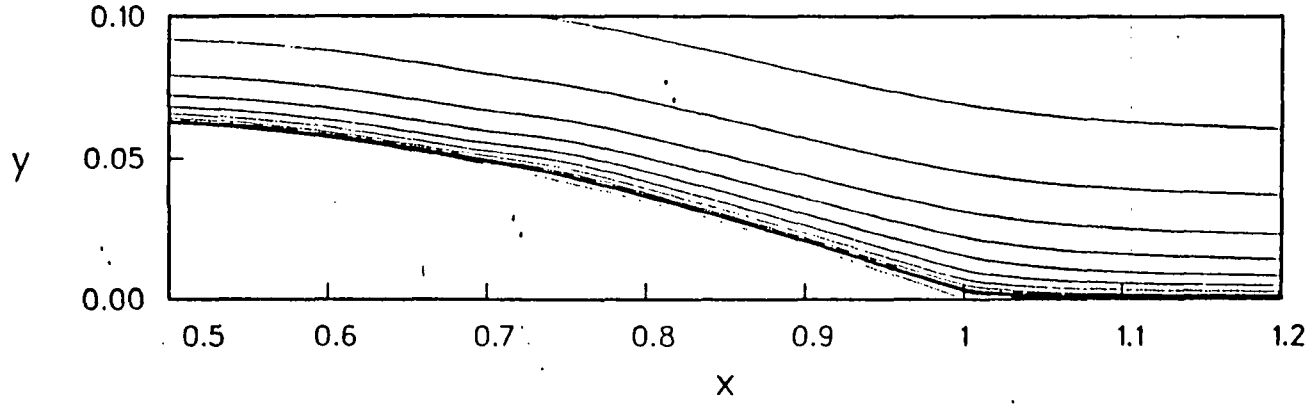

Fig. 6.18(f) Streamline pattern around a solid airfoil.

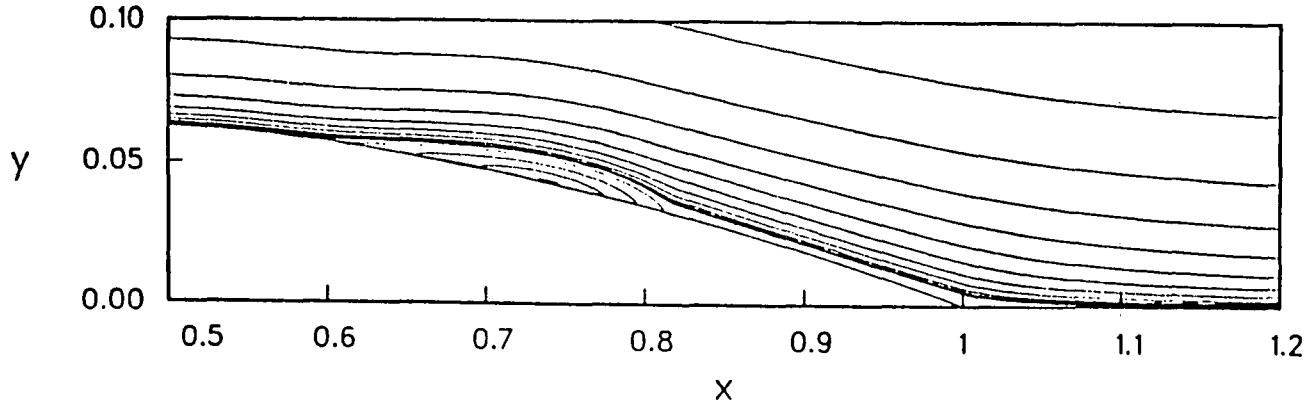

Fig. 6.18(g) Streamline pattern around a porous airfoil.

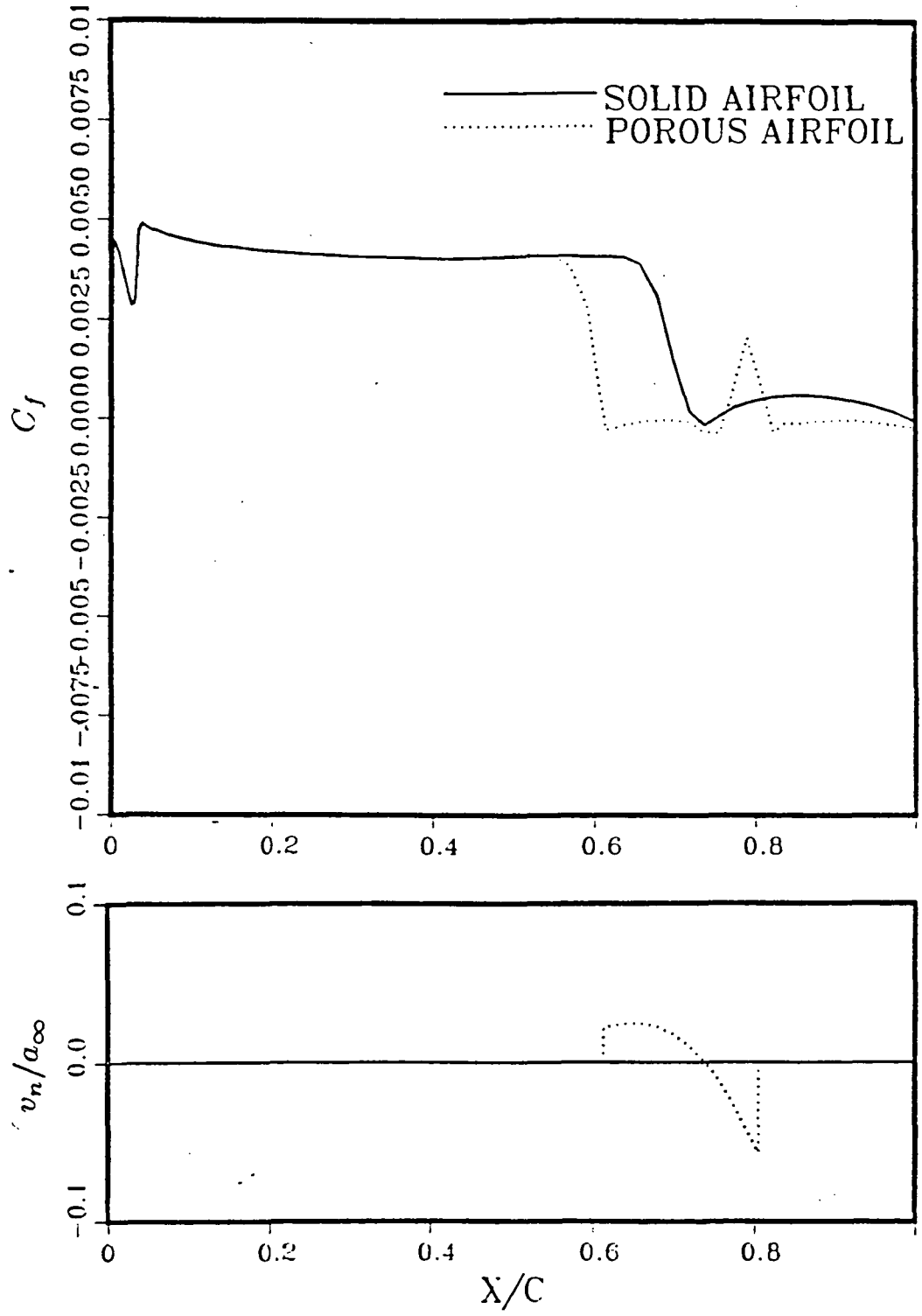

Fig. 6.18(h) Comparison of skin friction.

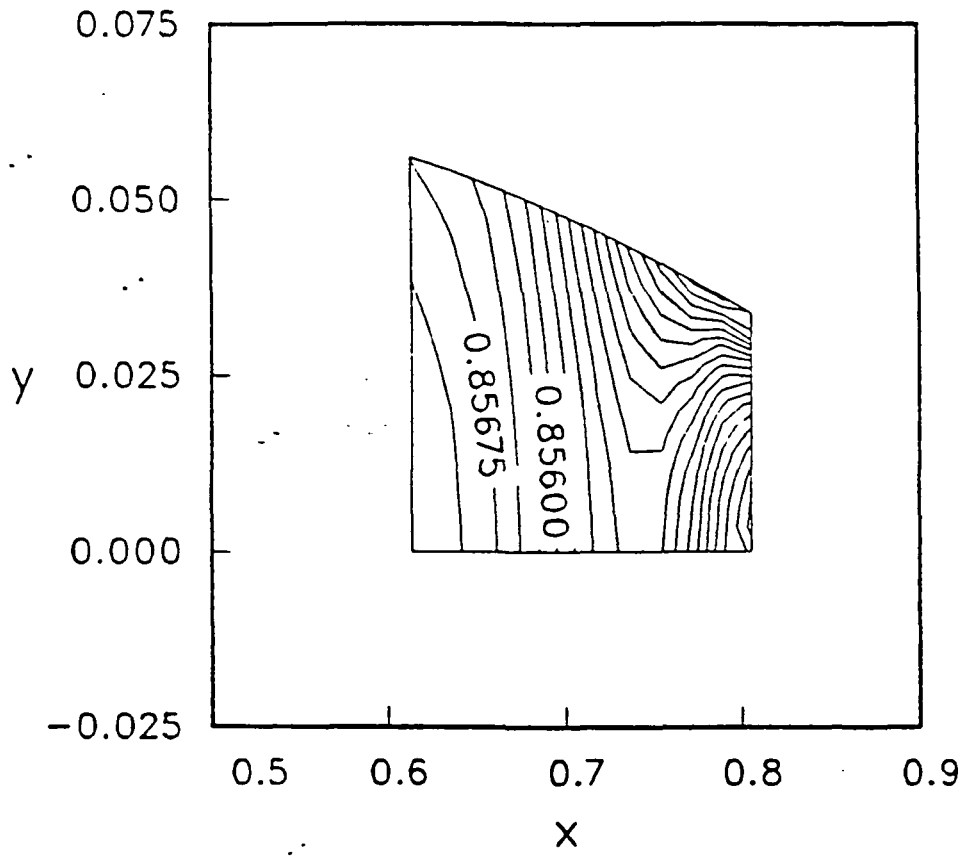

Fig. 6.18(i) Pressure distribution of cavity flow.

1. The comparison of C_p plots (Figs. 6.19(a),(b)) again shows that, relative to the solid airfoil, the shock is weakened near the airfoil surface and the pressure on the porous airfoil is lower at the trailing edge. The C_p plots also indicate that the original one strong pressure jump becomes two weaker jumps. However, the second pressure jump on the airfoil surface is moved upstream slightly, which is opposite to the last case ($M_\infty = 0.82$ and C_D was increased).

The experimental results in Fig. 6.19(b) show the comparison of shock position between the solid and porous airfoils by Nagamatsu et al. The comparison of C_D versus M_∞ corresponding to this figure has been shown in Fig. 6.4. The experimental results may indicate that the drag is reduced when the downstream movement of the rear leg of shock is retarded. From the comparison of last case (rear leg of shock moved downstream and drag was increased) and this case (rear leg of shock moved upstream and drag was reduced), there is a correlation between the experiment and the computation.

2. Once again, the Mach-contour plots (Figs. 6.19(c),(d)) indicate that the Mach contours are less concentrated around the shock on a porous airfoil, indicating a weakened shock. In addition, the results show that the position of the shock is moved upstream slightly.

3. According to the present modeling, the effects of porosity are to increase the viscous losses near the airfoil and decrease the entropy changes away from the airfoil (referring to Figs. 6.19(e),(f)).

4. The separated region is enlarged on the porous airfoil (Figs. 6.19 (g),(h)) and boundary layer becomes thicker. Fig. 6.19(h) indicates that some of the fluid particles that are blown out are immediately sucked back into the cavity. But some of the fluid particles that are blown out at the upstream end of the porous surface enclose a dead air region before going back into the

cavity.

According to the present turbulence and porosity modeling, for the passive shock/ boundary layer interaction at low angles of attack, there are two possible flow patterns above the porous surface as shown in Fig. 6.19(i). There is a stagnation point in the flow field of bottom pattern (pattern 2), which does not occur in the top pattern (pattern 1). The status of the earlier Fig. 6.18(g) is near a transition from pattern 1 to pattern 2, and the status of Fig. 6.19(h) is a typical pattern 2. Generally, when the shock strength is not strong , the top pattern occurs and the drag may not be reduced. When the shock becomes stronger, the bottom pattern may occur and the drag can be reduced. It can be expected that the separation bubble would burst intermittently and vortex shedding would occur when either Mach number or angle of attack is increased further, and oscillations between pattern 1 and pattern 2 would occur. Up to now, the only experimental investigation on the boundary layer near the porous region was by Krogmann, Stanewsky and Thiede (Refs. [9-10]). The experimental results indicate that the boundary layer is thickened by using a perforated surface with a cavity.

5. As shown in Fig. 6.19(j), the suction at the rear part of the porous region makes C_f more negative over the suction region, which is opposite to the effect shown in Fig. 6.18(h). This result should not be a surprise to us, in that the suction is trying to swallow the separation bubble that lies behind the suction region.

6. The cavity-flow solution is presented in Figs. 6.19(k)-(m). The pressure variation is small within the cavity. The pressure under the shock is lower than at the two ends of the cavity. Since the suction area is smaller

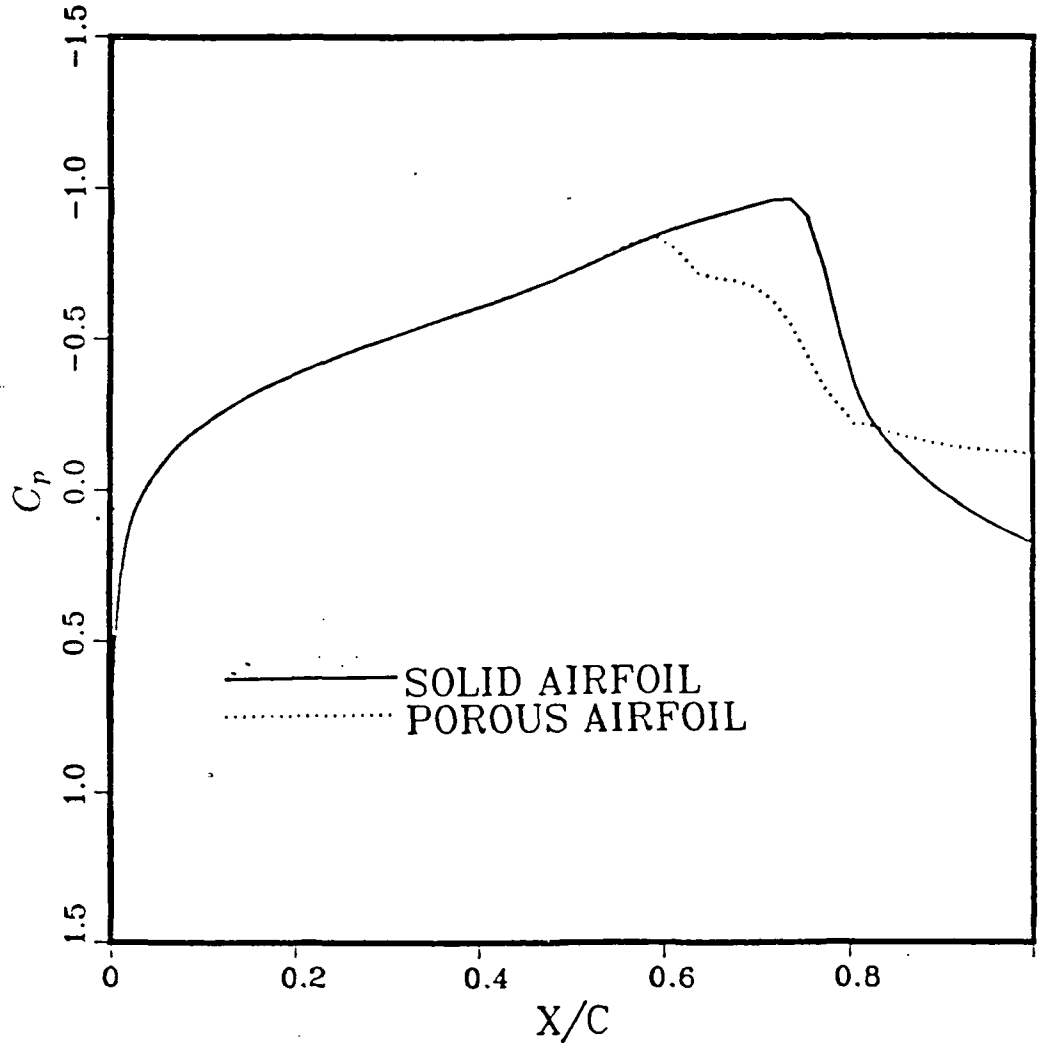

Fig. 6.19 Effects of porosity on a modified RAE 2822 airfoil, $x_1 = 0.615$, $x_2 = 0.805$, Type 1 porosity on both upper and lower surfaces, $\bar{\sigma} = 0.4$, the bottom of cavity is at $y/c = 0.0$, $Re = 6.5 \times 10^6$, $\alpha = 0°$, $M_\infty = 0.85$ and transition is fixed at 0.03.
(a) Comparison of pressure distribution on the airfoil surface.

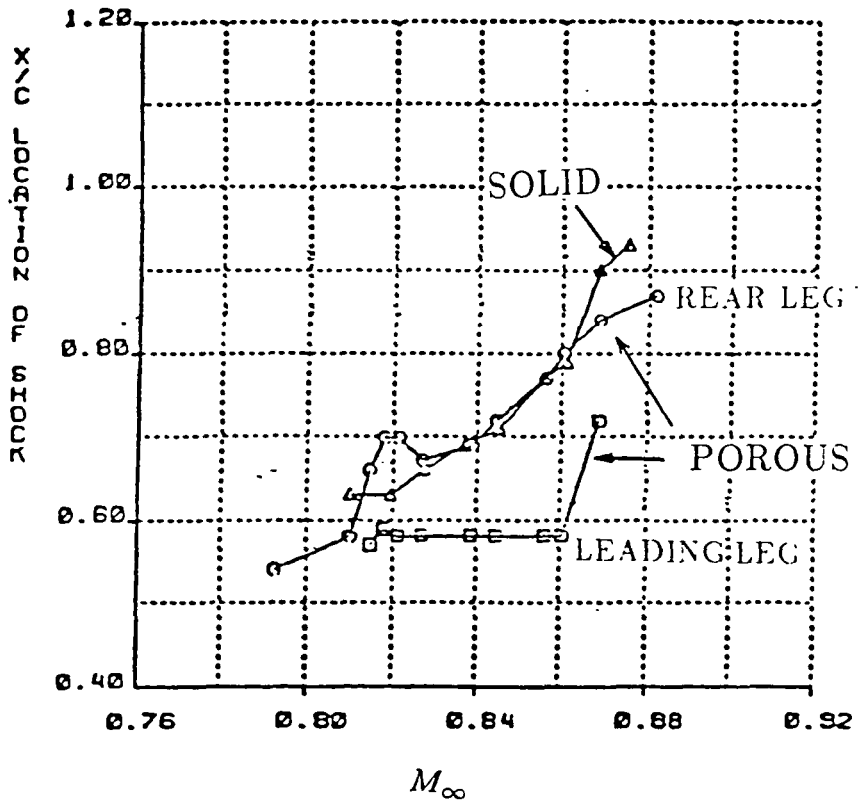

Fig. 6.19(b) Experimental results of shock movement on a supercritical airfoil.

C-2

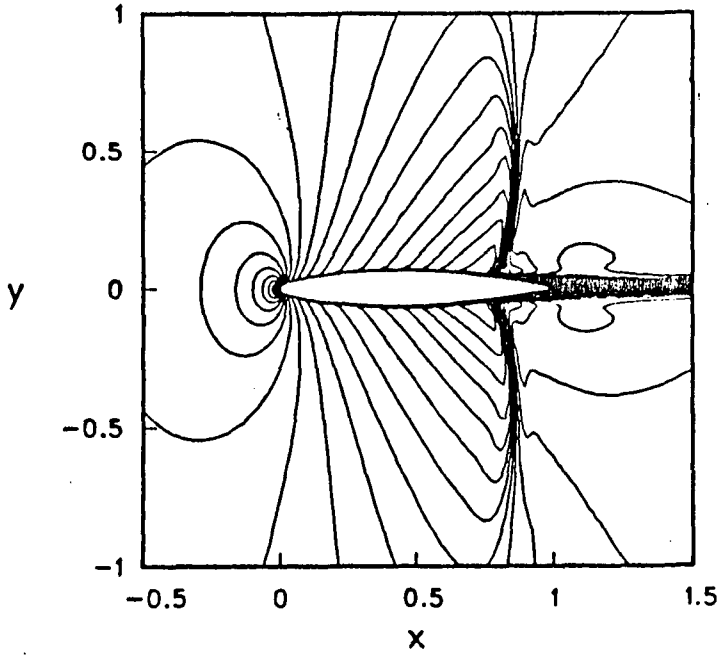

Fig. 6.19(c) Constant Mach number contours around a solid airfoil.

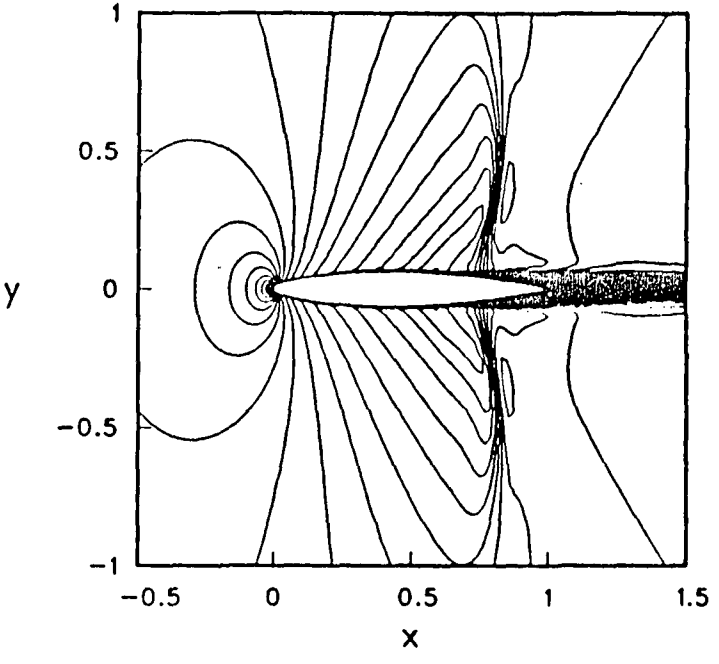

(d) Constant Mach number contours around a porous airfoil.

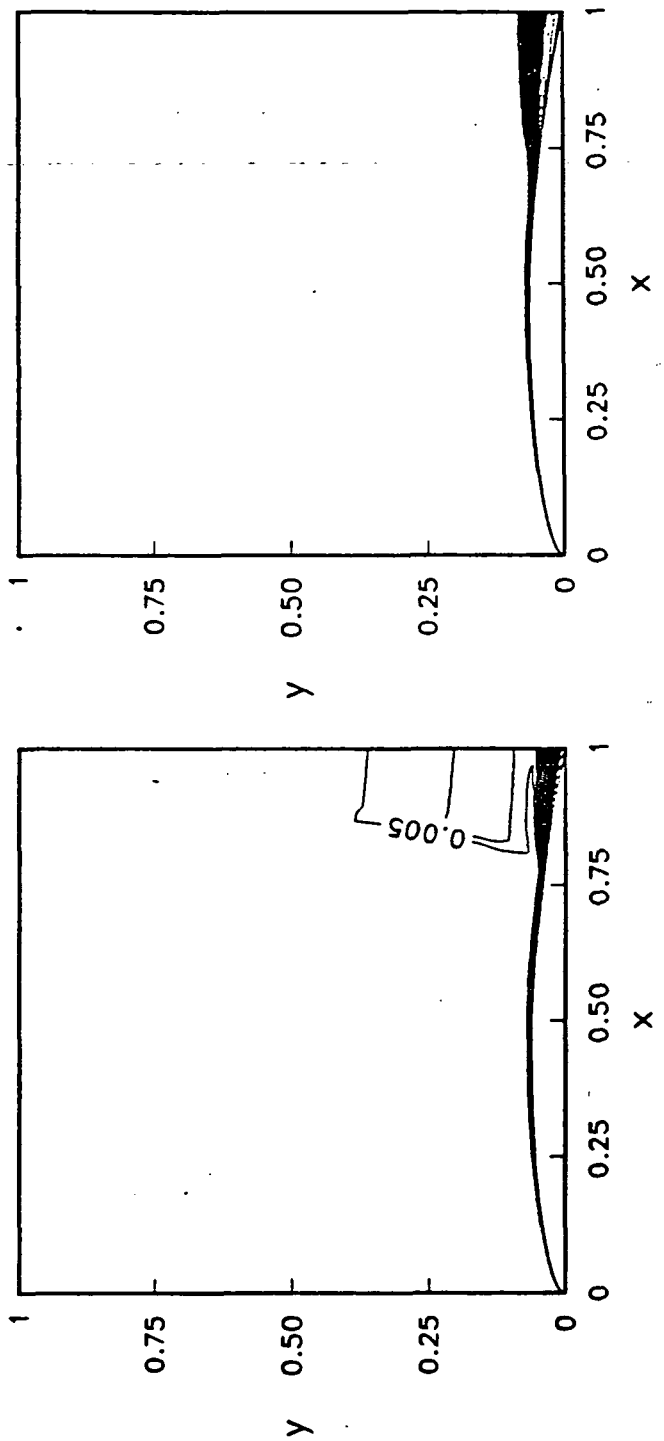

Fig. 6.19(e) Entropy contours around a solid airfoil.

Fig. 6.19(f) Entropy contours around a porous airfoil.

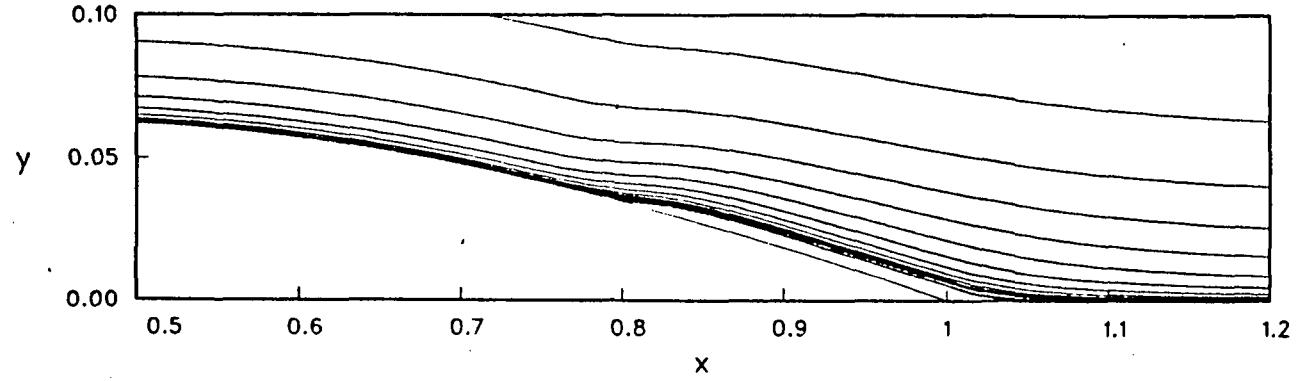

Fig. 6.19(g) Streamline pattern around a solid airfoil.

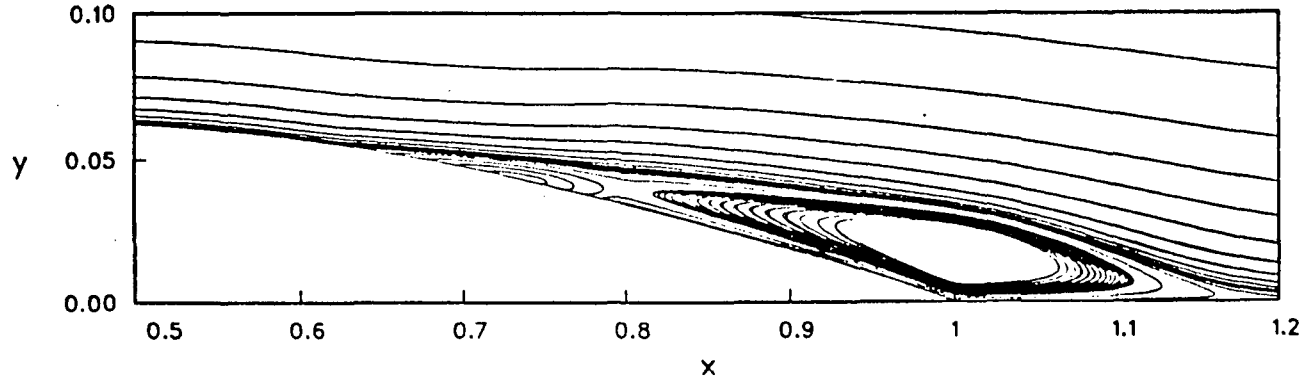

Fig. 6.19(h) Streamline pattern around a porous airfoil.

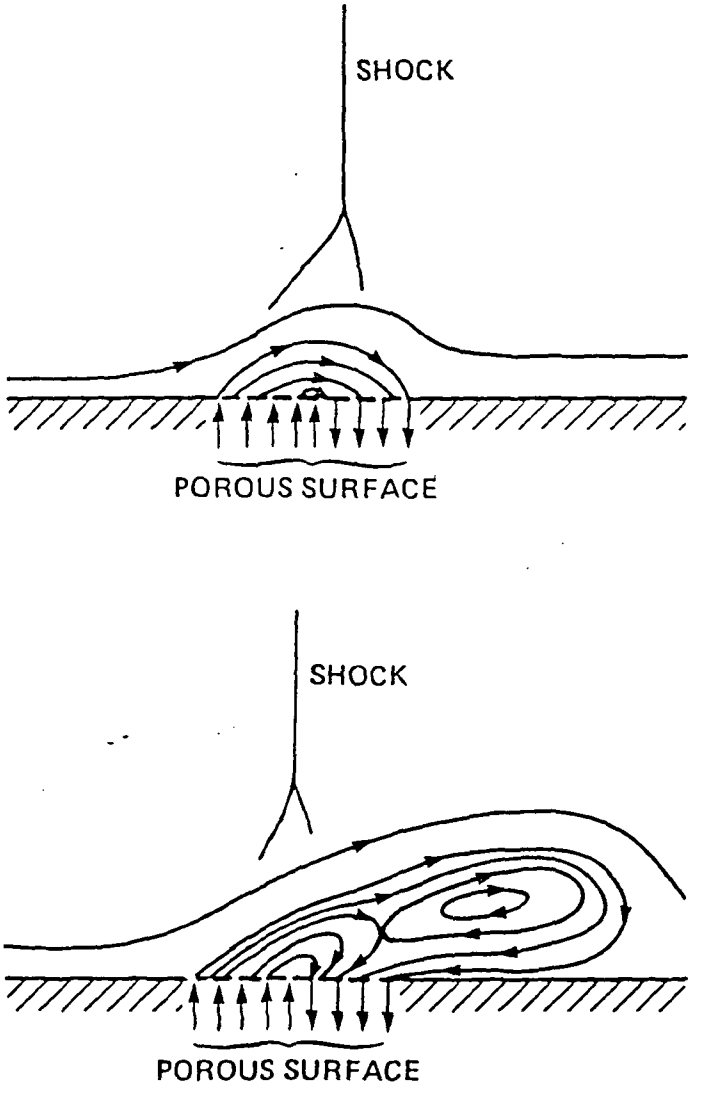

Fig. 6.19(i) Streamline pattern of passive shock/boundary layer interaction.

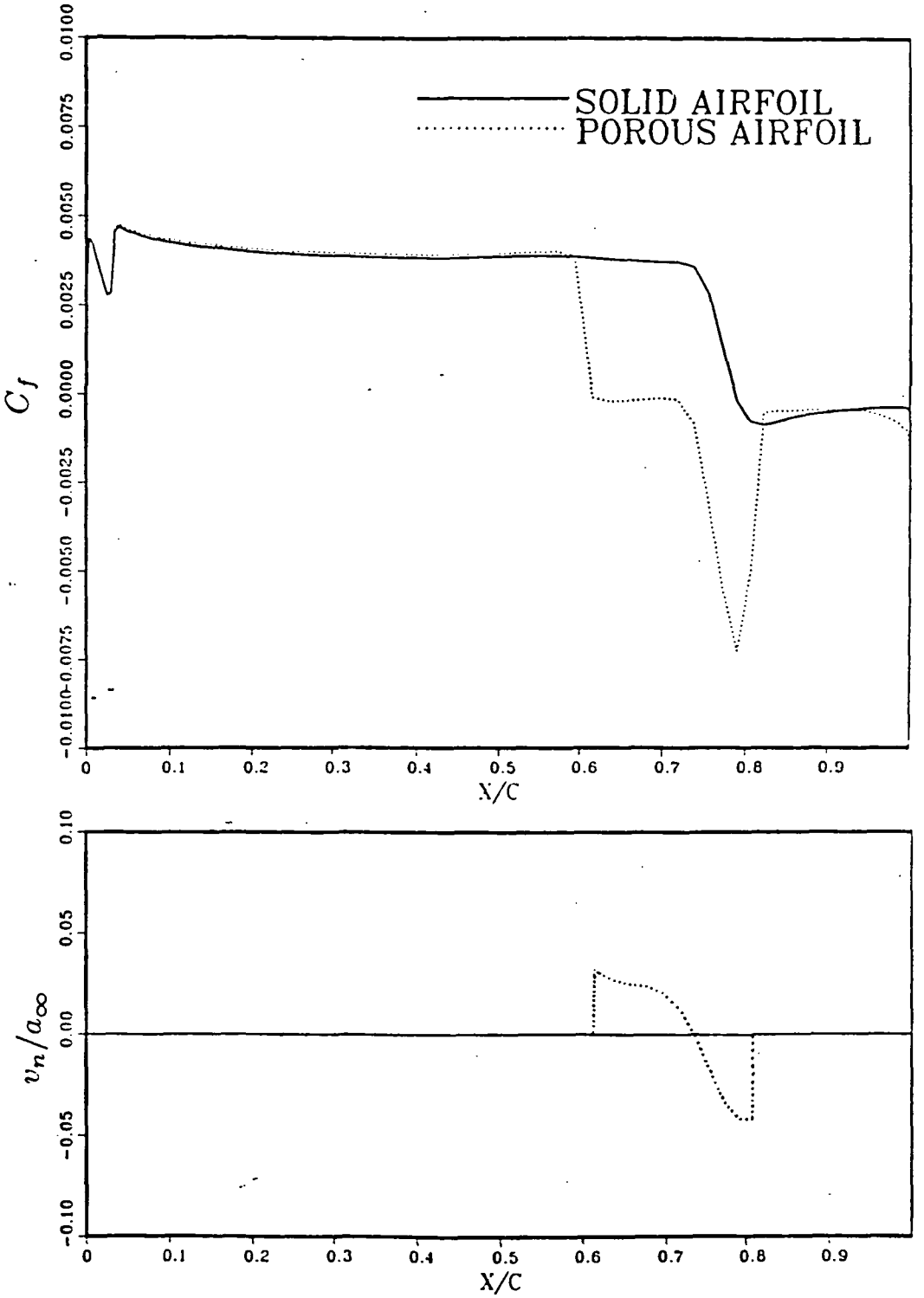

Fig. 6.19(j) Comparison of skin friction.

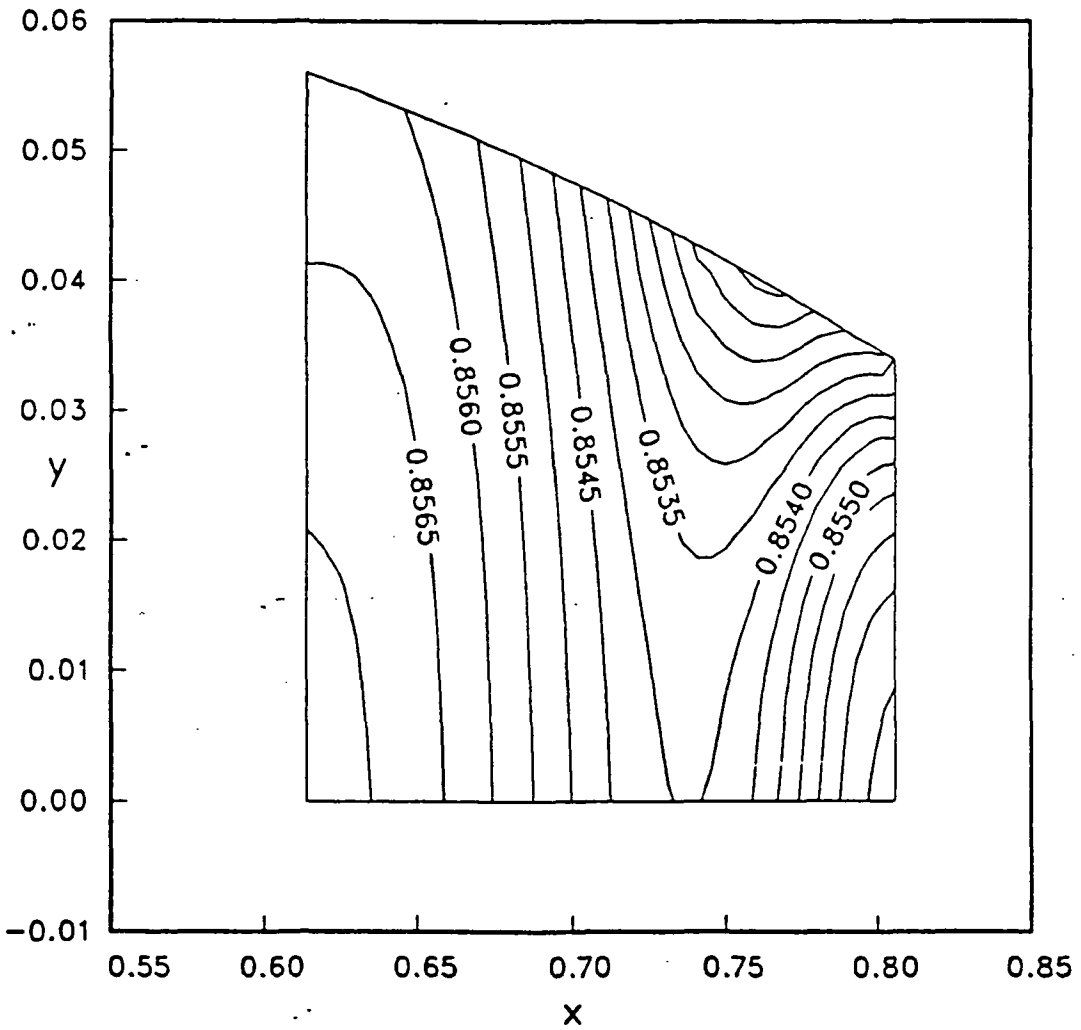

Fig. 6.19(k) Pressure distribution of cavity flow.

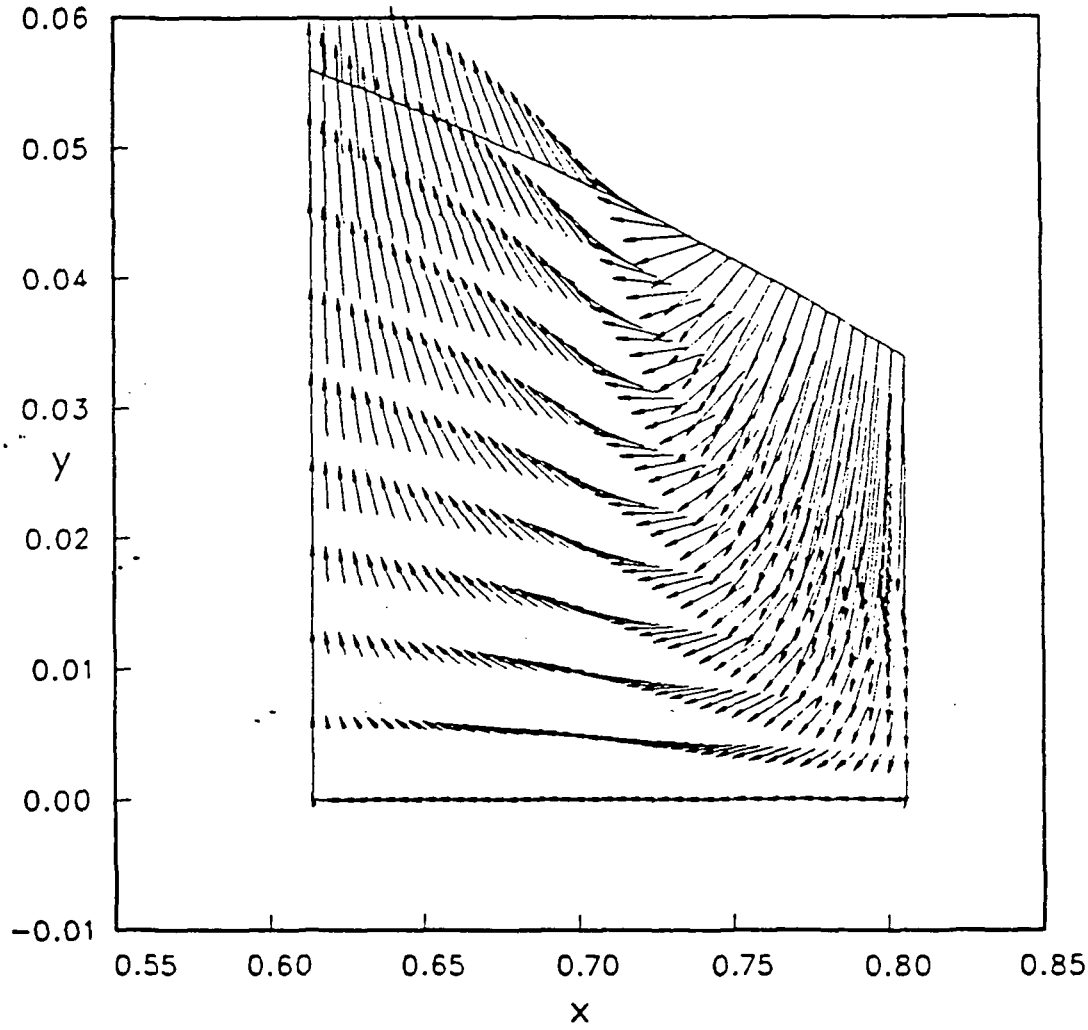

Fig. 6.19(l) Velocity pattern in the cavity.

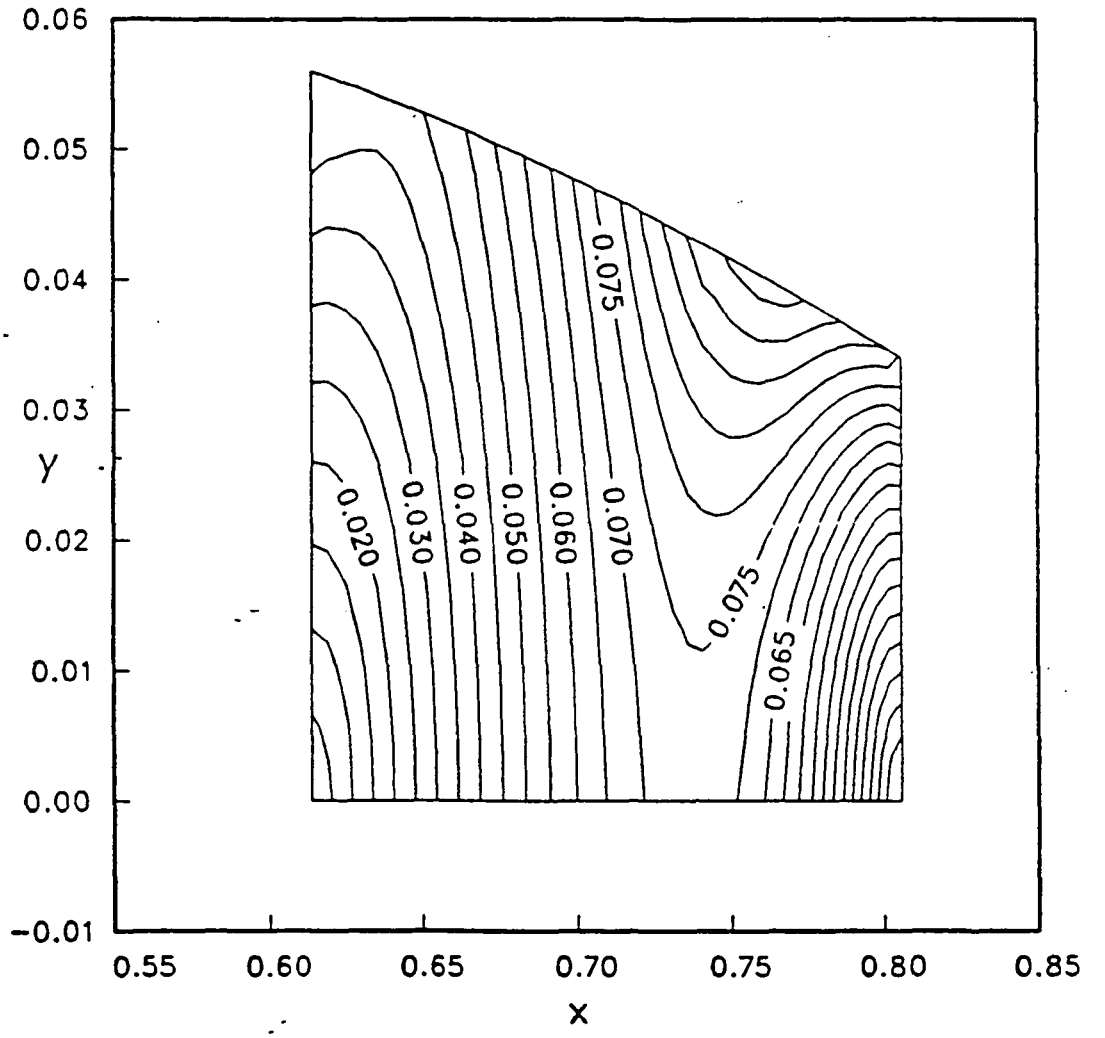

Fig. 6.19(m) Constant Mach number contours in the cavity.

than the blowing area, the average suction velocity is higher than the average blowing velocity. The highest Mach number occurs underneath the shock position.

In summary, the results of the present case reveal some general effects at higher M_∞ and $\alpha \approx 0°$. The shock becomes weaker, shock position is moved slightly upstream, and the viscous loss is increased. These findings are consistent with the results of the last few cases, except here the reduction in shock strength is more than enough to compensate for the increased viscous loss. Also the pattern 2 separated flow becomes mature, and downstream movement of the shock has been prevented. The numerical results strongly suggest that the total drag reduction is mainly due to a weakened shock. Boundary-layer separation occurs due to the blowing at the front part of the porous surface, and the suction at the rear part of the porous surface captures a dead air region. Also the present porosity model including a cavity model shows that the cavity flow is creeping and that pressure variation is very small in the cavity. Therefore whether the first model or the second model is used does not affect the outer flow solution. This might not be so if very small cavities were considered in the interest of conserving space.

The variation of C_D with increasing free-stream Mach number for this airfoil with a slightly longer porous surface from 0.615 to 0.88 is plotted in Fig. 6.20. Drag reduction by the porous surface occurs at Mach numbers higher than 0.84, and it can be as high as 20%. Drag reductions of the same order of magnitude have been found experimentally by Nagamatsu, Ficarra and Dyer[7] in the study of a supercritical airfoil mounted on the bottom wall of a wind tunnel. Finally, the numerical results show that the total drag of the porous airfoil is reduced at higher Mach numbers while increased at lower

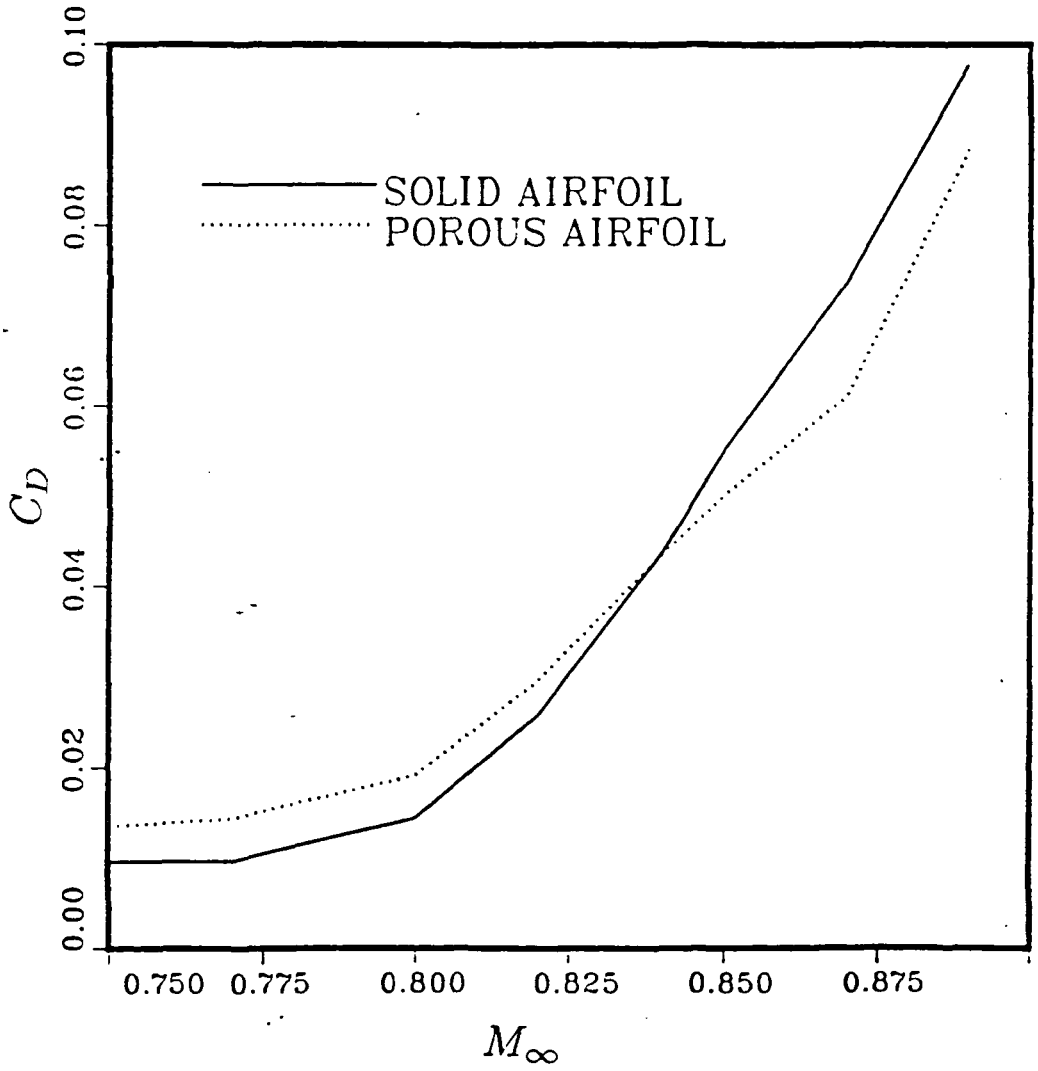

Fig. 6.20 Porosity effects on the drag of a modified RAE 2822 airfoil, $x_1 = 0.615$, $x_2 = 0.88$, Type 1 porosity on both upper and lower surfaces, $\bar{\sigma} = 0.4$, the bottom of cavity at $y/c = 0.0$, $Re = 6.5 \times 10^6$, $\alpha = 0°$ and transition is fixed at 0.03.

Mach numbers, as has been observed experimentally.[5,6,7,11]

CHAPTER VII

CONCLUSION

Summary

A numerical study is made to examine the effects of a porous surface on transonic airfoil performance and to help understand the flow structure of passive shock/boundary layer interactions. The transonic full-potential, IBL and TLNS algorithms modified to handle the transpiration boundary conditions have been used in this study. In many cases, good agreement has been found between experimental results and numerical results.

In the inviscid-flow approach, the results indicate that, by making the airfoil porous near the shock, the shock can be weakened to become a lambda shock so that the wave drag is reduced, and the lift can be increased with an appropriate porosity distribution. However, due partially to the neglect of viscous effects, the C_D versus M_∞ curve, the trailing-edge pressure, and the shock position (without Mach-number correction) do not compare well with the experimental results.

In the viscous-flow approach, computational results qualitatively verify most of the available experimental data and improve the inviscid-flow solutions. For example, the computational results can be used to predict the general trend shown in the C_D versus M_∞ curve, the generally lower trailing-edge pressure on the porous airfoils at higher M_∞ and $\alpha = 0°$, and the thickening of the boundary layer downstream of the porous surface observed in

the laboratory. The results also demonstrate that the porous surface affects not only the shock strength and shock shape but also the position of the shock. Furthermore, the computational results can reveal the structure of passive shock/boundary-layer interactions and the streamline patterns near the porous surface that experiments have had difficulty with.

Most of the work in this investigation has gone into algorithm development (and modification), boundary condition implementation, turbulence modeling, and porosity modeling (including a cavity modeling). Effort was also required to achieve a physical understanding of the flow patterns obtained.

Recommendation

In the last chapter, it has been pointed out that a porous airfoil can improve as well as deteriorate airfoil performance. An adaptive porosity capability would be helpful in the effort to improve airfoil performance under various flight conditions. An optimal porosity distribution might be obtained by using a flow solver program coupled with a numerical optimization algorithm.

Before such expectations can be realized, work needs to be done in turbulence modeling for massively separated flows, studying unsteady flows, refining the porosity model, developing a faster TLNS solver with optimum numerical dissipation terms, or developing a good model for the passive shock wave/boundary-layer interaction via the IBL procedure. Accurate experimental data concerning the boundary layer near the porous region would be very helpful in constructing more realistic porosity-cavity models.

BIBLIOGRAPHY

1. Holst, T. L., Slooff, J. W., Yoshihara, H., and Ballhaus, W. F., Jr. ", Applied Computational Transonic Aerodynamics", AGARDograph No. 266, 1982.

2. Bauer, F., Garabedian F., and Korn, D., "Supercritical Wing Sections, III", Lecture Notes in Economics and Mathematical Systems, No. 150, Springer-Verlag, Berlin, Heidelberg, New York, 1977, pp. 82-83.

3. Chang, P. K., "Control of Flow Separation", McGraw-Hill, New York, 1976.

4. Inger G. R. and Zee S., "Transonic Shock/Turbulent Boundary Layer Interaction with Suction or Blowing", Journal of Aircraft, Vol.15, Nov. 1978, pp 750-754.

5. Bahi, L., Ross, J. M., and Nagamatsu, H. T., "Passive Shock Wave/Boundary Layer Control for Transonic Airfoil Drag Reduction", AIAA Paper 83-0137, Jan. 1983.

6. Nagamatsu, H. T., Orozco, R. D., and Ling, D. C., "Porosity Effect on Supercritical Airfoil Drag Reduction by Shock Wave/Boundary Layer Control", AIAA Paper 84-1682, June 1984.

7. Nagamatsu, H. T., Dyer, R., and Ficarra, R. V., "Supercritical Airfoil Drag Reduction by Passive Shock Wave/Boundary Layer Control in the Mach Number Range .75 to .90", AIAA Paper 85-0207, Jan. 1985.

8. Savu, G., Trifu, O., and Dumitrescu, L. Z., "Suppression of Shocks on Transonic Airfoils", 14th Int'l. Symp. on Shock tubes and Waves, Sydney, Austrlia 1983.

9. Krogmann, P., Stanewsky, E., and Thiede, P., "Effects of Suction on Shock/Boundary-Layer Interaction and Shock-Induced Separation", Journal of Aircraft, Vol. 22, Jan. 1985, pp. 37-42.

10. Thiede, P., Krogmann, P., and Stanewsky, E., "Active and Passive Shock Boundary Layer Interaction Control on Supercritical Airfoils", AGARD CP-365, Improvement of Aerodynamic Performance Through Boundary Layer Control and High Lift Systems, May, 1984, pp. 24-1 to 24-13.

11. Raghunathan, S., and Mabey, D. G., "Passive Shockwave Boundary Layer

Control Experiments on a Circular Arc Model", AIAA Paper 86-0285, Jan. 1986.

12. Prandtl, L., "Über Flüssigkeitsbewegung bei sehr kleiner Reibung", Proc. 3rd Int. Math. Congr., Heidelberg, 1904.

13. Melnik, R. E., "Turbulent Interaction on Airfoils at Transonic Speeds – Recent Devellopments", Proc. AGARD Conf. on Comput. of Viscous-Inviscid Interactions, 1980, AGARD CP291, Paper 10.

14. LeBalleur, J. C., "Computation of Flows Including Strong Viscous Interactions With Coupling Methods", Proc. AGARD Conf. on Comput. of Viscous-Inviscid Interactions, 1980, AGARD CP291, Paper 1.

15. Lock, R. C. and Firmin, M. C. P., "Survey of Techniques for estimating Viscous Effects in External Aerodynamics", Proc. of the IMA Conf. on Numerical Methods in Aero. Fluid Dynamics, Reading, 1980, New York: Academic Press, 1982, pp. 337-430.

16. Visbal M. R. and Shang J. S., "Comparative Study Between Two Navier-Stokes Algorithms for Transonic Airfoils", AIAA Journal, Vol. 24, No. 4, April 1986, pp. 599-606.

17. Savu, G. and Trifu, O., "Porous Airfoils in Transonic Flow", AIAA Journal, Vol. 22, No. 7, July 1984, pp. 989-991.

18. Olling, C. R., "Viscous-Inviscid Interaction in Transonic Separated Flow over Solid and Porous Airfoils and Cascades", Ph.D dissertation, The University of Texas at Austin, December 1985.

19. Ram, R. B., Vemuru, C. S., and Harvey, W. D.,"Hybrid Approach to Steady Transonic Normal Shock-Compressible Laminar Boundary Layer Interactions over Airfoils with Suction", AIAA Paper 85-0522, March 12-14, 1985.

20. Inger G. R. and Nandanan M., "Prediction of Local Suction Effects on Transonic Shock/Turbulent Boundary Layer Interaction and Downstream Flow", AIAA Paper 86-1035, May 12-14, 1986.

21. Holst, T. L., "Implicit Algorithm for the Conservative Transonic Full-Potential Equation Using an Arbitrary Mesh", AIAA Journal, Vol. 17, Oct. 1979, pp. 1038-1045.

22. Van Dalsem, W. R., "Simulation of Separated Transonic Airfoil Flow by Finite-Difference Viscous-Inviscid Interaction", Ph.D dissertation, Stanford University, June 1984.

23. Van Dalsem, W. R. and Steger, J. L., "Finite-Difference Simulation of

Transonic Separated Flow Using a Full-Potential Boundary-Layer Interaction Approach", AIAA Paper 83-1689, Presented at the 16th Fluid & Plasma Dynamics Conference, Danvers, Massachusetts, July 12-14, 1983.

24. Pulliam, T. H., "Euler and Thin Layer Navier-Stokes Codes", Notes for Computational Fluid Dynamics User's Workshop, The University of Tennessee Space Institute Tullahoma, Tennessee, March 12-16, 1984.

25. Liepmann, H. W. and Roshko, A., "Elements of Gasdynamics", 1956.

26. Steger, J. L. and Baldwin, B. S., "Shock Waves and Drag in the Numerical Calculation of Isentropic Transonic Flow", NASA TN D-6997, 1972.

27. Dougherty, F. C., Holst, T. L., Gundy, K. L., and Thomas, S. D., "TAIR - A Transonic Airfoil Analysis Computer Code", NASA TM-81296, May 1981.

28. Flores, J., Holst, T. L., Kwak, D. and Batiste, D.M., "New Consistent Spatial Differencing Scheme for the Transonic Full-Potential Equations", AIAA Paper 83-0373, Presented at the AIAA 21th Aerospace Sciences Meeting, Reno, Nevada, January 10-13, 1983.

29. Sorenson, R. L., "A Computer Program to Generate Two-Dimensional Grids About Airfoils and Other Shapes by the Use of Poisson's Equation", NASA TM-81198, May 1980.

30. Steger, J. L. and Sorenson, R. L., "Automatic Mesh-Point Clustering Near a Boundary in Grid Generation with Elliptic Partial Differential Equations", Journal of Computational Physics, Vol. 33, Dec., pp. 405-410.

31. LeBalleur, J. C., Peyret, R., and Viviand H., "Numerical Studies in High Reynolds Aerodynamics ", Computers and Fluids, Vol.8, 1980.

32. Cebeci, T. and Smith, A. M. O., "Analysis of Turbulent Boundary Layers ", Academic Press, 1974.

33. Pulliam, T. H. and Chaussee, D. S., "A Diagonal Form of an Implicit Approximate-Factorization Algorithm", Journal of Comp. Physics, Vol. 39, No. 2, Feb. 1981, pp. 347-363.

34. Salas, M., Jameson, A., and Melnik, R., "A Comparative Study of the Nonuniqueness Problem of the Potential Equation", AIAA paper 83-1888, Danvers, Mass, July, 1983.

35. Barth, T. J., Pulliam T. H., and Buning P. G., "Navier-Stokes Computations for Exotic Airfoils", AIAA paper 85-0109, Reno, Nev., Jan. 1985.

36. Baldwin, B. S. and Lomax, H.,"Thin Layer Approximation and Algebraic

Model for Separated Turbulent Flows", AIAA Paper 78-257, Jan. 1978.

37. Bushnell, D. M., Cary, A. M. Jr., and Harris J. E., "Calculation Methods for Compressible Turbulent Boundary Layers-1976", NASA SP-422, 1977.

38. Crawford, M. E. and Kays, W. M., "STAN5 - A Program for Numerical Computation of Two-Dimensional Internal and External Boundary Layer Flows", NASA CR-2742, 1976.

39. Kays, W. M. and Moffat R. J., "The Behavior of Transpired Turbulent Boundary Layers", NASA CR-119147, 1975.

40. Patankar, S. V. and Spalding, D. B. "Heat and Mass Transfer in Boundary Layers", 2nd Ed. International Textbook Co., London, 1970.

41. Baker, R. J., Jonsson, V. K., and B. E. Launder, "The Turbulent Boundary Layer with Streamwise Pressure Gradient and Foreign-Gas Injection", Imperial College Rept. ET/TN/G/31.

42. Mehta, U., "Reynolds Averaged Navier-Stokes Computations of Transonic Flows Around Airfoils", Presented at the Second Symposium on Aerodynamic Flow, Long Beach, California, January 17-20, 1983.

43. Cook, P. H., McDonald, M. A., and Firmin, M. C. P., "Aerofoil RAE 2822-Pressure Distributions and Boundary Layer and Wake Measurements", AGARD AR 138, Paper A6, 1979.

44. Baldwin, B. S. and Turner, J. B., "Wall Interference in Wind Tunnels With Slotted and Porous Boundaries at Subsonic Speeds", NACA TN 3176, 1953.

45. Ballhaus, W. F, and Jameson, A., and Albert J., "Implicit Approximate-Factorization Schemes for Steady Transonic Flow Problems", AIAA Journal, Vol. 16, No. 6, June 1978, pp. 573-579.

46. Delery, J and Marvin J. G., "Shock-Wave Boundary Layer Interactions", AGARD AG-280 pp. 8-9, 1986.

47. Thibert, J. J. and Grandjacques, M., and Ohman L. H., "NACA 0012 Airfoil", AGARD AR 138, Paper A1, 1979.